SENSORS FOR MOBILE ROBOTS

THEORY AND APPLICATION

H.R. EVERETT

This is an unprecedented reference work that compiles into one convenient source everything the student or experienced developmental engineer needs to know about the many supporting technologies associated with the rapidly evolving field of robotics. Presenting the material in a manner which often parallels strategies of robotic development, Everett provides a comprehensive yet easy-to-understand explanation of the theory of sensor operation. An objective review of both prototype and commercially available candidate systems is presented throughout, followed up with practical lessons learned from actual use on various robotic vehicles. This book is a must-have for everyone in the robotics research and development community, be it in industry, government, or academia.

"A timely contribution to the field of mobile robotics, Everett's book is the most comprehensive survey appearing to date on sensor technology for this domain. His text serves both as a valuable reference for the experienced roboticist while also providing a thorough tutorial on the issues and technologies of mobile sensing for the novitiate."
—Professor Ron Arkin
Director, Mobile Robot Laboratory
Georgia Institute of Technology, Atlanta, GA

"*Sensors for Mobile Robots* is the most comprehensive, most meticulously researched, and most authoritative book in the emerging field of mobile robotics, equally valuable for experimentalists and theoreticians alike."
—Professor Johann Borenstein
Head, MEAM Mobile Robotics Laboratory
University of Michigan, Ann Arbor, MI

"In my opinion this book is the definitive work on the subject and is destined to *become a classic.*"
—Professor H.R. Luxenberg
Professor Emeritus, Computer Science Department
California State University, Chico, CA

"This is, simply, an astounding work, in both the range and depth of its coverage."
—*Nuts & Volts Magazine,* May 1995

"*Sensors for Mobile Robots* is the right book at the right time for anyone involved or interested in the rapidly expanding field of mobile robotics or industrial automation. Everett has provided both the breadth and the depth to enlighten designers with new ideas, as well as point them to commercial sources of potential solutions for the plethora of perception problems facing autonomous machines."
—*SENSORS Magazine,* June 1995
Book Review by Anita Flynn
MIT Artificial Intelligence Laboratory
Massachusetts Institute of Technology
Cambridge, MA

Cover photograph:
ROBART II. A second generation security robot employing 132 external sensors

A K Peters, Ltd.

ISBN 1-56881-048-2

Sensors *for* Mobile Robots

Theory and Application

H.R. Everett
Naval Command, Control and Ocean Surveillance Center
San Diego, California

A K Peters, Ltd.
Wellesley, Massachusetts

Editorial, Sales, and Customer Service Office

A K Peters, Ltd.
289 Linden Street
Wellesley, MA 02181

Library of Congress Cataloging-in-Publication Data

Everett, H. R., 1949-
Sensors for mobile robots : theory and application / H.R. Everett.
p. cm.
Includes bibliographical references and index.
ISBN 1-56881-048-2
1. Mobile robots. 2. Robots—Control systems. I. Title.
TJ211.415.E83 1995
629.8 ' 92—dc20 95-17178
CIP

Principle illustrator: Todd Ashley Everett

Printed in the United States of America
99 98 97 96 95 10 9 8 7 6 5 4 3 2 1

Table of Contents

Foreword

A robot's ability to sense its world and change its behavior on that basis is what makes a robot an interesting thing to build and a useful artifact when completed. Without sensors, robots would be nothing more than fixed automation, going through the same repetitive task again and again in a carefully controlled environment. Such devices certainly have their place and are often the right economic solution. But with good sensors, robots have the potential to do so much more. They can operate in unstructured environments and adapt as the environment changes around them. They can work in dirty dangerous places where there are no humans to keep the world safe for them. They can interact with us and with each other to work as parts of teams. They can inspire our imaginations and lead us to build devices that not so long ago were purely in the realms of fiction.

Sensors are what makes it all possible.

When it comes right down to it there are two sorts of sensors. There are visual sensors, or eyes, and there are non-visual sensors. Lots of books have been written about visual sensors and computer vision for robots.

There is exactly one book devoted to non-visual sensors. This one.

We tend to be a little vision-centric in our "view'' (there we go again...) of the world, as for humans vision is the most vivid sensor mechanism. But when we look at other animals, and without the impediment of introspection, another picture (hmmm...) begins to emerge. Insects have two eyes, each with at most perhaps 10,000 sensor elements.

Arachnids have eight eyes, many of them vestigial, some with only a few hundred sensor elements, and at most 10,000 again. But insects have lots and lots and lots of other sensors. Cockroaches, for example, have 30,000 wind-sensitive hairs on their legs, and can sense a change in wind direction and alter the direction in which they are scuttling in only 10 milliseconds. That is why you cannot stomp on one unless you have it cornered, and on top of that get lucky. The cockroach can sense your foot coming and change course much faster than you can change where you are aiming. And those 30,000 sensitive hairs represent just one of a myriad of specialized sensors on a cockroach. Plus each different insect has many varied and often uniquely different sensors. Evolution has become a master at producing non-visual sensors.

As robotics engineers we find it hard to create new sensors, but are all aware that in general our robots have a rather impoverished connection to the world. More sensors would let us program our robots in ways that handled more situations, and do better in those situations than they would with fewer sensors. Since we cannot easily create new sensors, the next best thing would be to know what sensors were already available. Up until this point we have all maintained

our own little libraries of sensors in our heads. Now Bart Everett has written down all he had in his own private library and more. Bart's robots have always stood out as those with the most sensors, because interactive sensing has always been a priority for Bart. Now he is sharing his accumulated wisdom with us, and robotdom will be a better place for it. Besides providing us with an expanded library, Bart has also done it in a way that everyone interested in robotics can understand. He takes us through the elementary physics of each sensor with an approach that a computer scientist, an electrical engineer, a mechanical engineer, or an industrial engineer can relate to and appreciate. We gain a solid understanding of just what each sensor is measuring, and what its limitations will be.

So let's go build some new robots!

Rodney A. Brooks
MIT AI Lab
Cambridge, MA

Preface

My underlying goal in the preparation of this manuscript was to present some general background on the sensing needs of a mobile system, followed by sufficient theory of operation and illustrative examples such that the overall result is both informative and of practical use. Perhaps the most challenging problem I faced early on in this endeavor was how to arrange reams of information on all the various sensors into some semblance of logical order. One considered possibility was to categorize by class of robot (i.e., airborne, underwater, indoor, exterior, autonomous, teleoperated). Given the emphasis of the book, however, it seemed more appropriate to break down the discussion by sensor type.

In an attempt to bound the problem, I decided to eliminate any treatment of airborne or underwater scenarios and focus instead on interior and exterior land-based applications. Even so, there was still considerable difficulty associated with organizing the flow. For example, at least seven different methods of non-contact ranging techniques are known to exist; one of these methods alone (triangulation) can be implemented in five different ways. Almost all such ranging systems can operate in the acoustical or electromagnetic regions of the energy spectrum; can be active or passive; and may have markedly different assigned functions in actual deployment.

After much weighing of alternative strategies, I chose to present the material in a manner that to some extent parallels the strategy often employed in robotic development. The initial thrust of most early research efforts in which I participated was simply aimed at how to get the robot to move about in a controlled and purposeful fashion. Once this hurdle is surmounted, attention can be turned to collision avoidance, wherein the system learns not to run into things while enroute. The proud builders soon realize the robot can perform admirably for some finite length of time but eventually will get lost, whereupon developmental focus shifts to navigational referencing. Applications are tacked on later, sometimes almost as an afterthought.

Accordingly, following some general background discussions in Chapter 1, we start by taking a look in Chapter 2 at the sensors employed in vehicle dead reckoning, with a careful analysis of potential error sources. Tactile and proximity sensors are introduced next in Chapter 3, providing a rudimentary capability to at least detect potential obstructions in time to stop. Chapters 4 through 7 provide an overview of the various distance measurement techniques available, such as triangulation, time of flight, frequency modulation, phase-shift measurement, and interferometry. Related discussion of implementation in the acoustical, radio frequency, and electro-optical domains is presented in Chapters 8 and 9, with a special emphasis on the various factors affecting performance.

This approach hopefully provides a good foundation for later examining how such non-contact ranging sensors are employed in specific roles, first and

foremost being in support of collision avoidance (Chapter 10). Navigational referencing, the subject of Chapters 11 through 16, is addressed in considerable detail as it represents one of the biggest remaining stumbling blocks to successful fielding. A few representative samples of application-specific sensors are treated in closing in Chapter 17.

In retrospect, there is considerably less emphasis than I originally intended on image-based systems, as the subject of machine vision quite obviously could be the focus of a book all in itself. And since a number of distinguished individuals far better qualified than myself have in fact taken that very objective to task, I have purposely limited discussion in this volume, and concentrated instead on various alternative (and often less complex) sensing strategies less documented in the open literature. Reference is made throughout the text to candidate systems, both commercially available and under development, in hopes of complementing theory of operation with some practical lessons in real-world usage. These illustrative examples are called out under separate headings where the discussion becomes rather detailed.

I have very much enjoyed the preparation of this manuscript, both in terms of what I learned in the process and the new contacts I made with other researchers in this exciting field. I hope the results as presented here will be useful in promoting the successful employment of mobile robotic systems through increased awareness of available supporting technologies.

H.R. Everett
San Diego, CA

Acknowledgments

A number of people have assisted me in my educational and research endeavors over the years and collectively contributed to making this book a reality. I would like to express my heart-felt appreciation to:

My uncles, Gene Everett and Joe Hickey, who introduced me to electronics at an early age.

My high school geometry teacher, Mrs. Nell Doar, for providing discipline, inspiration, and the mathematical foundation upon which I was to build.

Professor Robert Newton, my thesis advisor at the Naval Postgraduate School, who made it possible for me to pursue a rather unorthodox topic in the field of mobile robotics.

Vice Admiral Earl B. Fowler, USN (Ret.) for creating a robotics program office within the Naval Sea Systems Command, and giving me a job after graduate school.

Dr. Anita Flynn of MIT for all the late nights and weekends we spent hacking code and building our own sensors in my basement in Virginia.

Gary Gilbreath of the Naval Command Control and Ocean Surveillance Center for transforming ROBART II into a truly intelligent machine.

My son, Todd Everett, for his tremendous help in generating all the graphics used in the figures.

All those people kind enough to review this manuscript in the various stages of its completion, offering helpful insights on how best to present the material: Ron Arkin, Johann Borenstein, Fernando Figueroa, Anita Flynn, Doug Gage, Bob Garwood, Tracy Heath, Susan Hower, Robin Laird, Richard Langley, Richard Lao, Larry Mathies, and Hoa Nguyen.

In addition, portions of the material presented in Chapters 4 through 7 were previously published in *Sensors* and later *Robotics and Autonomous Systems* magazines, and updated in this book with their kind permissions.

1
Introduction

The past several years have brought about a tremendous rise in the envisioned potential of robotic systems, along with a significant increase in the number of proposed applications. Well-touted benefits typically associated with the installation of fixed-location industrial robots are improved effectiveness, higher quality, reductions in manpower, as well as greater efficiency, reliability, and cost savings. Additional drivers include the ability to perform tasks of which humans are incapable, and the removal of humans from demeaning or dangerous scenarios.

The concept of mobility has always suggested an additional range of applications beyond that of the typical factory floor, where free-roaming robots move about with an added versatility fostering even greater returns. Early developmental efforts introduced potential systems for fighting fires, handling ammunition, transporting materials, and patrolling warehouses and storage areas, to name but a few. Most of the resulting prototypes met with unexpected difficulty, primarily due to an insufficient supporting technology base. Even today, after decades of extensive research and development, the successful application of mobile robots remains for the most part an elusive dream, with only a small handful of fielded systems up and running.

While a number of technological hurdles have impeded progress, the three generally regarded as having the greatest impact are: 1) *computational resources*, 2) *communications*, and 3) *sensors*. The first two areas have been addressed for a variety of commercial reasons with remarkable progress. In just a little over 10 years we have transitioned from *6502*- and *Z80*-based personal computers running under *C/PM* with a maximum 64-kilobyte address space, to *Pentium*-based systems running at 90 MHz and addressing up to 32 megabytes of memory. The recent surge in popularity of laptop computers has provided an extra impetus, with special emphasis on reduced power consumption and extended battery life. Wireless local area networks and spread-spectrum technology have likewise advanced in kind, to the point where there are now a number of vendors offering full-duplex Ethernet-compatible high-speed datalinks with ranges of several miles.

The third category of *sensors* now stands somewhat alone as the most significant technical challenge still facing developers, due primarily to a lack of high-volume applications. While there has indeed been some carry-over sensor technology from advances in flexible automation for manufacturing, it has fallen far short of the explosive growth seen in the computer and communications industries. Successful adaptation of what progress has been made is further hampered by the highly unstructured nature of a mobile robot's operating environment. Industrial process-control systems used in repetitive manufacturing scenarios, in contrast, rely on carefully placed sensors that exploit the target characteristics. Background conditions are arranged to provide minimal interference, and often aid in the detection process by purposely increasing the *on-off* differential or contrast. Unfortunately, such optimized configuration control is usually no longer possible once mobility is introduced as a factor in the equation.

Consider for example the issue of collision avoidance: any mobile robot intended for real-world operation must be capable of moving around without running into surrounding obstructions. In practice, however, the nature and orientation of obstacles are not known with any certainty; the system must be capable of detecting a wide variety of target surfaces under varying angles of incidence. Control of background and ambient conditions may not be possible. *A priori* information regarding the relative positions, orientations, and nature of objects within the sensor's field of view becomes very difficult to supply.

The situation only worsens when the operating environment is taken outdoors, for a number of reasons. To begin with, problems of scale introduce a need for additional range capability that significantly adds to system complexity and cost. While an indoor collision avoidance system may need to see only 4 to 6 feet in front of the robot, for example, exterior scenarios typically require effective coverage over a 20- to 30-foot span, sometimes more. In addition, the outdoor environment often poses additional complicating hazards to safe navigation (i.e., terrain traversabilty, oncoming traffic, atmospheric obscurants) that demand appropriate engineering solutions not even addressed on interior systems.

On the positive side, worldwide interest in a rapidly expanding field known as *intelligent vehicle highway systems (IVHS)* has already created a huge potential market for sensors to address many of these problems as faced by the automotive industry (Catling, 1994). Lower-volume autonomous mobile robot applications are sure to benefit from the inevitable spin-off technologies that have already begun to emerge in the form of low-cost laser and millimeter-wave systems, for example. Many of these new and innovative products will be presented as illustrative examples in the following chapters, in hopes of further stimulating this technology-transfer process.

1.1 Design Considerations

The problems confronting most mobile robotic development efforts arise directly from the inherent need to interact with the physical objects and entities in the

environment. The platform must be able to navigate from a known position to a desired new location and orientation, avoiding any contact with fixed or moving objects while en route. There has been quite a tendency in early developmental efforts to oversimplify these issues and assume the natural growth of technology would provide the needed answers. While such solutions will ultimately come to pass, it is important to pace the evolution of the platform with a parallel development of the needed collision avoidance and navigation technologies.

Fundamental in this regard are the required sensors with which to acquire high-resolution data describing the robot's physical surroundings in a timely yet practical fashion, and in keeping with the limited onboard energy and computational resources of a mobile vehicle. General considerations for such sensors are summarized below:

- *Field of view* — Should be wide enough with sufficient depth of field to suit the application.
- *Range capability* — The minimum range of detection, as well as the maximum effective range, must be appropriate for the intended use of the sensor.
- *Accuracy and resolution* — Both must be in keeping with the needs of the given task.
- *Ability to detect all objects in environment* — Objects can absorb emitted energy; target surfaces can be specular as opposed to diffuse reflectors; ambient conditions and noise can interfere with the sensing process.
- *Real-time operation* — The update frequency must provide rapid, real-time data at a rate commensurate with the platform's speed of advance (and take into account the velocity of other approaching vehicles).
- *Concise, easy to interpret data* — The output format should be realistic from the standpoint of processing requirements; too much data can be as meaningless as not enough; some degree of preprocessing and analysis is required to provide output only when action is required.
- *Redundancy* — The system should provide graceful degradation and not become incapacitated due to the loss of a sensing element; a multimodal capability would be desirable to ensure detection of all targets, as well as to increase the confidence level of the output.
- *Simplicity* — The system should be low-cost and modular to allow for easy maintenance and evolutionary upgrades, not hardware-specific.
- *Power consumption* — The power requirements should be minimal in keeping with the limited resources on board a mobile vehicle.
- *Size* — The physical size and weight of the system should be practical with regard to the intended vehicle.

The various issues associated with sensor design, selection, and/or integration are complex and interwoven, and not easily conveyed from a purely theoretical perspective only. Actual device characterization in the form of performance

validation is invaluable in matching the capabilities and limitations of a particular sensor technology to the application at hand. Most manufacturers of established product lines provide excellent background information and experienced applications engineers to assist in this regard, but some of the more recently introduced devices are understandably a bit behind the power curve in terms of their documented performance results. In addition to the general theory of sensor operation, therefore, this book attempts to provide the reader with some important exposure to the practical experiences and insights of system developers involved in this rapidly evolving field.

1.2 The Robots

I consider myself very fortunate to have been personally associated with the development of a number of mobile systems over the past 30 years and will refer to several of these throughout this text for purposes of illustration. The following introductory sections are intended to provide a brief overview of these robots for those interested in the background. It is somewhat amusing to note the advancements made in the supporting technologies over this time span. The bottom line, however, is that the most sophisticated mobile robots in existence today still fall orders of magnitude short in achieving the utility and perception of their most inept human counterparts. While we have come a long way as developers, there is still much left to be done.

1.2.1 WALTER (1965-1967)

WALTER (Figure 1-1) was a 5-foot-tall anthropomorphic robot I constructed my sophomore year in high school as a science fair entry. Strictly a teleoperated system with no onboard intelligence, WALTER was capable of forward or reverse travel, using two 8-inch rear drive wheels made of ¾-inch plywood and a pair of 2-inch roller-skate wheels in front for steering. The steering mechanism was solenoid-actuated under *bang-bang* control, with a spring-loaded center default position. A 20-foot umbilical tether supplied 117-volt AC power from the control station shown on the left side of the photo.

The right arm was capable of two-degree-of-freedom movement (elbow and shoulder) driven by linear actuators constructed from ¼-inch threaded rod, powered by a sewing machine motor and a kitchen mixer, respectively. The left arm had only a single degree of freedom at the elbow (I ran out of motors), its associated linear actuator being coupled to the prime mover from an old movie projector. All the motors were single-speed series-wound universal type controlled (by onboard relays) from the remote operator console. The linear actuators were coupled to their respective joints by tendons made from bicycle hand-brake cables.

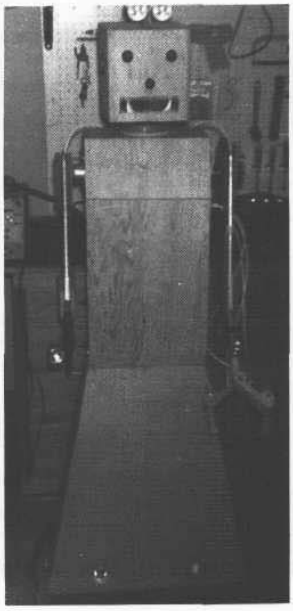

Figure 1-1. *WALTER* (circa 1964) was a teleoperated anthropomorphic robot constructed as a high school science fair entry.

The left and right grippers were also different (it's no fun building the same thing twice...), but similar in that they both lacked wrist movement. The right gripper was fashioned from a 10-inch fuse puller, aligned for grasping objects oriented in the horizontal plane. The left gripper was somewhat more complex, constructed from ¼-inch hardwood with two degrees of freedom as illustrated in Figure 1-2, and oriented to grasp vertical objects. All gripper joints were tendon-driven by cables spring-coupled to powerful solenoids removed from innumerable washing machines.

WALTER's head could pan left or right approximately 45 degrees either side of center, driven through tendons by a linear actuator mounted in the base to keep the center of gravity low. Load-bearing joints (head pan axis, shoulder, elbows) were fashioned from ball-bearing roller-skate wheels. There was a photocell mounted on top of the head to monitor ambient light conditions, and, of course, the obligatory flashing lamps for eyes and nose. Two microphone ears and a speaker behind the mouth opening provided for remote communications via the telephone handset shown in Figure 1-1. (After all, 20 feet is a long way to yell when we have the technology.)

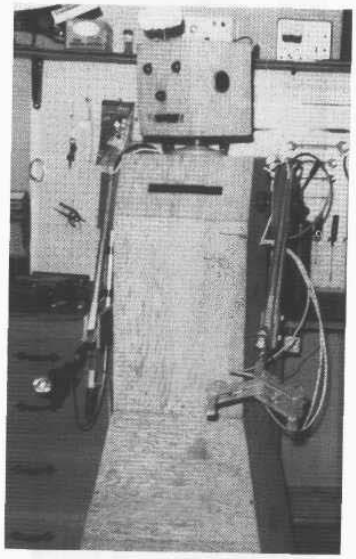

Figure 1-2. WALTER'S left gripper was tendon actuated with two degrees of freedom.

The electronics for both the robot and the control console were vacuum-tube based. One interesting submodule was a capacity-operated relay (see Chapter 3) coupled to a touch sensor in the right gripper. The sole purpose of this circuitry was to discourage pulling and prodding by curious onlookers; any stray finger that poked its way into the open claw would be met by a startling and decidedly effective warning snip. The resounding thump of the actuating solenoid only served to accentuate the message.

WALTER met his demise one day in 1967 at the hands of our cleaning lady (bless her heart). I had been experimenting with some Japanese six-transistor portable radios that sold at the time for around five dollars apiece, trying to come up with a low-cost radio control scheme. The idea was to tune each of the four receivers to a blank spot on the AM dial, and use a continuous-tone RF transmitter that could be switched to any one of these four frequencies. Half-wave rectifiers attached to the audio outputs of the individual radios activated sensitive meter relays that controlled the forward, reverse, left, and right power relays in the drive circuitry.

As fate would have it, the unsuspecting maid bravely entered the confines of my bedroom workshop one day when I was not at home and turned on the ancient pre-World-War-II *Lewyt* vacuum cleaner my dad had rebuilt six times just in my

brief lifetime. The motor brushes had long since worn down to their springs, which arced across the pitted commutator segments with such intensity that all TV and radio reception for two blocks was blanked out whenever the machine was running. WALTER's radios responded instantly to this rich broad-band interference, randomly applying power in a mindless fashion to drive motors and steering solenoids alike. The robot lurched forward, twisting and turning, motors whining and solenoids clacking, only to be immediately decapitated with one mighty swing of a *Lewyt* rug sweeper. When I got home the vacuum was still running, WALTER was a total loss, the front door was swinging on its hinges, and the maid had vanished, never to return.

1.2.2 CRAWLER I (1966-1968)

I had been bitten by the bug, it seemed, and was now fascinated with the idea of building a free-roaming robot unencumbered by any sort of tether. There was little point in trying to refurbish WALTER; structural damage notwithstanding, all the electrical components were rated for 117 volts AC. My next creation had to be battery powered. And so I began to amass an impressive collection of DC motors, relays, and other diverse components while sorting out the design in my head. The end result was CRAWLER I (Figure 1-3), intended to be my junior-year science fair project. (The eagerly anticipated event was unfortunately canceled due to faculty indifference.)

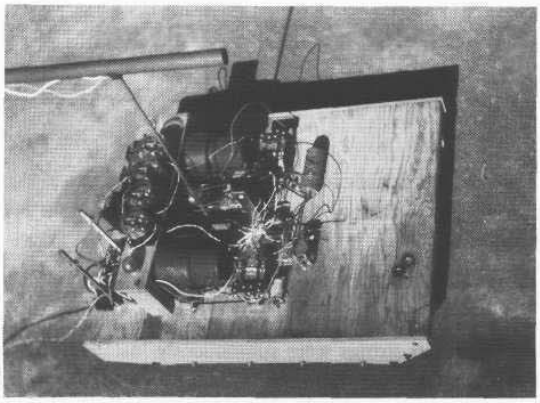

Figure 1-3. Photo of *CRAWLER I* (circa 1966) in early stages of development.

I had also decided to build a tracked vehicle for improved maneuverability. Two 24-volt DC gearmotors from a aircraft surplus catalog were mounted on a 18- by 13-inch plywood base (Figure 1-4), driving left and right tracks fashioned from 1.5-inch rubber timing belts turned inside out. Control was again provided by relays, but the motors each had centrifugal speed-limiting switches that could be adjusted to achieve straight-line travel. By adding an override circuit on the stationary side of the slip rings that fed the centrifugal governor, it was possible to momentarily boost the motor rpm to maximum. *Skid steering* was achieved by providing differential speed commands in this fashion or stopping one motor altogether. The vehicle could also turn in place by reversing one track.

The tough part in building an autonomous vehicle, of course, lies in how to control its motion, made even tougher still in an era that predated microprocessors and low-cost sensors. I had in mind a platform that would drive around until it encountered an object, then alter course in an intelligent fashion. I also wanted it to automatically recharge the onboard lead-acid motorcycle batteries when they ran low. Like most engineers, I tackled the tougher issue first: automatic recharging. I settled on a beacon homing scheme and elected to use an ordinary light bulb as the source. (It would take me some time, and several follow-on robots, to shake this mind set.) Details of this tracking and homing design are presented later in Chapter 15.

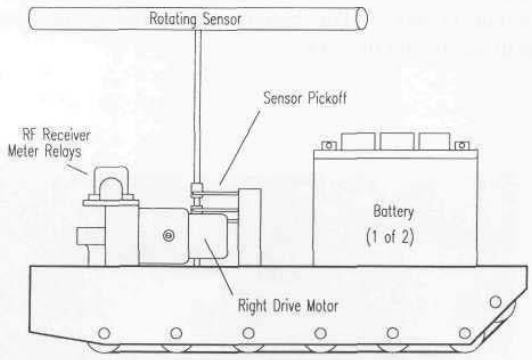

Figure 1-4. A rotating photocell sensor was used on *CRAWLER I* to locate and track a homing beacon for automatic recharging.

Providing for truly autonomous operation meant adding some type of collision avoidance sensor and implementing a scheme of intelligent reaction. Tactile sensors made from guitar strings were subsequently installed on the four corners of the platform to support this task and are described in Chapter 3. Intelligent response was another matter; single-chip microcontrollers were not yet even a figment of anyone's imagination in those days. My Hollywood-inspired image of a computer centered around a lot of flashing lights and punched cards. I had

already wired dozens of very impressive indicator lamps in parallel with the relay coils of the CRAWLER's logic and control circuitry (for diagnostic purposes, of course). Operating the CRAWLER with the four-channel radio control developed on WALTER had quickly become boring, so it seemed the appropriate thing to do was build a punched-card reader.

The robot's environment could be simplistically described by four state variables associated with the tactile sensors situated at each of the four corners of the platform. By comparing these sensor input states to a 4-bit address field punched into each card, the correct response to any particular scenario could be read from the output section of the one card with an address code matching the specified input conditions. The robot would simply stop whenever input conditions changed state and cycle the cards until finding a match. The preprogrammed response (i.e., drive and steering commands) to the new conditions would be punched into the 4-bit output field of the correct card.

I was really excited about the prospect of building this card reader and made pretty fair progress using modified index cards with eight photocells to detect ¼-inch holes made by a standard office hole punch. An actual 3.5- by 8-inch card is shown in Figure 1-5; the top row of holes represented the inputs, while the bottom row controlled the outputs. The individual illumination sources for the eight opposing photocells were 3-volt pilot lamps, wired in series to ensure the entire string would extinguish to prevent faulty readings if any single bulb burned out. The lamps were powered by the 12-volt battery at half their rated filament voltage to ensure extended life, and the reduced light output prevented premature activation of the photodetectors through the thin index-card paper. But the mechanics associated with reliably recycling the stack of cards (once all had been read) proved too much for my limited shop facilities, so I resorted to using a 12-inch circular disk of poster paper traced from a 33-rpm record album.

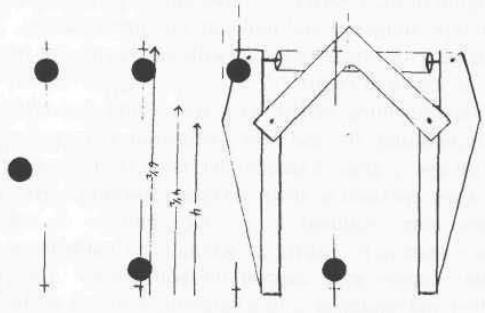

Figure 1-5. An actual 3- by 5-inch card used on *CRAWLER I* showing the two rows of punched holes representing input and output data. The sketch on the back is a preliminary gripper design that was abandoned in favor of the vise-grip implementation shown later in Figure 1-7

This approach greatly simplified matters. The address and output fields were aligned along the radial axis of the disk with 16 possible states as shown in Figure 1-6, with the most significant bit towards the outer periphery. The disk would rotate at 6 rpm while the photocells looked for a hole pattern corresponding to the sensor input states. When a match was found, the disk drive motor was disabled and the output field would be read, thus determining the desired control relay states for left and right track drive and direction. The output holes were punched in radial columns offset exactly 78.75 degrees from their associated input columns to allow sufficient room for the two photocell arrays. The circular card was secured to a rubber-covered drive capstan with a ¼-inch wingbolt and washer.

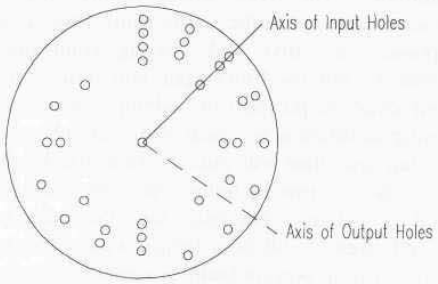

Figure 1-6. Mechanical problems with the stacked-card transport mechanism forced a switch to the circular card format shown above. Punched output holes (not shown) were inserted between the input address fields, offset approximately 90 degrees.

1.2.3 CRAWLER II (1968-1971)

All the added features (particularly the 12-inch disk reader) necessitated a complete repackaging of the *CRAWLER's* mechanical layout, so I elected to scrap the plywood prototype altogether and build an aluminum chassis. The result was *CRAWLER II*, basically the same size, but with the electronics implemented in a layered approach as shown in Figure 1-7.

I had begun experimenting earlier with some miniature hydraulic cylinders fashioned by encapsulating 30- and 50-cc irrigation syringes inside of copper-tubing sheaths with epoxy glue. Considerable force could be generated with one of these devices when operated at about 100 psi; solenoid valves from discarded washing machines were modified to provide control. A surplus chemical-injection pump was used to pressurize an accumulator made from a 4-inch length of 3-inch-diameter copper pipe capped on both ends. CRAWLER II was eventually modified and equipped with a hydraulic arm and gripper configuration as illustrated in Figure 1-7. The gripper force was quite powerful. While attempting to explore the limits of remote-operator dexterity, I once squeezed the

locomotive of my brother's train set just a wee bit too hard, rendering it no longer compatible with H-O gauge track.

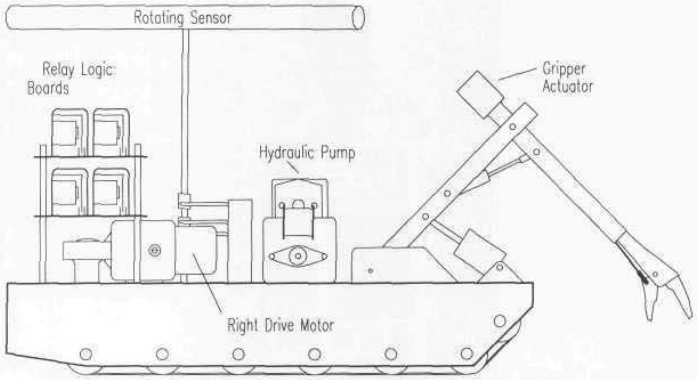

Figure 1-7. *CRAWLER II* (shown here without the circular disk reader) was a teleoperated platform equipped with a 2-DOF hydraulic gripper.

Unfortunately, the bulky disk reader and the manipulator would not both fit on the platform at the same time, and the modified hydraulic components were all rated for 117 volts AC. In addition, there was essentially no way to control the new manipulator in an autonomous fashion, so CRAWLER II had to revert back to tethered control. The few photographs I have of CRAWLER I were taken by one of my high school buddies who owned a Polaroid camera; since most of the CRAWLER II development was performed while I was away at college, I regrettably don't have any pictures. Work on CRAWLER II ceased my junior year, when I "borrowed" the onboard logic control unit to automate our (very) mechanized homecoming display at Georgia Tech.

1.2.4 ROBART I (1980-1985)

ROBART I (Figure 1-8) was my thesis project at the Naval Postgraduate School in Monterey, CA (Everett, 1982a; 1982b). Its assigned function was to patrol a normal home environment, following either a random or set pattern from room to room, checking for unwanted conditions such as fire, smoke, intrusion, etc. The security application was chosen because it demonstrated performance of a useful function and did not require an end-effector or vision system, significantly reducing the required system complexity. Provision was made for locating and connecting with a free-standing recharging station when battery voltage began running low (Figure 1-9). Patrols were made at random intervals, with the majority of time spent immobile in a passive intrusion-detection mode to conserve power.

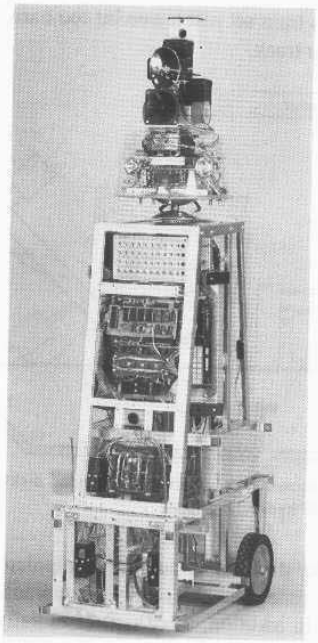

Figure 1-8. *ROBART I* was a fully autonomous interior security robot (courtesy Naval Surface Weapons Center).

A Synertek *SYM-1* single-board computer formed the heart of the onboard electronics. Speech synthesis (to allow the system to announce any unwanted conditions detected in the course of a random patrol) was implemented through National Semiconductor's *Digitalker DT1050* synthesizer chip. Two sets of vocabulary instructions were stored on EPROMs for a total vocabulary of 280 words. A fixed vocabulary was chosen over an unlimited vocabulary created through use of phonemes in light of the greatly decreased demand on the onboard microprocessor in terms of execution time and memory space.

The software maintained the robot in one of two modes of operation: *Alert Mode* or *Passive Mode*. In the *Passive Mode*, the majority of sensors were enabled, but a good deal of the interface and drive control circuitry was powered down to conserve the battery. The robot relied on optical motion detection, ultrasonic motion detection, and hearing to detect an intruder, while at the same time monitoring for vibration (earthquake), fire, smoke, toxic gas, and flooding (Everett, 1982a). Some of these inputs were hard-wired to cause an alert (switch from *Passive Mode* to *Alert Mode*), whereas others had to be evaluated first by software that could then trigger an alert if required. Either mode could be in

effect while recharging, and recharging could be temporarily suspended if conditions so warranted.

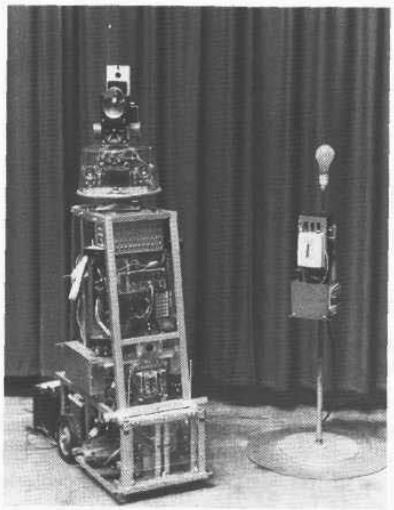

Figure 1-9. An optical homing beacon mounted on top of the recharging station was used to guide *ROBART I* to the charger when a low-battery condition was detected.

Recharging was handled automatically. The 12-volt 20-amphour lead-acid battery gave about six hours of continuous service and then required 12 hours of charge. Roughly one hour of power was available to locate the charging station (by means of a visual homing beacon) after the battery monitor circuits detected a low condition. The homing beacon was activated by a coded signal sent out from an RF transmitter located atop the robot's head, and the recharging supply was activated only when a demand was sensed after connection (Figure 1-10). The robot could elect to seek out the recharging station before a low battery condition actually arose, such as between patrols.

The software employed in homing on the recharger and effecting a connection was able to deal with a multitude of problems that could arise to hinder the process. Provision was made to skirt around obstacles between the robot and the recharging station. If, as a result of a collision avoidance maneuver, the robot were oriented with respect to the charger so as to preclude a successful docking, the vehicle would back up and realign itself before continuing. The robot could also tell when a return from a forward-looking proximity detector was due to the presence of the recharging station, so the software would not try to steer the platform away. (The collision-avoidance strategy will be discussed in more detail later in Chapter 10.)

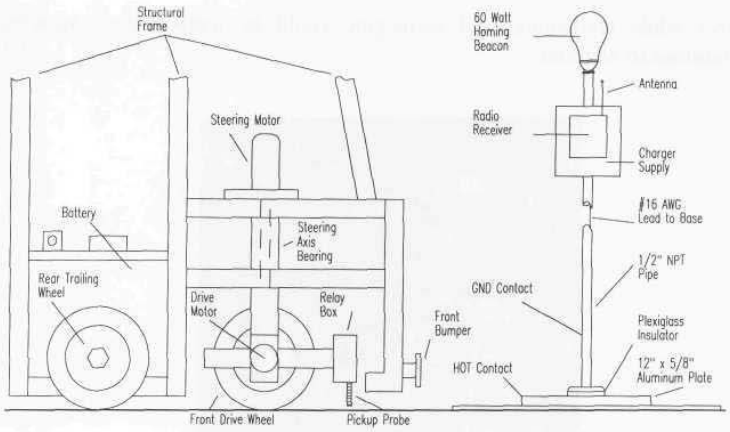

Figure 1-10. Diagram of the optical homing beacon used by *ROBART I* for automatic battery charging (adapted from Everett, 1982a).

A special near-infrared proximity sensor mounted on the head provided reliable detection of diffuse wall surfaces for ranges out to 6 feet. This sensor could be positioned at any angle up to 100 degrees either side of centerline by panning the head and was extremely useful in locating open doors and clear paths for travel. Excellent bearing information could be obtained, allowing this sensor to establish the location of the edge of a doorway, for example, to within 1 inch at a distance of 5 feet.

The hallway navigation scheme employed on ROBART I was based in part on the concept of beacon tracking. The recharging station optical beacon was suitably positioned in a known location to assist the robot in entering the hallway. Once in the hallway, the robot would move parallel to the walls in a reflexive fashion, guided by numerous near-infrared proximity sensors. General orientation in the hallway could be determined by knowing which direction afforded a view of the beacon. With *a priori* knowledge of where the rooms were situated with respect to this hallway, the robot could proceed in a semi-intelligent fashion to any given room, simply by counting off the correct number of open doorways on the appropriate side of the hall.

ROBART I was purposely intended to be a crude and simplistic demonstration of technical feasibility and was built on an extremely limited budget using oversimplified approaches. This philosophy assumed that if the concept could be successfully demonstrated under such primitive conditions of implementation, a reasonable extrapolation would show promise indeed for a more sophisticated second-generation version. (I had actually started work on this follow-on prototype just before leaving the Naval Postgraduate School in 1982.) As my interests shifted more in this direction, ROBART I was loaned to the Naval Surface Weapons Center in White Oak, MD, entrusted to the watchful care of an

MIT co-op student by the name of Anita Flynn (now a famous pioneer in the field of microrobotics). All work with ROBART I ended in 1985, when the prototype was shipped to Vancouver, BC, for display in the *Design 2000* exhibit at *EXPO '86*.

1.2.5 ROBART II (1982-)

ROBART II (Figure 1-11) became the center of focus for the next several years in my basement workshop in Springfield, VA. The system basically performed the same functions as its predecessor but employed a multiprocessor architecture to enable parallel real-time operations. Optimization of performance was addressed through significantly increased sensor capability, distributed processing, and precise vehicle motion control. Upon my transfer in 1986 to the Naval Command Control and Ocean Surveillance Center (NCCOSC) in San Diego, CA (then Naval Ocean Systems Center), the prototype was made available to the Navy for use as a testbed in support of mobile robotics research. The initial development effort focused on two specific technology areas.

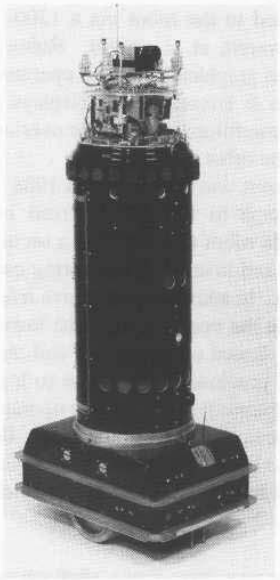

Figure 1-11. *ROBART II* was constructed in my basement in Springfield, VA between 1982 and 1986.

The first of these addressed the navigational concerns that were hindering successful implementation of a number of robotic applications requiring mobility (Gilbreath & Everett, 1988). Simply put, an autonomous vehicle must be able to determine its position and orientation in the workspace, plan a path to its intended destination, and then execute that path without running into any obstructions. Numerous proximity and ranging sensors were incorporated on the robot to support map generation, position estimation, collision avoidance, navigational planning, and terrain assessment, enabling successful traversal of congested environments with no human intervention.

The second thrust was aimed at producing a robust automated security system exhibiting a high probability of detection with the ability to distinguish between actual and nuisance alarms. ROBART II was therefore also equipped with a multitude of intrusion and environmental sensors in support of its role as an intelligent sentry. These sensors monitor both system and room temperature, relative humidity, barometric pressure, ambient light and noise levels, toxic gas, smoke, and fire. Intrusion detection is addressed through the use of infrared, optical, ultrasonic, microwave, and video motion detection, as well as vibration monitoring and discriminatory hearing.

All high-level planning and assessment software runs on a desktop IBM-PC/AT computer connected to the robot via a 1200-baud Repco RF modem as shown in Figure 1-12 (Everett, et al., 1990). Robot position as well as sensor monitoring are represented graphically for the operator. The security assessment software package (Smurlo & Everett, 1993) displays time-stamped sensor status as well as environmental conditions, and can be overlaid on live video transmitted from a camera on-board the robot.

The scope of involvement was broadened in 1988 to include enhancements to the world modeling scheme to incorporate fixed installation security sensors (thereby allowing a mobile robot to operate in a secure area already protected by installed motion sensors) and inventory monitoring capability (allowing the robot to detect missing objects). In addition, a *reflexive teleoperated control* capability was added in 1989 to free the operator from the lower-level concerns associated with direct teleoperation. Speed of the vehicle and direction of motion are servo-controlled by an onboard processor in response to local sensor inputs, but under the high-level supervisory control of the remote operator (Laird & Everett, 1990).

In spite of having been built at home from hobbyist-grade components, ROBART II has proven to be an amazingly reliable piece of equipment, with only four documented cases of hardware failure since officially coming to life in early 1983. These included:

- A cold solder joint on a drive-motor shaft encoder.
- A defective power transistor in a drive-motor H-bridge amplifier.
- An oxidized variable capacitor in the CPU clock circuit for the sonar controller.
- An intermittent optical motion detector in the security sensor suite.

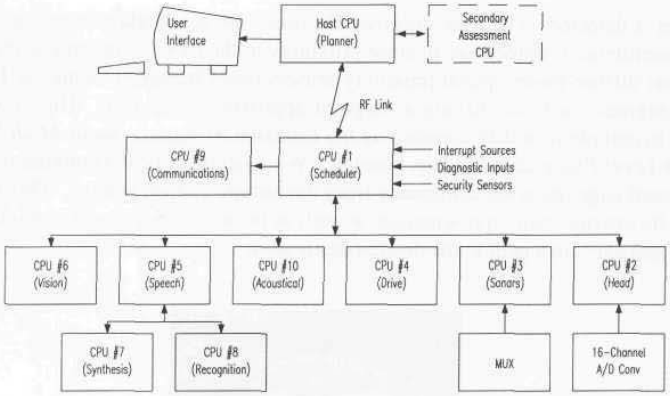

Figure 1-12. Block diagram of the computer architecture employed on *ROBART II*.

This record is somewhat noteworthy, considering the workout given the system over its 13-year lifetime to date; records indicate the robot performed in 53 live demonstrations for visiting students, faculty, scientists, and government officials in 1987 alone. ROBART II has been continuously on line now without a power interruption since sometime back in 1988.

1.2.6 MODBOT (1990-)

The *Modular Robotic Architecture* was developed by NCCOSC as a generic platform control system offering developers a standard set of software and hardware tools that could be used to quickly design modular robotic prototypes with minimum start-up overhead (Smurlo & Laird, 1990). The concept facilitates customization of a testbed system by providing sensor, actuator, and processing modules that can be configured on demand as required by the particular needs of the application being addressed. The ability to later accept newer modules of increasing sophistication provides for evolutionary growth potential, ensuring maximum effective service life before the hardware becomes obsolete.

The *ModBot* (Figure 1-13) is an example of a mobile robot implemented under this modular concept, employing several independent modules of varying intelligence and sophistication connected together in a generalized distributed network. The platform is made up of a detachable base with accompanying power source and various sensor, actuator, and processing modules. Each of these modules enables the robot to obtain and process different information about its surroundings.

The *Collision Avoidance Sonar Module* is active whenever the robot is in motion. It continuously looks for obstacles within a predefined distance and reports back to the *High-Level Processing Module* for appropriate action if an

object is detected. The *Near-Infrared Proximity Sensor Module* is another means of determining if objects are in close proximity to the robot. This ring contains 11 Banner diffuse-mode optical proximity sensors (see Chapter 3) facing the forward 180 degrees, each one having a range of approximately 3 feet. This module is used to complement data obtained by the *Collision Avoidance Sonar Module*. The *High-Level Processing Module*, housing a WinSystems AT286 computer mounted in a card cage, receives commands from the remote control station. This module uses its internal map representation, as well as information from other modules, to plan and execute a path to the desired destination.

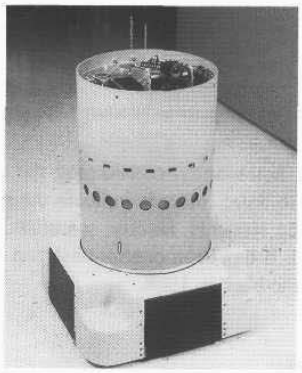

Figure 1-13. The *ModBot* is an autonomous robotic testbed that can be quickly reconfigured as needed to support a variety of potential research issues (courtesy Naval Command Control and Ocean Surveillance Center).

During data transfers, the *Control Station Module* communicates with the *ModBot* via the *Communications Module*. An RS-232 umbilical cable was initially used during the early stages of development and later replaced by an OCI *LAWN* spread-spectrum RF link. Some exploratory work was also performed using a full-duplex near-infrared datalink made by STI. The modular nature of the robot allowed the *Communications Module* to be upgraded without any other reconfiguration necessary to the rest of the *ModBot* systems.

The flexibility and extendibility of the *ModBot* architecture have made it a valuable testbed for the pursuit of new ideas and applications involving robot mobility. One of the first was a significantly upgraded version of the robotic security concept carried over from ROBART II. The *Intrusion Detection Module* is used to detect intruders in the vicinity of the robot and reports the bearing back to a remotely located *Control Station Module*. The *Intrusion Detection Module* consists of ultrasonic, passive-infrared, and microwave motion detectors which cover the full 360-degree surrounding area. A video motion detector in this module also receives information from the acoustic and video sensors on the

Stereoscopic Pan-and-Tilt Module to determine if an intruder is present. Audio and composite video signals are transmitted back to the operator via two separate analog RF links.

1.2.7 USMC TeleOperated Vehicle (1985-1989)

The *TeleOperated Vehicle (TOV)* was developed for the US Marine Corps by NCCOSC as part of the *Ground Air TeleRobotic Systems (GATERS)* program, and continued under the Unmanned Ground Vehicle Joint Program Office (UGV/JPO) *Ground-Launched Hellfire* program (Metz, et al., 1992). I served as Chief Engineer on the latter effort from July 1988 until October of the following year, during which time we designed and built a hardened second-generation version of the vehicle to support a major milestone demonstration in September 1989. During this series of live-fire exercises at Camp Pendelton, CA, the *TOV* system achieved a perfect record of eight direct hits with *Hellfire* missiles and four direct hits with laser-guided *Copperhead* projectiles.

Figure 1-14. One of three remotely driven reconnaissance, surveillance, and target acquisition (RSTA) vehicles developed by NCCOSC for the USMC *TeleOperated Vehicle (TOV)* program (courtesy Naval Command Control and Ocean Surveillance Center).

Three distinct modules for mobility, surveillance, and weapons firing allow the remote *TOV* platforms to be configured for various tactical missions (Aviles, et al., 1990; Metz, et al., 1992). The first, the *Mobility Module*, encompasses the necessary video cameras and actuation hardware to enable remote driving of the HMMWV. Figure 1-14 shows *TOV-2 (TeleOperated Vehicle 2)*, one of three platforms operated from a control van several kilometers away. A robot in the

driver's seat of the HMMWV was slaved to the operator's helmet back in the control van so as to mimic his head movements (Martin & Hutchinson, 1989). If the helmet turned to the left and down, so did the slave robot in the remote vehicle. The two cameras on the robot that look like eyes feed two miniature video monitors on the operator's helmet, so that the operator would see in the van whatever the robot was viewing out in the field.

Two microphones on either side of the head served as the robot's ears, providing the operator with stereo hearing to heighten the *remote-telepresence* effect. Electric and hydraulic actuators for the accelerator, brakes, steering, and gearshift were all coupled via a fiber-optic telemetry link to identical components at the driver's station inside the control van (Figure 1-15). Actual HMMWV controls were replicated in form, function, and relative position to minimize required operator training (Metz, et al., 1992). After a few minutes of remote driving, one would actually begin to feel like one was sitting in the vehicle itself. A low-tension 30-kilometer cable payout system dispensed the fiber-optic tether onto the ground as the vehicle moved, avoiding the damage and hampered mobility that would otherwise arise from dragging the cable (Aviles, et al., 1990).

Figure 1-15. The *TOV Control Van* consists of a HMMWV-mounted environmental shelter containing three operator control stations and a fourth supervisor station (courtesy Naval Command Control and Ocean Surveillance Center).

Probably the most bizarre feeling I had driving one of these things remotely was operating the gearshift. You naturally want to look down at the shift lever when you grab it, which of course causes the slave robot at the other end to look down also (Figure 1-16). Your eyes see the shift lever on the remote vehicle, while your hand feels the shift knob in the control van. The problem is your hand doesn't appear in the video that your eyes see. When you move the lever, you feel

it move and see it move in the video, but there's no hand there doing the moving. The human brain automatically fuses sensory inputs from two different sources, several kilometers apart, back into one composite image.

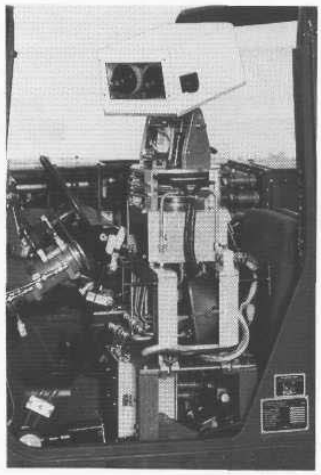

Figure 1-16. The remote slave robot is situated in the HMMWV driver's seat just behind the hydraulically actuated steering wheel (courtesy Naval Command Control and Ocean Surveillance Center).

The *Surveillance Module* was basically a glorified pan-and-tilt unit transporting a high-resolution sensor package, all mounted on a scissors-lift mechanism that could raise it 12 feet into the air. The sensor suite weighed approximately 300 pounds and consisted of a low-light-level zoom camera, an *AN/TAS-4A* infrared imager (FLIR), and an *AN/PAQ-3 MULE* laser designator. The remote operator would look for a tank or some other target with the camera or the FLIR, then switch over to the designator to light it up for a laser-guided *Hellfire* missile or *Copperhead* artillery round.

The *Weapons Module* provided each of the designating vehicles with a remotely-actuated .50-caliber machine gun for self defense. In addition to pan-and-tilt motion, electric actuators were provided to charge the weapon, release the safety, and depress the trigger. A fixed-focus CCD camera was mounted just above the gun barrel for safety purposes. The weapon could be manually controlled with the joystick in response to video from this camera, or slaved to the more sophisticated electro-optical sensors of the *Surveillance Module*. One of the remote HMMWVs had a *Hellfire* missile launcher (Figure 1-17) instead of a *Surveillance Module*, the idea being that one platform looked and designated while the other did the shooting. Meanwhile, all the humans could be up to 15 kilometers away, which is important in chemical or biological warfare scenarios.

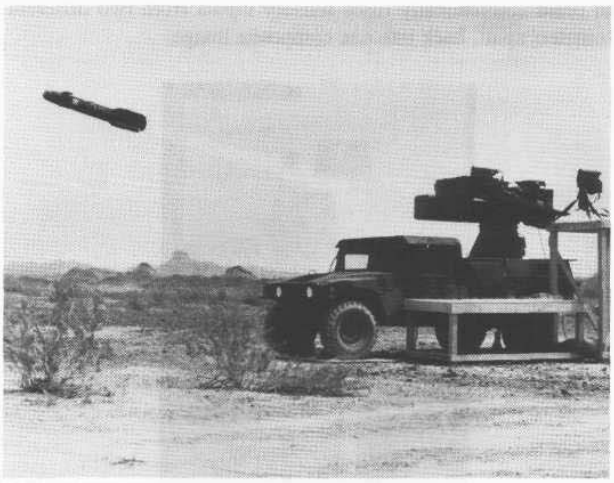

Figure 1-17. A Rockwell *Hellfire* missile comes off the rail in response to a remote command from the *TOV* operator located in the *Control Van* several kilometers away during demonstrations for a high-level Department of Defense audience at Camp Pendelton, CA, in September 1989 (courtesy Naval Command Control and Ocean Surveillance Center).

1.2.8 MDARS Interior (1989-)

The *Mobile Detection Assessment and Response System (MDARS)* program is a joint Army-Navy effort to develop a robotic security and automated inventory assessment capability for use in Department of Defense warehouses and storage sites. The program is managed by the US Army Physical Security Equipment Management Office, Ft. Belvoir, VA, with NCCOSC providing all technical direction and systems integration functions. Near-term objectives are improved effectiveness (with less risk) to a smaller guard force, and significant reduction in the intensive manpower requirements associated with accounting for critical and high-dollar assets. The initial *Interior* implementation involves eight Cybermotion *K2A Navmaster* robots (Figure 1-18) configured as remote security platforms (Laird, et al., 1993).

From a technical perspective, the objective is to field a *supervised robotic security system* which basically runs itself until an unusual condition is encountered that necessitates human intervention. This requirement implies the MDARS host architecture must be able to respond to exceptional events from several robots simultaneously. Distributed processing allows the problem to be split among multiple resources and facilitates later expansion through connection

of additional processors. The individual processors are connected via an *Ethernet* LAN (Figure 1-19) that supports peer-to-peer communications protocol. Distribution of function enables human supervision and interaction at several levels, while the hierarchical design facilitates delegation and assignment of limited human resources to prioritized needs as they arise.

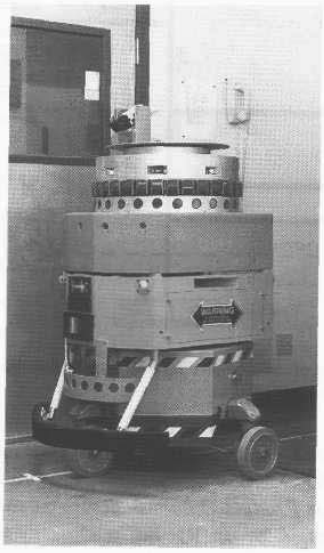

Figure 1-18. The early *MDARS Interior* feasibility prototype developed by the government employed the same modular-ring design used on the *ModBot* (courtesy Naval Command Control and Ocean Surveillance Center).

The *Supervisor* computer sits at the top of the hierarchy, responsible for overall system coordination and graphical display of the "big picture." The *Supervisor* has at its disposal a number of computing resources, such as one or more *Operator Displays*, two or more *Planner/Dispatchers*, a *Product Database* computer, and a *Link Server*. The *Supervisor* and *Operator Displays* have been similarly configured to provide the guard with consistent user-friendly visual displays. Both modules support a point-and-choose menu interface for guard-selectable options, commands, and navigational waypoints. The *Operator Display* allows a security guard to directly influence the actions of an individual platform, with hands-on control of destination, mode of operation, and camera functions. An optional *Virtual Reality Display* can be connected to the network if desired to provide a realistic three-dimensional model of the operating environment (Everett, et al., 1993).

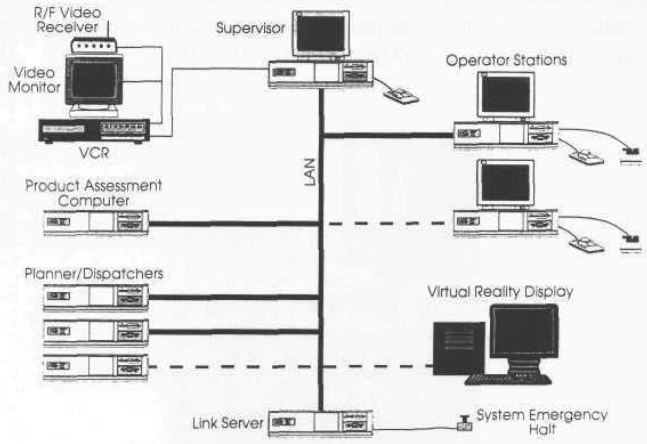

Figure 1-19. Block diagram of the *Multiple Robot Host Architecture* developed at NCCOSC for the coordinated control of multiple platforms.

The *Planner/Dispatcher* computers (an integration of the Cybermotion *Dispatcher* and the NCCOSC *Planner*) are responsible for navigation and collision avoidance. The *Product Database* computer maintains a listing of high-value inventory as verified by an RF tag reading system on board the robot, correlated to geographical location within the warehouse. The *Link Server* provides an interface to a spread-spectrum RF link between the host and the various robots, and maintains a blackboard data structure of robot status information for immediate retrieval by other computers on the LAN.

In October 1993 the MDARS Interior system began extensive test and evaluation in an actual semi-structured warehouse environment at Camp Elliott in San Diego, CA (Laird, et al., 1993). The original staring-array security sensor suite was replaced in December 1993 with the more optimal Cybermotion *SPI (Security Patrol Instrumentation)* module shown in Figure 1-20 (Holland, 1993). Developed as an outgrowth of a Cooperative Research and Development Agreement between Cybermotion and NCCOSC, the *SPI* uses a scanning configuration of microwave and passive infrared sensors to achieve the same 360-degree coverage at significantly reduced complexity and cost (DeCorte, 1994). A number of technical challenges associated with real-world operation have been uncovered and addressed during this rapid-prototyping test and development phase (Everett, et al., 1994; Gage, et al., 1995). Formal installation at an actual end-user site is scheduled to occur in the form of *Early User Experimentation* beginning in January 1997.

Figure 1-20. The *MDARS Interior* robot equipped with the Cybermotion *SPI Module* on patrol in the Camp Elliott warehouse in San Diego, CA (courtesy Naval Command Control and Ocean Surveillance Center).

1.2.9 Surrogate Teleoperated Vehicle (1990-1993)

The *Surrogate Teleoperated Vehicle (STV)*, a scaled-down follow-on version of the TOV concept, was developed under contract to NCCOSC by Robotic Systems Technology (RST), Inc., Westminster, MD, for the UGV/JPO in Huntsville, AL. The STV was intended to serve as a prototype system supporting the near-term development and evaluation of operational concepts for future unmanned ground vehicles, hence the terminology "Surrogate." A total of 14 vehicles was delivered to allow large numbers of military personnel to gain valuable hands-on robotics experience that could appropriately influence subsequent acquisition strategies. Figure 1-21 shows the STV fording a stream during the initial *Concept of Employment Exercise* at Fort Hunter Ligget, CA, in March 1992 (Metz et al., 1992).

From a technical perspective, the STV can be decomposed into four major inter-related subsystems: 1) the *Remote Platform*, 2) the *Mobility/RSTA Module*, 3) the *Operator Control Unit*, and 4) the *Communication System*.

The *Remote Platform* is built around a modified Polaris Industries *Big Boss* six-wheel-drive all-terrain vehicle measuring 117.5 inches long and 50.5 inches

wide (Myers, 1992). The principle power source is a water-cooled three-cylinder 25-horsepower diesel engine built by Fuji Heavy Industries, capable of propelling the vehicle at speeds up to 35 miles per hour. The output shaft of the diesel drives a modified Polaris *variable belt transmission* that in turn is coupled to a gearbox providing neutral, reverse, low-forward, and high-forward speed ranges (RST, 1993). An auxiliary 3-horsepower electric golf-cart motor is also coupled to the gearbox input shaft (via an electric clutch) to provide for extremely quiet movement during surveillance operations at limited speeds up to 4 miles per hour. The gearbox output shaft powers the tandem rear axles through an exposed chain-drive arrangement. Two 12-volt sealed lead-acid batteries supply all required DC power, recharged by a 24-volt 60-amp engine-driven alternator.

Figure 1-21. Shown here crossing a stream at Fort Hunter Ligget, the *Surrogate Teleoperated Vehicle* is capable of traversing through water up to 2 feet deep (courtesy Unmanned Ground Vehicle Joint Program Office).

In similar fashion to its TOV predecessor, the STV *Mobility/RSTA Module* consists of a number of *reconnaissance, surveillance, and target acquisition* sensors mounted on a pan-and-tilt mechanism situated atop an extending scissors-lift mast (Figure 1-22). In a stowed configuration, the mast is only 24 inches high, but can raise the sensor pod when desired to a full height of 15 feet above ground level. Adjustable pneumatic springs in the rear of the vehicle allow for stiffening of the suspension when the surveillance mast is elevated, thus reducing sway and jitter during RSTA operations (Metz, et al., 1992). The mobility and RSTA sensors include:

- A stereo pair of 460-line day driving cameras.
- An image-intensified camera-pair for nighttime driving.
- A day targeting camera equipped with a 14-to-1 zoom lens.
- An image-intensified night targeting camera with a 10-to-1 zoom lens.
- An *IRIS-T* FLIR (forward-looking infrared).
- Either an *LTM-86* laser ranger/designator, or an *ESL-100* eye-safe laser ranger.

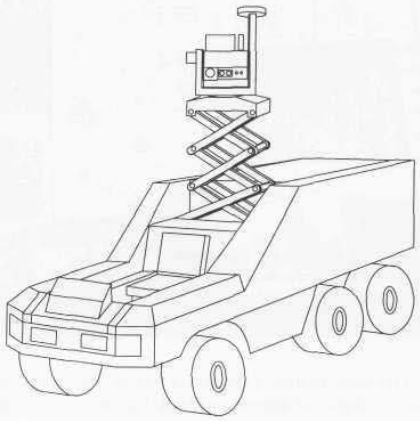

Figure 1-22. The STV incorporates a scaled-down version of the scissors lift developed for the TOV to raise the *Surveillance Module* 15 feet above ground level (courtesy Robotic Systems Technology).

The STV *Communications System* allows the vehicle to be controlled from the man-portable *Operator Control Unit* (Figure 1-23) using either a deployed fiber-optic tether or a back-up RF link (RST, 1993). The 10-kilometer inside-wound fiber-optic spool is packaged in a 3.5 cubic foot cargo-box area behind the engine compartment, with a hinged lid for easy access (Myers, 1992). A low-tension payout scheme feeds the 2.5-millimeter cable out the back as the vehicle moves forward. The RF back-up communications system consists of (RST, 1993):

- A 9600-baud full-duplex (dual-frequency) Repco *SLQ-96 Radio Modem* for command and status data.
- A Repco *Utility Data System (UDS)* FM transmitter for audio to the vehicle.
- A Dell-Star Technologies *900-Series* video transmitter for video and audio from the vehicle to the *Operator Control Unit*.

The maximum effective operating range under level-terrain conditions in the RF mode is approximately 2 kilometers.

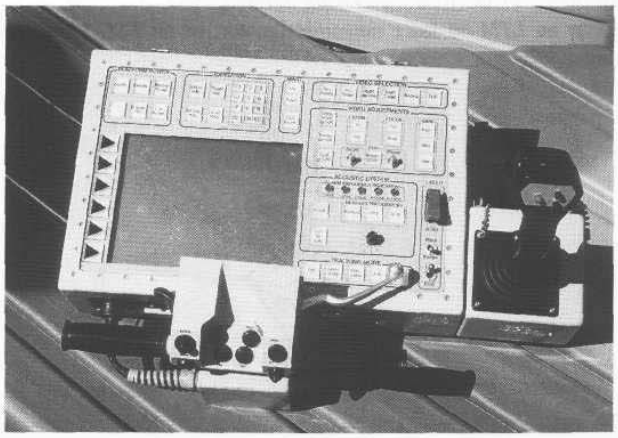

Figure 1-23. The *STV Operator Control Unit* uses a motorcycle-type steering device for vehicle mobility control, with a two-degree-of-freedom joystick for camera pan-and-tilt (courtesy Robotic Systems Technology).

1.2.10 ROBART III (1992-)

ROBART III (Figure 1-24) is intended to be an advanced demonstration platform for non-lethal response measures incorporating the reflexive teleoperated control concepts developed on *ROBART II*. I began work on this experimental system in my garage in July 1992 but was forced to suspend my efforts in December of that same year following a minor dirt-bike accident that put my right arm in a cast for about six months. That little inconvenience put me so far behind schedule on the preparation of this manuscript that further development of ROBART III was placed on hold for essentially the next two years. Recent government interest in dual-use technology reinvestment in a category known as *Operations Other Than War/Law Enforcement* have prompted renewed interest in completing the initial demonstration platform as soon as this book is finished.

Head-mounted sensors include two Polaroid sonar transducers, a Banner near-infrared proximity sensor, an AM Sensors microwave motion detector, and a video surveillance camera. The output of the CCD camera is broadcast to the operator over an analog RF link and simultaneously fed to an onboard video motion detector that provides azimuthal data allowing the head pan-axis controller

to automatically track a moving target. Azimuthal and elevation information from the motion detector will be similarly fed to the pan-and-tilt controller for the six-barrel pneumatically fired dart gun for purposes of automated weapon positioning (Figure 1-25). Additional Polaroid sensors and near-infrared proximity detectors are strategically located to provide full collision avoidance coverage in support of the advanced teleoperation features desired.

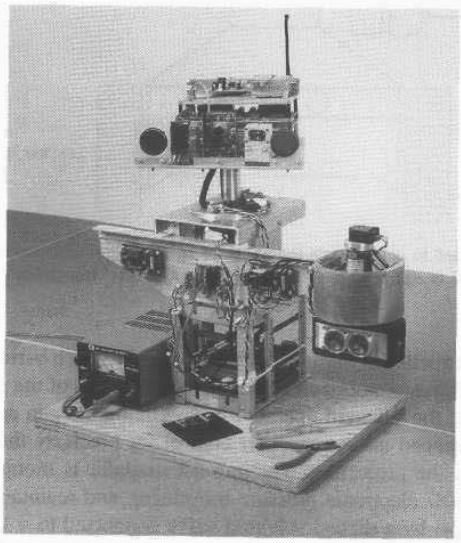

Figure 1-24. Only the upper portion of *ROBART III* was completed before work was temporarily suspended in December 1992.

The non-lethal-response weapon chosen for incorporation into the system consists of a pneumatically powered dart gun capable of firing a variety of $^{3}/_{16}$-inch diameter projectiles. The simulated tranquilizer darts shown in the foreground of Figure 1-26 were developed to demonstrate a potential response application involving remote firing of temporarily incapacitating rounds by law enforcement personnel. The demonstration darts consist of a sharpened 20-gauge spring-steel wires approximately 3 inches long and terminated with $^{3}/_{16}$-inch plastic balls. A rotating-barrel arrangement was incorporated to allow for multiple firings (six) with minimal mechanical complexity. (The spinning-barrel mechanism also imparts a rather sobering psychological message during system initialization.)

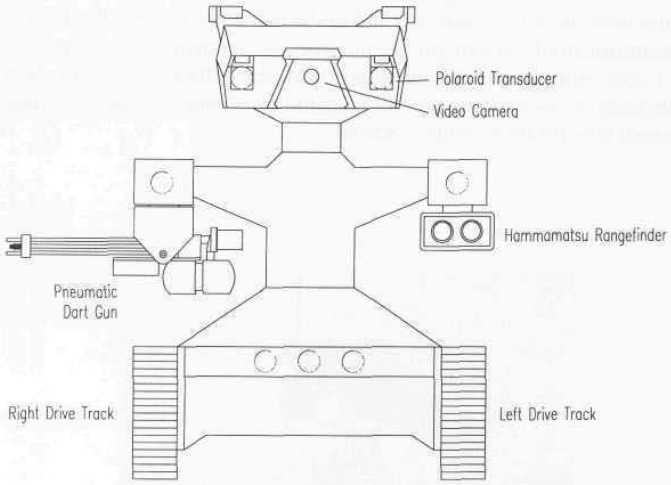

Figure 1-25. Intended to demonstrate the utility of an intelligent teleoperated security response vehicle, *ROBART III* is equipped with a laser-sighted six-barrel tranquilizer dart gun and video tracking.

The darts are expelled at high velocity from their 12-inch barrels by a release of compressed air from a pressurized accumulator at the rear of the gun assembly. To minimize air loss, the solenoid-operated valve linking the gun accumulator to the active barrel is opened under computer control for precisely the amount of time required to expel the projectile. The gun accumulator is monitored by a Micro Switch *242PC150G* electronic pressure transducer, and maintained at a constant pressure of 120 psi by a second solenoid valve connected to a 150-psi air source (see again Figure 1-26). All six darts can thus be fired in rapid succession (approximately 1.5 seconds) under highly repeatable launch conditions to ensure accurate performance. A visible-red laser sight is provided to facilitate manual operation under joystick control using video relayed from the head-mounted camera.

The left and right drive tracks are fashioned from 2.5-inch rubber timing belts turned inside out, driven by a pair of 12-volt electric wheelchair motors identical to those used on ROBART II. System power is supplied by a 80-amphour 12-volt gel-cell battery which provides for several hours of continuous operation between charges. A three-axis Precision Navigation *TCM Electronic Compass Module* (see Chapter 12) provides magnetic heading, temperature, and vehicle attitude (pitch and roll) information to the remote operator. Full-duplex data communication with the PC-based host control station is accomplished via a 9600-baud Telesystems spread-spectrum RF link.

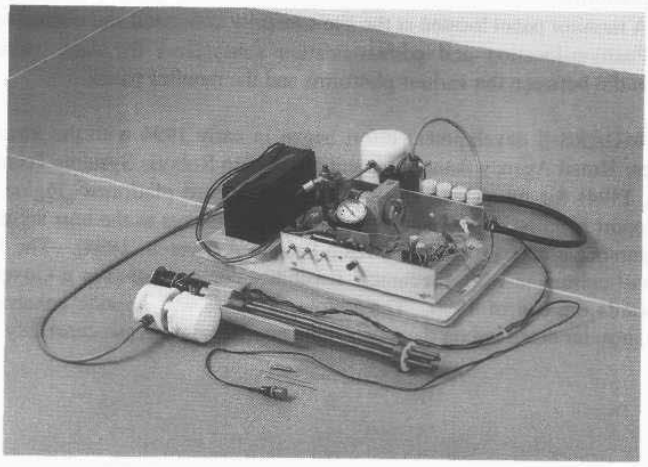

Figure 1-26. The gun accumulator is recharged after each firing from a 150-psi air tank supplied by a 12-volt Campbell Hausfeld automobile air compressor.

1.2.11 MDARS Exterior (1994-)

The *MDARS Exterior* program extends the robotic security and inventory control concepts of *MDARS Interior* into the realm of semi-structured (i.e., improved roads, defined fence lines, and standardized storage layouts) outdoor environments such as storage yards, dock facilities, and airfields. Intruder detection, assessment, and response, product inventories for theft prevention purposes, and lock/barrier checks are some of the physical security and inventory tasks currently performed by government personnel that will be replicated by the exterior robots. Inventory control will consist of verifying the contents of closed structures (i.e., warehouses, bunkers, igloos) without the need for opening. As is the case for the *Interior* program, the user's desire for minimum human involvement dictates that the exterior system operate in a supervised autonomous mode.

To perform the functions described above, it is envisioned that a basic exterior system will consist of the following:

- Two to eight exterior platforms patrolling the same or different areas on a site.

- RF-transponder tag-interrogation equipment on each of the remote platforms.
- A monitor panel located at the site's security command and control station.
- Position-location and communication subsystems for data, voice, and audio between the various platforms and the monitor panel.

The MDARS-E development effort began in early 1994 with the award of a three-year Broad Agency Announcement contract to Robotic Systems Technology (Myers, 1994) for the development of two brassboard platforms (Figure 1-27), with support from NCCOSC in the form of enhancements to the host architecture to accommodate exterior control (Heath-Pastore & Everett, 1994). The Phase-I effort will culminate with a technical feasibility demonstration at a Government site towards the end of 1996. The follow-up phase will provide enhancements such as intruder detection on the move and a non-lethal response capability.

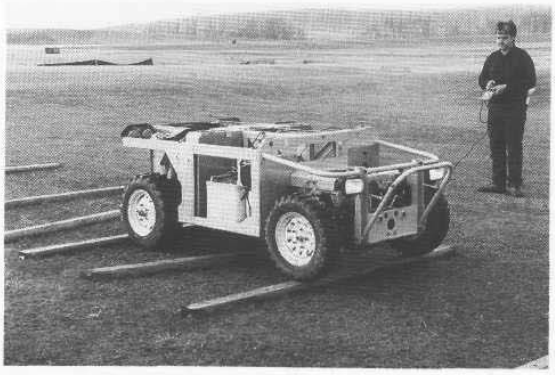

Figure 1-27. The diesel-powered hydrostatic-drive prototype *MDARS Exterior* vehicle being demonstrated under pendant control in January 1995 (courtesy Robotic Systems Technology).

The MDARS Exterior platform currently weighs approximately 1700 pounds and measures 84 inches long by 35 inches high by 50 inches wide, with an 8-inch ground clearance. The four-wheel hydrostatic-drive configuration is powered by an 18-horsepower three-cylinder diesel engine with a 24-volt alternator and integral power steering pump. An Ackerman-steered design was chosen over a skid-steer arrangement for improved dead-reckoning capability. The water-cooled Kubota engine is directly coupled to a 50-cc/rev Rexroth hydrostatic pump that

drives four White Industries rotary hydraulic wheel actuators with integral 200-line phase-quadrature encoders. The Rotac hydraulic steering actuator is independently supplied by the integrated power steering pump. The vehicle was carefully designed with an extremely low center of gravity (14.5 inches above ground level) for maximum stability on uneven terrain.

The MDARS-E vehicle is required to operate over unimproved roads and fairly rough terrain at speeds up to 9 miles per hour, automatically avoiding obstacles greater than 6 inches, breaches wider than 8 inches, and grades steeper than 10 percent. The collision avoidance strategy therefore incorporates a two-tier layered approach, wherein long-range (i.e., 0-100 feet) low-resolution sensors provide broad first-alert *obstacle-detection* coverage, and shorter-range (i.e., 0-30 feet typical) higher-resolution sensors are invoked for more precise *obstacle avoidance* maneuvering. Candidate systems currently being investigated include:

- Stereo vision (Burt, et al., 1992; 1993).
- Laser ranging (see Chapters 5 and 6).
- Millimeter-wave radar (see Chapter 6).
- Ultrasonic ranging (Hammond, 1994).

1.3 References

Aviles, W.A., Everett, H.R., Hughes, T.W., Koyamatsu, A.H., Laird, R.T., Martin, S.W., McArthur, S.P., Umeda, A.Y., "Issues in Mobile Robotics: The Unmanned Ground Vehicle Program TeleOperated Vehicle (TOV)," SPIE Vol. 1388, Mobile Robots V, Boston, MA, pp. 587-597, 8-9 November, 1990.

Burt, P.J., Anadan, P., Hanna, K., van der Wal, G., "A Front End Vision Processor for Unmanned Vehicles," Advanced Image Processing Group, David Sarnoff Research Center, Princeton, NJ, April, 1992.

Burt, P.J., Anadan, P., Hanna, K., van der Wal, G., Bassman, R., "A Front End Vision Processor for Vehicle Navigation," International Conference on Intelligent Systems, February, 1993.

Catling, I., *Advanced Technology for Road Transport: IVHS and ATT*, Artech House, Boston, MA, 1994.

DeCorte, C., "Robots train for Security Surveillance," *Access Control*, pp. 37-38, June, 1994.

Everett, H.R., "A Computer Controlled Sentry Robot," *Robotics Age*, March/April, 1982a.

Everett, H.R., "A Microprocessor Controlled Autonomous Sentry Robot", Masters Thesis, Naval Postgraduate School, Monterey, CA, October 1982b.

Everett, H.R., Gilbreath, G.A., Tran, T., Nieusma, J.M., "Modeling the Environment of a Mobile Security Robot," Technical Document 1835, Naval Command Control and Ocean Surveillance Center, San Diego, CA, June, 1990.

Everett, H.R., Gilbreath, G.A., Heath, T.A., Laird, R.T., "Coordinated Control of Multiple Security Robots," SPIE Vol. 2058, Mobile Robots VIII, Cambridge, MA, September, 1993.

Everett, H.R., Gage, D.W., Gilbreath, G.A., Laird, R.T., Smurlo, R.P., "Real-World Issues in Warehouse Navigation," SPIE Vol. 2352, Mobile Robots IX, Boston, MA, November, 1994.

Gage, D.W., Everett, H.R., Laird, R.T., Heath-Pastore, T.A., "Navigating Multiple Robots in Semi-Structured Environments," ANS 6th Topical Meeting on Robotics and Remote Systems, American Nuclear Society, Monterey, CA, February, 1995.

Gilbreath, G.A., Everett, H.R., "Path Planning and Collision Avoidance for an Indoor Security Robot," SPIE Mobile Robots III, Cambridge, MA, pp. 19-27, November, 1988.

Hammond, W., "Vehicular Use of Ultrasonic Systems," Technical Report, Cybermotion, Inc., Salem, VA, May, 1994.

Heath-Pastore, T.A., Everett, H.R., "Coordinated Control of Interior and Exterior Autonomous Platforms," ISRAM '94, Fifth International Symposium on Robotics and Manufacturing, Maui, HI, August, 1994.

Holland, J.M., "An Army of Robots Roams the Night," International Robot and Vision Automation Show and Conference, Detroit, MI, pp. 17.1-17.12, April, 1993.

Laird, R.T., Everett, H.R., "Reflexive Teleoperated Control," Association for Unmanned Vehicle Systems, Dayton, OH, July, 1990.

Laird, R.T., Everett, H.R., Gilbreath, G.A.., "A Host Architecture for Multiple Robot Control," ANS Fifth Topical Meeting on Robotics and Remote Handling, Knoxville, TN, April, 1993.

Martin, S.W., Hutchinson, R.C., "Low-Cost Design Alternatives for Head-Mounted Displays", Proceedings, SPIE 1083, Three Dimensional Visualization and Display Technologies, 1989.

Metz, C.D., Everett, H.R., Myers, S., "Recent Developments in Tactical Unmanned Ground Vehicles," Association for Unmanned Vehicle Systems, Huntsville, AL, June, 1992.

Myers, S.D., "Update on the Surrogate Teleoperated Vehicle (STV)," Association for Unmanned Vehicle Systems, Hunstville, AL, 1992

Myers, S.D., "Design of an Autonomous Exterior Security Robot," NASA Conference Publication 3251, Vol. 1, Conference on Intelligent Robotics in Field, Factory, Service, and Space, Houston, TX, pp. 82-87, March, 1994.

RST, "Surrogate Teleoperated Vehicle (STV) Technical Manual," Robotic Systems Technology, Westminster, MD, Contract No. N66001-91-C-60007, CDRL Item B001, Final Issue, 13 September, 1993.

Smurlo, R.P, Laird, R.T., "A Modular Robotic Architecture," SPIE Vol. 1388, Mobile Robots V, Boston, MA, 8-9 November, 1990.

Smurlo, R.P., Everett, H.R., "Intelligent Sensor Fusion for a Mobile Security Robot," *Sensors*, pp. 18-28, June, 1993.

2
Dead Reckoning

Dead reckoning (derived from "deduced reckoning" of sailing days) is a simple mathematical procedure for determining the present location of a vessel by advancing some previous position through known course and velocity information over a given length of time (Dunlap & Shufeldt, 1972). The concept was mechanically applied to automobile navigation as early as 1910, when the *Jones Live Map* was advertised as a means of replacing paper maps and eliminating the stress associated with route finding (Catling, 1994). This rather primitive but pioneering system counted wheel rotations to derive longitudinal displacement and employed a frictionally driven steering wheel encoder for calculating heading, and was thus subject to cumulative errors that precluded its ultimate success. The vast majority of land-based mobile robotic systems in use today rely on very similar dead-reckoning schemes to form the backbone of their navigational strategy, but like their nautical counterparts, periodically null out accumulated errors with recurring "fixes" from assorted navigational aids.

The most simplistic implementation of *dead reckoning* is sometimes termed *odometry*, the terminology implying vehicle displacement along the path of travel is directly derived from some onboard "odometer" as in the case of the *Jones Live Map*. A common means of *odometry* instrumentation involves optical encoders directly coupled to the motor armatures or wheel axles. In exterior applications, magnetic proximity sensors are sometimes used to sense a small permanent magnet (or magnets) attached to the vehicle driveshaft, as is typically done in the automotive industry to supply velocity feedback to cruise control equipment. Alternatively, inductive proximity sensors have been employed to detect cogs on a wheel or individual sections of a steel track when no rotational shafts are conveniently exposed, which is often the case when retrofitting conventional off-road equipment.

Heading information can be: 1) indirectly derived from an onboard steering angle sensor, 2) supplied by a magnetic compass or gyro, or 3) calculated from differential odometry as will be discussed below. Incremental displacement along the path is broken up into X and Y components, either as a function of elapsed

time or distance traveled. For straight-line motion (i.e., no turns), periodic updates to vehicle-position coordinates are given by:

$$x_{n+1} = x_n + D\sin\theta$$
$$y_{n+1} = y_n + D\cos\theta$$

where:

D = vehicle displacement along path
θ = vehicle heading.

Klarer (1988) presents an excellent and detailed description of the appropriate algorithms for various types of steering configurations, some of which will be discussed in further detail later in this chapter.

2.1 Odometry Sensors

Since most (but not all!) mobile robots rely on some variation of wheeled locomotion, a basic understanding of sensors that accurately quantify angular position and velocity is an important prerequisite to further discussions of odometry. There are a number of different types of rotational displacement and velocity sensors in use today:

- Brush Encoders.
- Potentiometers.
- Synchros.
- Resolvers.
- Optical Encoders.
- Magnetic Encoders.
- Inductive Encoders.
- Capacitive Encoders.

A multitude of issues must be considered in choosing the appropriate device for a particular application. Aviolio (1993) points out that over 17 million variations of rotary encoders are offered by one company alone. We shall examine in more detail the three most common types as applied to odometry sensing: 1) *potentiometers*, 2) *resolvers*, and 3) *optical encoders*.

2.1.1 Potentiometers

Potentiometers, or *pots* for short, are often used as low-cost rotational displacement sensors in low-speed medium-accuracy applications not involving continuous rotation. (For example, both ROBART I and ROBART II used precision potentiometers to sense head pan position.) The principle of operation is that of a variable-resistance voltage divider (Figure 2-1), where the center tap is a mechanically coupled wiper that moves across the resistance element in conjunction with shaft rotation. A variety of relationships (tapers) defining

resistance as a function of wiper displacement are employed in the fabrication of potentiometers (i.e., audio, logarithmic, sinusoidal, linear), with linear taper being the most common scheme in position sensing applications.

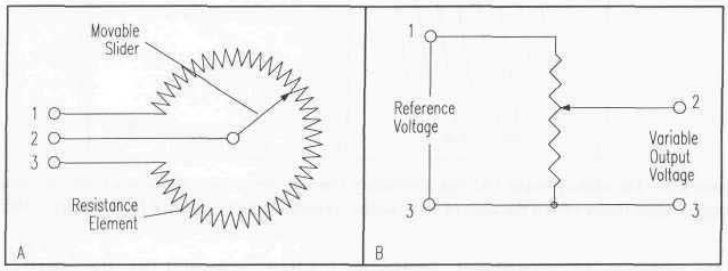

Figure 2-1. For a linear-taper pot, the output voltage V_o is directly related to the ratio of actual to full scale displacement.

The principle advantages of potentiometric sensors are very low cost and ease of interface. A regulated DC voltage is applied across the full resistance R as shown. Output voltage is given by the equation:

$$V_o = V_{ref} \frac{r}{R}$$

where:

V_o = output voltage from wiper
V_{ref} = reference voltage across pot
r = wiper-to-ground resistance
R = total potentiometer resistance.

For linear-taper devices, the quotient r/R is precisely equal to the ratio of actual to full-scale wiper displacement, assuming negligible loading effects. Since output voltage is also a linear function of the reference voltage V_{ref}, care must be taken to use a well-regulated noise-free supply.

Wire-wound pots can exhibit a piecewise quantification in performance as illustrated in Figure 2-2, since resistance is not continuously varied but instead incrementally stepped as a result of the coil design (Fraden, 1993). In addition, the wiper will temporarily "short" together adjacent windings in passing, changing the effective total resistance. The best precision potentiometers therefore employ a continuous resistive film fabricated from carbon, conductive plastic, or a ceramic-metal mix known as *cermet*. While a good wire-wound pot can provide an average resolution of about 0.1 percent of full scale, the high-quality resistive-film devices are generally limited only by manufacturing tolerances governing the uniformity of the resistance element (Fraden, 1993).

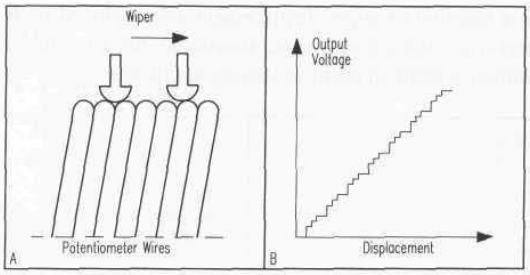

Figure 2-2. The sliding wiper (A) can alternately contact one or two wires at a time, introducing an output uncertainty (B) in the case of wire-wound potentiometers (adapted from Fraden, 1993).

In addition to significant frictional loading imparted to the shaft, the fundamental disadvantage of potentiometers is their relatively poor reliability due to dirt build-up and inevitable wiper wear, resulting in noisy and erratic operation. Other errors can be introduced by slack and/or elasticity in the belt drive if not directly coupled to the shaft, and electrical noise introduced into the analog output line. For these reasons, the use of potentiometers as rotation sensing devices has fallen off in recent years in favor of the more versatile incremental optical encoders, to be discussed in Section 2.1.3.

2.1.2 Synchros and Resolvers

Synchros are rotating electromechanical devices used to transmit angular information electrically from one place to another with great precision (Schwartz & Grafstein, 1971). In essence, the *synchro* forms a variable-coupling transformer consisting of an AC-excited rotor winding (primary) and two or more stator windings (secondaries) symmetrically oriented around the rotor. The effective magnetic coupling between the rotor winding and the surrounding stator windings varies as a function of rotor orientation. Maximum coupling occurs when the fields are parallel, while minimal coupling results when the rotor field is orthogonally aligned with respect to a particular stator winding. As a consequence, the stator outputs form a set of AC signals whose respective magnitudes uniquely define the rotor angle at any given point in time. A wide variety of *synchro* types exist:

- Transmitters.
- Differentials.
- Receivers.
- Control Transformers.
- Resolvers.
- Differential Resolvers.
- Linear Transformers.
- Transolvers.

Deirmengian (1990a) provides a comprehensive treatment of the theory of operation for the components listed above, followed by a detailed examination of the various design parameters and error sources that must be taken into account (1990b).

The most widely known *synchro* configuration is probably the three-phase *transmitter/receiver* pair commonly used for remote shaft-angle indication. The slave *synchro receiver* is electrically identical to the master *transmitter* and connected so that the stator windings for both devices are in parallel as shown in Figure 2-3. The rotor windings on both the transmitter and the remote-indicating receiver are excited by an AC current (400 Hz to several KHz) typically supplied through slip rings. When the receiver and transmitter rotors are in identical alignment with their respective stator windings, the individual stator outputs will be equal for the two devices, and consequently there will be no current flow.

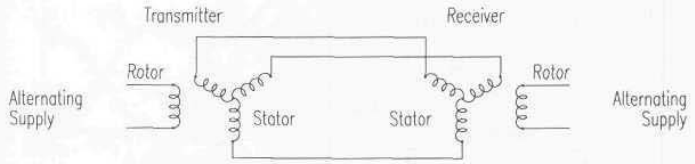

Figure 2-3. Schematic diagram of a typical remote-indicating synchro configuration (adapted from Schwartz & Graftstein, 1971).

If the transmitter rotor shaft is turned by some external force, the equilibrium conditions are upset, and the resulting voltage differences generate current flows in both sets of stator windings. These current flows induce an identical torque in both rotors, but since the transmitter rotor is constrained, the torque on the receiver rotor acts to restore alignment and thus equilibrium (Diermengian, 1990a). The observed effect is the receiver output shaft will precisely track any rotational displacement seen by the remotely located transmitter input shaft. More than one receiver can be driven by a common transmitter. For example, Navy ships are equipped with a number of remote heading indicators (directional gyro repeaters) located in the pilot house, on the port and starboard bridge wings, and up on the signal bridge, while the gyro itself is mounted deep inside the vessel to minimize effects of ships motion (i.e., pitch and roll).

The *resolver* is a special configuration of the *synchro* that develops voltages proportional to the sine and cosine of rotor angle, and thus is often used to break down a vector quantity into its associated components. A typical example is seen in the aircraft industry where resolvers are used to perform coordinate transforms between aircraft- and ground-based reference frames. Only two stator coils are involved, oriented 90 degrees apart as shown in Figure 2-4 (Tiwari, 1993).

The individual stator outputs as a function of input excitation and rotor position θ are given by the following equations (ILC, 1982):

$$V_x = K_x \sin\theta \sin(\omega t + a_x)$$
$$V_y = K_y \cos\theta \sin(\omega t + a_y)$$

where:

θ = the resolver input shaft angle
$\omega = 2\pi f$, where f is the excitation frequency
K_x and K_y are ideally equal transfer-function constants
a_x and a_y are ideally zero time-phase shifts between rotor and stator.

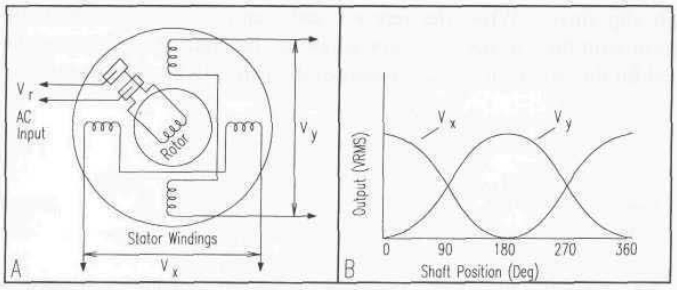

Figure 2-4. The outputs of the two orthogonal stator windings in a *resolver* are proportional to the sine and cosine of the applied rotor excitation (adapted from Tiwari, 1993).

The definitive mathematical relationship inherent in the *resolver* output signals means the transmitter can be used stand-alone (i.e., without a slave receiver) as an input transducer in a digital control system. A *resolver-to-digital converter* (RDC) is employed in place of the receiver to transform the output signals into an appropriate format for computer interface. This conversion is typically done in one of three ways: 1) phase-shift approach, 2) amplitude-ratio approach, or 3) multiplex approach. Grandner and Lanton (1986) present an excellent overview and comparison of these three techniques, of which the amplitude-ratio approach seems to be gaining the most popularity. The *ISN4* hybrid phase tracking RDC from Analog Devices provides a special velocity output in addition to absolute position information (Nickson, 1985).

In summary, resolvers offer a very rugged and reliable means for quantifying absolute angular position that is accurate, moderately cheap, and fairly small in terms of physical size. The advent of custom large-scale integrated (LSI) circuits has reduced the cost of associated electronics, making resolvers competitive with other alternatives (Grandner & Lanton, 1986). Brushless versions employ a special cylindrical transformer instead of slip rings to couple AC excitation to the rotor as shown in Figure 2-5 (Nickson, 1985). These configurations have essentially no wear and therefore zero maintenance, but at the expense of additional power consumption and increased length.

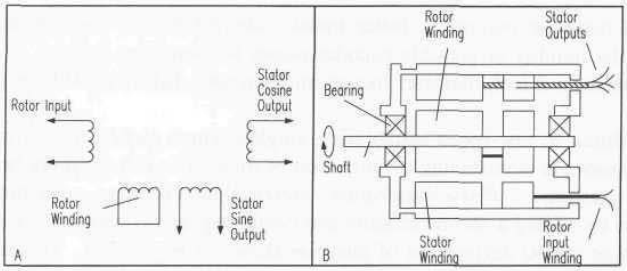

Figure 2-5. Brushless resolvers employ a rotating transformer instead of slip rings to couple excitation energy to the rotor and essentially require no maintenance (adapted from Nickson, 1985).

2.1.3 Optical Encoders

The first optical encoders were developed in the mid-1940s by the Baldwin Piano Company for use as "tone wheels" that allowed electric organs to mimic other musical instruments (Agent, 1991). Today's contemporary devices basically embody a miniaturized version of the *opposed-mode proximity sensor* (see Chapter 3). A focused beam of light aimed at a matched photodetector is periodically interrupted by a coded opaque/transparent pattern on a rotating intermediate disk attached to the shaft of interest. The rotating disk may take the form of chrome on glass, etched metal, or photoplast such as Mylar (Henkel, 1987). Relative to the more complex alternating-current resolvers, the straightforward encoding scheme and inherently digital output of the optical encoder results in a low-cost reliable package with good noise immunity.

There are two basic types of optical encoders: *incremental* and *absolute*. The *incremental* version measures rotational velocity and can infer relative position, while *absolute* models directly measure angular position and infer velocity. If non-volatile position information is not a consideration, *incremental encoders* generally are easier to interface and provide equivalent resolution at a much lower cost than *absolute optical encoders.*

Incremental Optical Encoders

The simplest type of *incremental encoder* is a single-channel *tachometer encoder,* which is basically an instrumented mechanical light chopper that produces a certain number of sine or square wave pulses for each shaft revolution. The greater the number of pulses, the higher the resolution (and subsequently the cost) of the unit. These relatively inexpensive devices are well suited as velocity feedback sensors in medium- to high-speed control systems, but run into noise and stability problems at extremely slow velocities due to quantization errors (Nickson, 1985). The tradeoff here is resolution versus update rate: improved

transient response requires a faster update rate, which for a given line count reduces the number of possible encoder pulses per sampling interval. A typical limitation for a 2-inch diameter incremental encoder disk is 2540 lines (Henkel, 1987).

In addition to low-speed instabilities, single-channel *tachometer encoders* are also incapable of determining the direction of rotation and thus cannot be used as position sensors. *Phase-quadrature incremental encoders* overcome these problems by adding a second channel and displacing the detectors so the resulting pulse trains are 90 degrees out of phase as shown in Figure 2-6. This technique allows the decoding electronics to determine which channel is leading the other and hence ascertain the direction of rotation, with the added benefit of increased resolution. Holle (1990) provides an in-depth discussion of output options (single-ended TTL or differential drivers) and various design issues (i.e., resolution, bandwidth, phasing, filtering) for consideration when interfacing phase-quadrature incremental encoders to digital control systems.

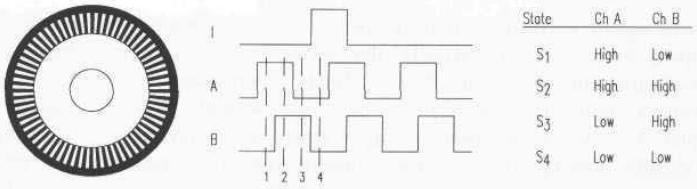

Figure 2-6. The observed phase relationship between Channel A and B pulse trains can be used to determine the direction of rotation with a phase-quadrature encoder, while unique output states S_1 - S_4 allow for up to a four-fold increase in resolution. The single slot in the outer track generates one index (I) pulse per disk rotation.

The incremental nature of the phase-quadrature output signals dictates that any resolution of angular position can only be relative to some specific reference, as opposed to absolute. Establishing such a reference can be accomplished in a number of ways. For applications involving continuous 360-degree rotation, most encoders incorporate as a third channel a special *index output* that goes high once for each complete revolution of the shaft (see Figure 2-6 above). Intermediate shaft positions are then specified by the number of encoder *up counts* or *down counts* from this known index position. One disadvantage of this approach is all relative position information is lost in the event of a power interruption.

In the case of limited rotation, such as the back-and-forth motion of a pan or tilt axis, electrical limit switches and/or mechanical stops can be used to establish a *home reference* position. To improve repeatability this homing action is sometimes broken up into two steps. The axis is rotated at reduced speed in the appropriate direction until the stop mechanism is encountered, whereupon rotation is reversed for a short predefined interval. The shaft is then rotated slowly back into the stop at a specified low velocity from this designated start point, thus eliminating any variations in inertial loading that could influence the final homing

position. This two-step approach can usually be observed in the power-on initialization of stepper-motor positioners for dot-matrix printer heads.

Alternatively, the absolute indexing function can be based on some external referencing action that is decoupled from the immediate servo-control loop. A good illustration of this situation involves an incremental encoder used to keep track of platform steering angle. For example, when the Cybermotion *K2A Navmaster* robot is first powered up, the absolute steering angle is unknown and must be initialized through a "referencing" action with the docking beacon, a nearby wall, or some other identifiable set of landmarks of known orientation (see Chapters 15 and 16). The up/down count output from the decoder electronics is then used to modify the vehicle heading register in a relative fashion.

A growing number of very inexpensive off-the-shelf components have contributed to making the phase-quadrature incremental encoder the rotational sensor of choice within the robotics research and development community. Figure 2-7 shows an incremental optical encoder and PID motor-controller chip made by Hewlett Packard, along with a National Semiconductor H-bridge amplifier that collectively form the basis of a complete digital control system for a total package price of well under $100. Several manufacturers now offer small DC gearmotors with incremental encoders already attached to the armature shafts. Within the US automated guided vehicle (AGV) industry, however, resolvers are still generally preferred over optical encoders for their perceived superiority under harsh operating conditions, but the European AGV community seems to clearly favor the encoder (Manolis, 1993).

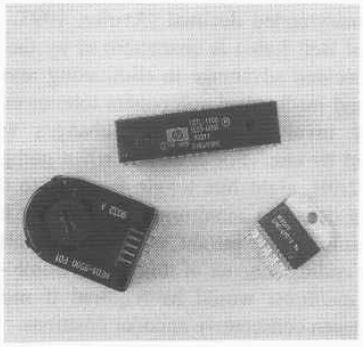

Figure 2-7. Shown here are the major components for a complete digital control system: (from left to right) a Hewlett Packard *HEDS-5500* incremental optical encoder, a Hewlett Packard *HCTL-1100* PID controller chip, and a National Semiconductor *LMD18200* H-bridge power amplifier (courtesy Naval Command Control and Ocean Surveillance Center).

Absolute Optical Encoders

Absolute encoders are typically used for slower rotational applications that require positional information when potential loss of reference from power interruption cannot be tolerated. Discrete detector elements in a photovoltaic array are individually aligned in break-beam fashion with concentric encoder tracks as shown in Figure 2-8, creating in effect a non-contact implementation of the earlier commutating brush encoder. The assignment of a dedicated track for each bit of resolution results in larger size disks (relative to incremental designs), with a corresponding decrease in shock and vibration tolerance. A general rule of thumb is that each additional encoder track doubles the resolution but quadruples the cost (Agent, 1991).

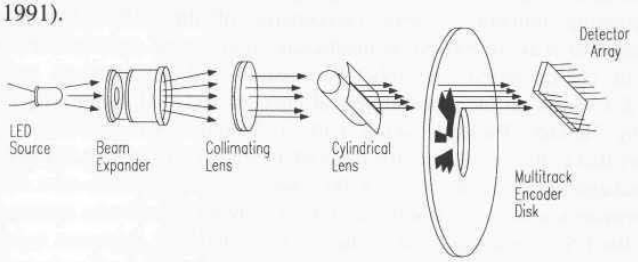

Figure 2-8. A line source of light passing through a coded pattern of opaque and transparent segments on the rotating encoder disk results in a parallel output that uniquely specifies the absolute angular position of the shaft (adapted from Agent, 1991).

Instead of the serial bit streams of incremental designs, absolute optical encoders provide a parallel word output with a unique code pattern for each quantized shaft position. The most common coding schemes are Gray code, natural binary, and binary-coded decimal (Avolio, 1993). The Gray code (for inventor Frank Gray of Bell Labs) is characterized by the fact that only one bit changes at a time, a decided advantage in eliminating asynchronous ambiguities caused by electronic and mechanical component tolerances. Binary code, on the other hand, routinely involves multiple-bit changes when incrementing or decrementing the count by one. For example, when going from position 255 to position 0 in Figure 2-9B, eight bits toggle from 1s to 0s. Since there is no guarantee all threshold detectors monitoring the detector elements tracking each bit will toggle at the same precise instant, considerable ambiguity can exist during state transition with a coding scheme of this form. Some type of handshake line signaling *valid data available* would be required if more than one bit were allowed to change between consecutive encoder positions.

Absolute encoders are best suited for slow and/or infrequent rotations such as steering angle encoding, as opposed to measuring high-speed continuous (i.e., drivewheel) rotations as would be required for calculating displacement along the path of travel. Although not quite as robust as resolvers for high-temperature, high-shock applications, operation at temperatures in excess of 125 degrees C is

possible, and medium-resolution (1000 counts per revolution) metal or Mylar disk designs can compete favorably with resolvers in terms of shock resistance (Manolis, 1993).

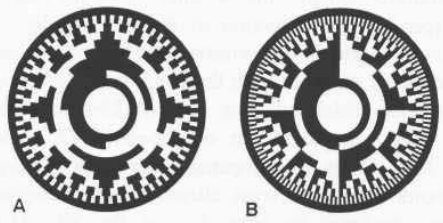

Figure 2-9. Rotating an 8-bit absolute Gray code disk (A) counterclockwise by one position increment will cause only one bit to change, whereas the same rotation of a binary-coded disk (B) will cause all bits to change in the particular case (255 to 0) illustrated by the reference line at 12 o'clock.

More complex interface issues due to the large number of leads associated with the parallel nature of the output pose a potential disadvantage. A 13-bit absolute encoder using complimentary output signals for noise immunity would require a 28-conductor cable (13 signal pairs plus power and ground), versus only six for a resolver or incremental encoder (Avolio, 1993).

2.2 Doppler and Inertial Navigation

The rotational displacement sensors discussed above derive navigational parameters directly from wheel rotation, and are thus subject to problems arising from slippage, tread wear, and/or improper tire inflation. In certain applications, Doppler and inertial navigation techniques are sometimes employed to reduce the effects of such error sources.

2.2.1 Doppler Navigation

Doppler navigation systems are routinely employed in maritime and aeronautical applications to yield velocity measurements with respect to the earth itself, thus eliminating dead-reckoning errors introduced by unknown ocean or air currents. The principle of operation is based on the Doppler shift in frequency observed when radiated energy reflects off a surface that is moving with respect to the emitter, as will be discussed in detail in Chapter 8. Maritime systems employ acoustical energy reflected from the ocean floor, while airborne systems sense microwave RF energy bounced off the surface of the earth. Both configurations

typically involve an array of four transducers spaced 90 degrees apart in azimuth and inclined downward at a common angle with respect to the horizontal plane (Dunlap & Shufeldt, 1972).

Due to cost constraints and the reduced likelihood of transverse drift, most robotic implementations employ but a single forward-looking transducer to measure ground speed in the direction of travel. Similar configurations are sometimes used in the agricultural industry, where tire slippage in soft freshly plowed dirt can seriously interfere with the need to release seed or fertilizer at a rate commensurate with vehicle advance. The M113-based Ground Surveillance Robot (Harmon, 1986) employed an off-the-shelf RF system of this type manufactured by John Deere to compensate for track slippage (Figure 2-10). Milner (1990) reports a very low-cost ultrasonic unit designed to be worn by runners and skiers (marketed by Nike, Inc. as the *Nike Monitor*) that could measure a mile to within 10 feet.

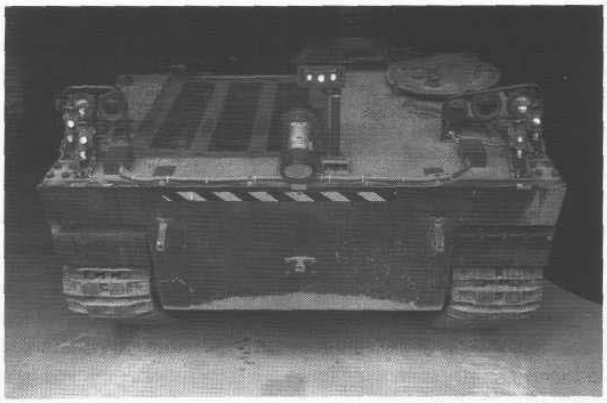

Figure 2-10. A commercially available John Deere agricultural ground-speed sensor was employed on the Ground Surveillance Robot to improve dead-reckoning accuracy (courtesy Naval Command Control and Ocean Surveillance Center).

The microwave (or ultrasonic) sensor is aimed downward at a prescribed angle (typically 45 degrees) to sense ground movement as shown in Figure 2-11. Actual ground speed V_A is derived from the measured velocity V_D in accordance with the following equation (Schultz, 1993):

$$V_A = \frac{V_D}{\cos\alpha} = \frac{c\,F_D}{2\,F_o\cos\alpha}$$

where:

V_A = actual ground velocity along path
V_D = measured Doppler velocity
α = angle of declination
c = speed of light
F_D = observed Doppler shift frequency
F_O = transmitted frequency.

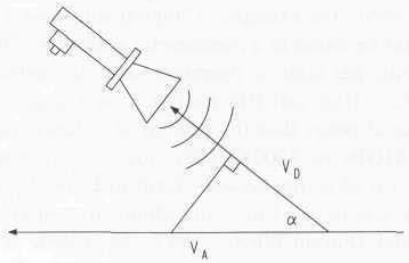

Figure 2-11. A Doppler ground speed sensor inclined at an angle α as shown measures the velocity component V_D of true ground speed V_A (adapted from Schultz, 1993).

Errors in determining true ground speed arise due to side-lobe interference, vertical velocity components introduced by vehicle reaction to road surface anomalies, and uncertainties in the actual angle of incidence due to the finite width of the beam. Since the Doppler frequency is proportional to the cosine of the angle, the far part of the beam returns a higher frequency than the near part, with a continuous distribution of frequencies in between (Milner, 1990). Signal processing techniques (i.e., square-root-of-frequency filters, centroid extractors, phase-lock loops) are necessary to extract a representative frequency from the spectrum.

Byrne, et al. (1992) point out another interesting scenario for potentially erroneous operation, involving a stationary vehicle parked over a stream of water. The Doppler ground-speed sensor in this case would misinterpret the relative motion between the stopped vehicle and the running water as vehicle travel.

2.2.2 Inertial Navigation

An alternative approach to augmenting the dead-reckoning solution beyond simple odometry is *inertial navigation*, initially developed for deployment on aircraft. The technology was quickly adapted for use on missiles and in outer space, and found its way to maritime usage when the nuclear submarines *Nautilus* and *Skate* were suitably equipped in support of their transpolar voyages in 1958 (Dunlap & Shufeldt, 1972). The principle of operation involves continuous sensing of minute accelerations in each of the three directional axes, and

integrating over time to derive velocity and position. A gyroscopically stabilized sensor platform is used to maintain consistent orientation of the three accelerometers throughout this process.

Although fairly simple in basic concept, the specifics of implementation are rather demanding from the standpoint of minimizing the various error sources that adversely affect the stability of the gyros used to ensure correct attitude. The resulting high manufacturing and maintenance costs have effectively precluded any practical application of this technology in the automated guided vehicle industry (Turpin, 1986). For example, a "high-quality" *inertial navigation system* (INS) such as would be found in a commercial airliner will have a typical drift of about 1 nautical mile per hour of operation, and cost between $50K and $70K (Byrne, et al., 1992). High-end INS packages used in ground applications have shown performance of better than 0.1 percent of distance traveled but cost in the neighborhood of $100K to $200K, while lower performance versions (i.e., 1 percent of distance traveled) run between $20K to $50K (Dahlin & Krantz, 1988).

Experimental results by the Universite Montpellier in France (Vaganay, et al., 1993), Barsham and Durrant-Whyte (1993), Mononen, et al. (1994), and the University of Michigan (Borenstein, 1994a) indicate the inertial navigation approach is not realistically advantageous for the above reasons. As a consequence, the use of INS hardware in robotic applications has to date been generally limited to scenarios that aren't readily addressable by more practical alternatives. An example of such a situation is presented by Sammarco (1990; 1994), who reports preliminary results in the case of an INS used to control an autonomous vehicle in a mining application. The development of increasingly low-cost fiber-optic gyros and solid-state accelerometers, however, promises to open up new opportunities in the not too distant future.

The various gyro and accelerometer components that make up an *inertial navigation system* will be treated in some detail later in Chapter 13.

2.3 Typical Mobility Configurations

A number of design issues impact the selection of an appropriate drive and steering configuration for a mobile robotic vehicle:

- *Maneuverability* — The ability to translate and/or change direction of motion must be consistent with the constraints of the surrounding environment.
- *Controllability* — The hardware and software necessary to control the mobility scheme must be practical and not overly complex.
- *Traction* — Sufficient traction should be provided to minimize slippage under varying conditions in accordance with anticipated operational scenarios.

- *Climbing ability* — Indoor schemes must allow for traversal of minor discontinuities or gaps in the floor surface; exterior requirements are dictated by the range of terrain features associated with the application.
- *Stability* — The mobility base must provide sufficient stability for the payload with an adequate safety margin under expected conditions of acceleration, tilt, and roll.
- *Efficiency* — Power consumption must be in keeping with available energy reserves and duty cycle.
- *Maintenance* — The system should be easy to maintain with an acceptable mean time between failure, and not prone to excessive tire or component wear.
- *Environmental impact* — The drive and steering functions should not damage the floor or ground surface.
- *Navigational considerations* — Dead-reckoning accuracy should be in keeping with the needs of the application.

This next section will discuss only those sensor considerations in support of the last of these categories.

2.3.1 Differential Steering

A very common indoor propulsion system uses two individually controlled drive wheels on either side of the base, with casters in front and rear for stability. This configuration allows the robot to spin in place about the vertical axis for maneuvering in congested areas. Drivemotor velocities are monitored by optical encoders attached to the armature shafts (Figure 2-12). High-resolution phase-quadrature encoders produce hundreds of counts per turn of the motor armatures, which usually translates to thousands of counts per wheel revolution. Very precise displacement and velocity information is thus available for use in dead reckoning calculations, but the results are influenced by a number of systemic as well as external sources of error that must be taken into account.

Robot displacement D along the path of travel is given by the equation:

$$D = \frac{D_l + D_r}{2}$$

where:

D = displacement of platform
D_l = displacement of left wheel
D_r = displacement of right wheel.

Similarly, the platform velocity V is given by the equation:

$$V = \frac{V_l + V_r}{2}$$

where:

V = velocity of platform
V_l = velocity of left wheel
V_r = velocity of right wheel.

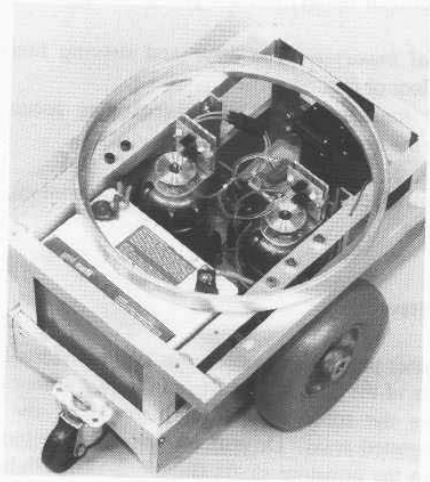

Figure 2-12. Early style incremental optical encoders attached to the left and right drive motor armatures provide differential odometry information for the drive controller on ROBART II.

Referring to Figure 2-13, arc D_l represents a portion of the circumference of a circle of radius $d + b$:

$$C_l = 2\pi(d + b)$$

where:

C_l = circumference of circle traced by left wheel
d = distance between left and right drive wheels
b = inner turn radius.

In addition, the relationship:

$$\frac{D_l}{C_l} = \frac{\theta}{2\pi} \quad \text{yields:} \quad C_l = \frac{2\pi D_l}{\theta}.$$

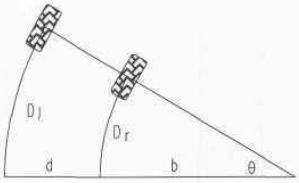

Figure 2-13. Arcs D_l and D_r are traced by the left and right wheels for change in robot heading θ.

Combining the above equations and solving for θ:

$$\theta = \frac{D_l}{d+b}.$$

Similarly, the shorter arc D_r represents a portion of the circumference of a circle of radius b:

$$C_r = 2\pi b$$

where:

C_r = circumference of circle traced by right wheel.

And the relationship: $\frac{D_r}{C_r} = \frac{\theta}{2\pi}$ yields: $C_r = \frac{2\pi D_r}{\theta}$.

Combining equations and solving for b:

$$b = \frac{D_r}{\theta}$$

Substituting this expression for b into the previous expression for θ:

$$\theta = \frac{D_l}{d + \frac{D_r}{\theta}} = \frac{D_l - D_r}{d}.$$

Note this expression for the change in vehicle orientation θ is a function of the displacements of the left and right drive wheels and is completely independent of the path taken. The variable d in the denominator, however, represents a significant source of error, due to uncertainties associated with the effective point of contact of the tires as illustrated in Figure 2-14. The assumption that wheel separation distance is simply the center-to-center distance d as shown is inappropriate. Non-planar irregularities in the floor surface can combine with variations in both tread wear and compliance to shift the effective point of contact in rather unpredictable fashion, with a very detrimental impact on vehicle heading.

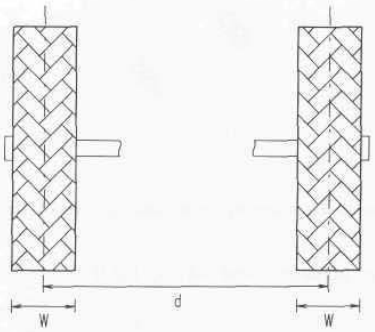

Figure 2-14. Uncertainties in the effective point of contact between tire and floor introduce an ambiguity $2W$ into wheel separation distance d.

Referring now to Figure 2-15, wheel displacement D_l is given by the equation:

$$D_l = \phi R_{el}$$

where:

ϕ = wheel rotation (radians)
R_{el} = effective left wheel radius.

Expressing in terms of encoder counts, this yields:

$$D_l = \frac{2\pi N_l}{C_t} R_{el}$$

where:

N_l = number of counts left encoder
C_t = encoder counts per wheel revolution.

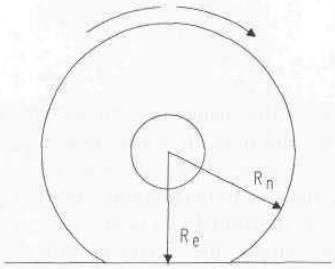

Figure 2-15. Due to tire compliance, effective wheel radius R_e is less than nominal wheel radius R_n.

Similarly, for the right drive wheel:

$$D_r = \frac{2\pi N_r}{C_t} R_{er}$$

where:

N_r = number of counts right shaft encoder
C_t = encoder counts per wheel revolution
R_{er} = effective right wheel radius.

The drive controller will attempt to make the robot travel a straight line by ensuring N_r and N_l are the same. Note, however, that effective wheel radius is a function of the compliance of the tire and the weight of the robot and must be determined empirically. In actuality, R_{el} may not be equal to R_{er}, as was the case when several tires were tested on ROBART II in an attempt to obtain a matched set. For some tires, the compliance (and hence effective radius) was found to vary as a function of wheel rotation ϕ.

Ignoring this situation momentarily for the sake of simplicity, let us next assume a non-compliant wheel of radius R traversing a step discontinuity of height h as shown in Figure 2-16 below. In climbing over the step, the wheel effectively rotates around the point C in the diagram until the axle is directly overhead C at point O' (Borenstein, 1994). The wheel encoder meanwhile measures an effective rotation ϕ corresponding to movement of the axle along path O-O', for a perceived distance D_m. As Borenstein points out, however, the actual horizontal distance traveled is only D_h, creating a linear error of magnitude D_m - D_h. In the case of bump traversal, a similar error will be incurred in rolling off the other side at point C' as the wheel drops an identical distance h in returning to floor level. This displacement differential between left and right drive wheels results in an instantaneous heading change (towards the side traversing the bump) equal to:

$$\Delta\theta = 2\,\frac{D_m - D_h}{d}$$

where:

D_m = measured distance traveled
D_h = actual horizontal distance traveled
d = wheel separation distance as before.

A similar effect is observed when traversing a crack in the floor surface, with the vertical drop h' determined by the relationship of wheel diameter to the width w of the crack.

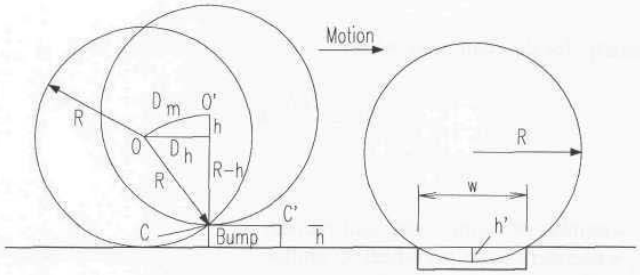

Figure 2-16. Traversal of a small bump creates a differential in the horizontal distance traveled versus the perceived distance measured by the encoder, resulting in a significant angular offset (adapted with changes from Borenstein, 1994a, © IEEE). A similar effect is experienced when rolling over a crack of width *w*.

Bumps and cracks in the floor can cause non-systemic errors that adversely affect dead reckoning performance. Another common error source is the inevitable slippage that occurs between tire and floor surfaces due to grease or oil build-up, fluid spills, excessive acceleration or deceleration, or even actual impact to the vehicle itself. This problem is especially noticeable in an exterior implementation of differential drive known as *skid steering*, routinely implemented in track form on bulldozers and armored vehicles. Such *skid-steer* configurations intentionally rely on track or wheel slippage for normal operation (Figure 2-17) and as a consequence provide rather poor dead-reckoning information. For this reason, *skid steering* is generally employed only in teleoperated as opposed to autonomous robotic applications, where the ability to surmount significant floor discontinuities is more desirable than accurate dead-reckoning information. An example is seen in the track drives popular with remote-controlled robots intended for explosive ordnance disposal.

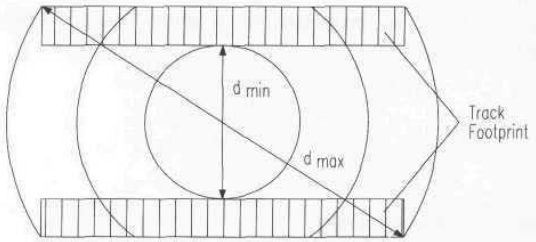

Figure 2-17. The effective point of contact for a skid-steer vehicle is roughly constrained on either side by a rectangular zone of ambiguity corresponding to the track footprint. As is implied by the concentric circles, considerable slippage must occur in order for the vehicle to turn.

2.3.2 Ackerman Steering

Used almost exclusively in the automotive industry, *Ackerman steering* (Jones & Flynn, 1993) is designed to ensure the inside front wheel is rotated to a slightly sharper angle than the outside wheel when turning, thereby eliminating geometrically induced tire slippage. As seen in Figure 2-18, the extended axes for the two front wheels intersect in a common point that lies on the extended axis of the rear axle. The locus of points traced along the ground by the center of each tire is thus a set of concentric arcs about this centerpoint of rotation P_1, and (ignoring for the moment any centrifugal accelerations) all instantaneous velocity vectors will subsequently be tangential to these arcs. Such a steering geometry is said to satisfy the *Ackerman equation* (Byrne, et al., 1992):

$$\cot\theta_i - \cot\theta_o = \frac{d}{l}$$

where:

θ_i = relative steering angle of inner wheel
θ_o = relative steering angle of outer wheel
l = longitudinal wheel separation
d = lateral wheel separation.

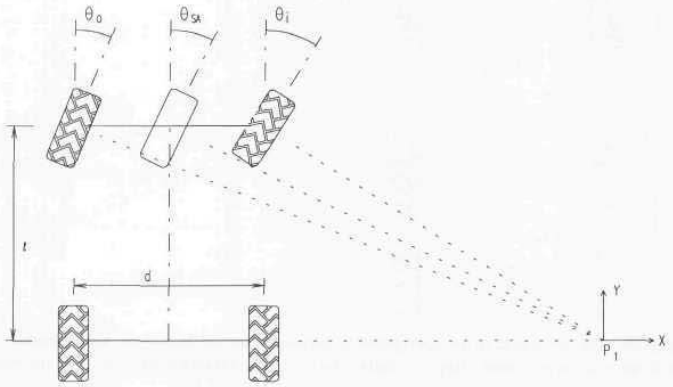

Figure 2-18. In an Ackerman-steered vehicle, the extended axes for all wheels intersect in a common point (adapted from Byrne, et al., 1992).

For sake of convenience, the vehicle steering angle θ_{SA} can be thought of as the angle (relative to vehicle heading) associated with an imaginary center wheel as shown in the figure above. θ_{SA} can be expressed in terms of either the inside or outside steering angles (θ_i or θ_o) as follows (Byrne, et al., 1992):

$$\cot\theta_{SA} = \frac{d}{2l} + \cot\theta_i \quad \text{or alternatively:} \quad \cot\theta_{SA} = \cot\theta_o - \frac{d}{2l}.$$

Ackerman steering provides a fairly accurate dead-reckoning solution while supporting the traction and ground clearance needs of all-terrain operation and is generally the method of choice for outdoor autonomous vehicles. Associated drive implementations typically employ a gasoline or diesel engine coupled to a manual or automatic transmission, with power applied to four wheels through a transfer case, differential, and a series of universal joints. A representative example is seen in the HMMWV-based prototype of the USMC Teleoperated Vehicle (TOV) Program (Aviles et al., 1990). From a military perspective, the use of existing-inventory equipment of this type simplifies some of the logistics problems associated with vehicle maintenance. In addition, reliability of the drive components is high due to the inherited stability of a proven power train. (Significant interface problems can be encountered, however, in retrofitting off-the-shelf vehicles intended for human drivers to accommodate remote or computer control.)

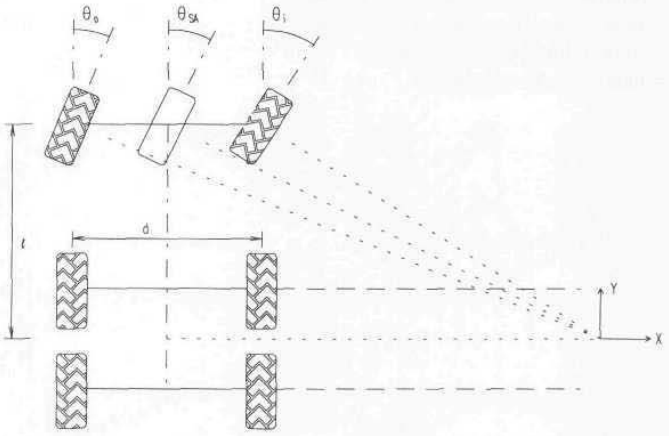

Figure 2-19. The six-wheel drive configuration employed on the Surrogate Teleoperated Vehicle suffers from excessive wheel slippage during turns as all extended axes do not intersect in a common point.

The Surrogate Teleoperated Vehicle (STV) developed by Robotic Systems Technology (Metz, et al., 1992; Myers, 1992) is loosely considered a six-wheel Ackerman-steered vehicle with twin rear axles, but the geometry (Figure 2-19) does not satisfy the Ackerman equation. The extra rear axle introduces some significant wheel slippage (and tire wear) during turns, even further aggravated by the fact that no differential action was incorporated in the chain-drive design. These detrimental effects on dead-reckoning accuracy were not all that significant

from an operational standpoint since the vehicle was directly controlled by a remote human driver, but were a major factor in the decision not to use the STV in an MDARS Exterior role.

2.3.3 Synchro Drive

An innovative configuration known as *synchro drive* features three or more wheels (Figure 2-20) mechanically coupled in such a way that all rotate in the same direction at the same speed, and similarly pivot in unison about their respective steering axes when executing a turn. This drive and steering "synchronization" results in improved dead-reckoning accuracy through reduced slippage, since all wheels generate equal and parallel force vectors at all times.

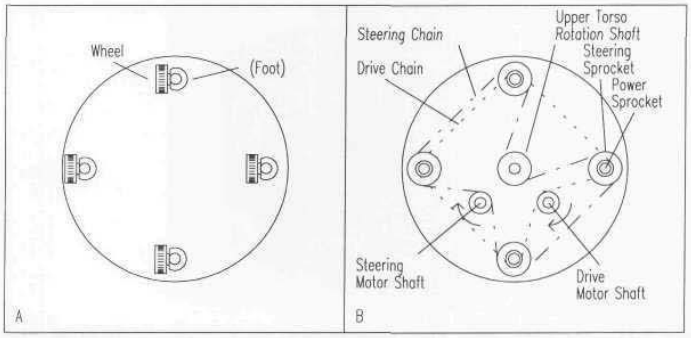

Figure 2-20. Bottom (A) and top (B) views of a four-wheel synchro-drive configuration (adapted from Holland, 1983).

The required mechanical synchronization can be accomplished in a number of ways, the most common being chain, belt, or gear drive. Carnegie Mellon University has implemented an electronically synchronized version on one of their *Rover* series robots (Figure 2-21), with dedicated drive motors for each of the three wheels. Chain- and belt-drive configurations experience some degradation in steering accuracy and alignment due to uneven distribution of slack, which varies as a function of loading and direction of rotation. In addition, whenever chains (or timing belts) are tightened to reduce such slack, the individual wheels must be realigned. These problems are eliminated with a completely enclosed gear-drive approach. An enclosed gear train also significantly reduces noise as well as particulate generation, the latter being very important in clean-room applications.

An example of a three-wheeled belt-drive implementation is seen in the Denning *MRV-2* and *Sentry* robots introduced by Denning Mobile Robots, Woburn, MA (Kadonoff, 1986). Referring to Figure 2-22, drive torque is transferred down through the three steering columns to polyurethane-filled rubber

tires. The drivemotor output shaft is mechanically coupled to each of the steering-column power shafts by a heavy-duty timing belt to ensure synchronous operation. A second timing belt transfers the rotational output of the steering motor to the three steering columns, allowing them to synchronously pivot throughout a full 360-degree range (Everett, 1988).

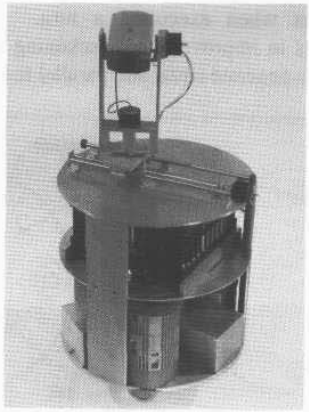

Figure 2-21. The CMU robot *Pluto* employs three electronically synchronized drive wheels (courtesy Carnegie Mellon University).

The three-point configuration ensures good stability and traction, while the actively driven large-diameter wheels provide more than adequate obstacle climbing capability for indoor scenarios. Disadvantages of this particular implementation include dead-reckoning errors introduced by compliance in the drive belts as well as by reactionary frictional forces exerted by the floor surface when turning in place.

To overcome these problems, the Cybermotion *K2A Navmaster* robot employs an enclosed gear-drive configuration with the wheels offset from the steering axis as shown in Figure 2-23. When a foot pivots during a turn, the attached wheel rotates in the appropriate direction to minimize floor and tire wear, power consumption, and slippage. Note that for correct compensation, the miter gear on the wheel axis must be on the opposite side of the power shaft gear from the wheel as illustrated. The governing equation for minimal slippage is (Holland, 1983):

$$\frac{A}{B} = \frac{r'}{r}$$

where:

A = number of teeth on the power shaft gear
B = number of teeth on the wheel axle gear
r' = wheel offset from steering pivot axis
r = wheel radius.

Figure 2-22. The Denning *MRV-2* mobility base incorporates a three-point *synchro-drive* configuration with each wheel located directly below the pivot axis of the associated steering column (courtesy Georgia Institute of Technology).

One drawback of this approach is seen in the decreased lateral stability that results when one wheel is turned in under the vehicle. Cybermotion's improved *K3A* design solves this problem (with an even smaller wheelbase) by incorporating a dual-wheel arrangement on each foot as shown in Figure 2-24 (Fisher, et al., 1994). The two wheels turn in opposite directions in differential fashion as the foot pivots during a turn, but good stability is maintained in the foregoing example by the outward swing of the additional wheel. In addition, the decreased lateral projection of the foot assembly significantly decreases the likelihood of a wheel climbing up the side of a projecting wall surface such as a column or corner, a situation that has on occasion caused the *Navmaster* to flip over.

The dead-reckoning calculations for *synchro drive* are almost trivial: vehicle heading is simply derived from the steering angle encoder, while displacement in the direction of travel is given as follows:

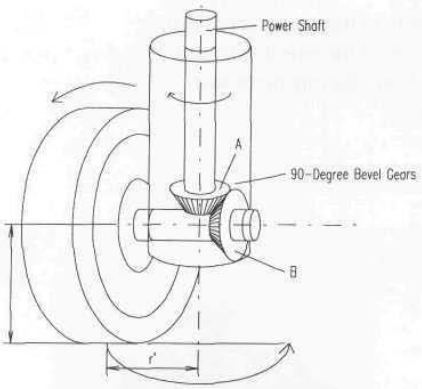

Figure 2-23. Slip compensation during a turn is accomplished through use of an offset foot assembly on the three-wheeled *K2A Navmaster* robot (adapted from Holland, 1983).

$$D = \frac{2\pi N}{C_e} R_e$$

where:

D = vehicle displacement along path
N = measured counts of drive motor shaft encoder
C_e = encoder counts per complete wheel revolution
R_e = effective wheel radius.

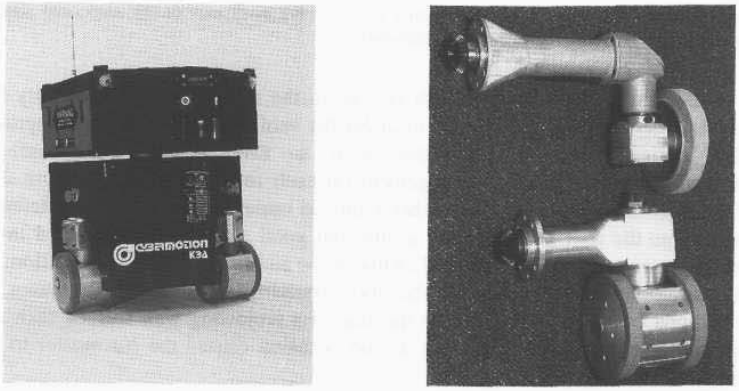

Figure 2-24. The new *K3A* dual-wheel foot assembly (bottom right) is shown in comparison to the original *K2A* assembly at the top right (courtesy Cybermotion, Inc.).

2.3.4 Tricycle Drive

Tricycle-drive configurations (Figure 2-25) employing a single driven front wheel and two passive rear wheels (or vice versa) are fairly common in AGV applications due to their inherent simplicity. For odometry instrumentation in the form of a steering angle encoder, the dead-reckoning solution is equivalent to that of an Ackerman-steered vehicle, where the drive wheel replaces the imaginary center wheel discussed in Section 2.3.2. Alternatively, if rear-axle differential odometry is used to determine heading, the solution is identical to the differential-drive configuration discussed in Section 2.3.1.

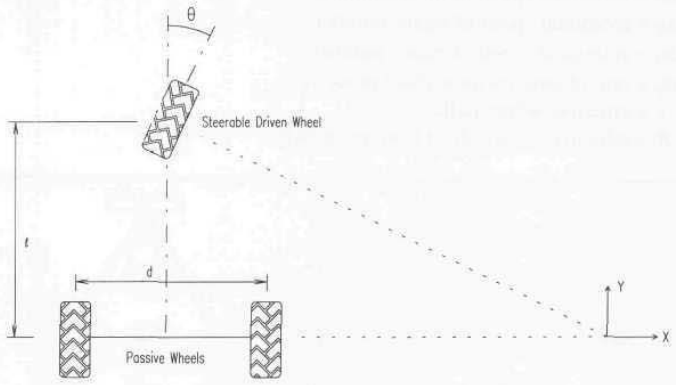

Figure 2-25. Tricycle-drive configurations employing a steerable driven wheel and two passive trailing wheels can derive heading information directly from a steering angle encoder or indirectly from differential odometry.

One problem associated with the tricycle-drive configuration is the vehicle's center of gravity tends to move away from the driven wheel when traversing up an incline, causing a loss of traction. As in the case of Ackerman-steered designs, some surface damage and induced heading errors are possible when actuating the steering while the platform is not moving.

2.3.5 Omni-Directional Drive

The dead-reckoning solution for most multiple-degree-of-freedom configurations is done in similar fashion to that for differential drive, with position and velocity data derived from the motor (or wheel) shaft- encoders. For the three-wheel example illustrated in Figure 2-26B, the equations of motion relating individual motor speeds to velocity components V_x and V_y in the reference frame of the vehicle are given by (Holland, 1983):

$$V_1 = \omega_1 r = V_x + \omega_p R$$
$$V_2 = \omega_2 r = -0.5 V_x + 0.867 V_y + \omega_p R$$
$$V_3 = \omega_3 r = -0.5 V_x - 0.867 V_y + \omega_p R$$

where:

V_1 = tangential velocity of wheel number 1
V_2 = tangential velocity of wheel number 2
V_3 = tangential velocity of wheel number 3
ω_1 = rotational speed of motor number 1
ω_2 = rotational speed of motor number 2
ω_3 = rotational speed of motor number 3
ω_p = rate of base rotation about pivot axis
r = effective wheel radius
R = effective wheel offset from pivot axis.

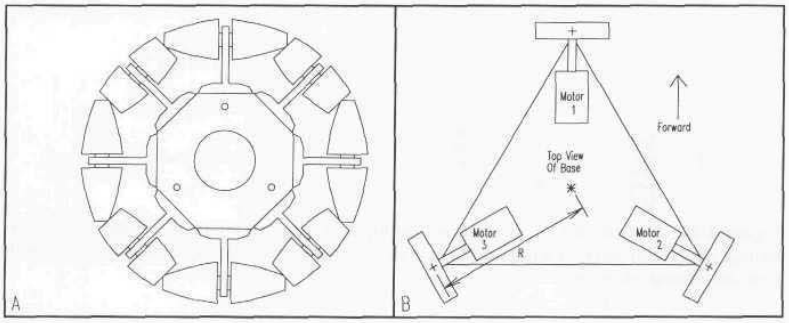

Figure 2-26. (A) Schematic of the wheel assembly used by the Veterans Administration (La, et al., 1981, © IEEE) on an omni-directional wheelchair. (B) Top view of base showing relative orientation of components in the three-wheel configuration (adapted from Holland, 1983).

The geometric relationships between wheel rotation and vehicle displacement are of course platform specific, as should be obvious from the alternative four-wheel design shown in Figure 2-27 below. Multiple-degree-of-freedom configurations display exceptional maneuverability in tight quarters in comparison to conventional 2-DOF mobility systems but have been found to be difficult to control due to their overconstrained nature (Reister, 1991; Kilough & Pin, 1992; Borenstein, 1994b). Resulting problems include increased wheel slippage, excessive tire wear, and inefficiency in operation, which can sometimes offset the not-always-required gain in maneuverability. A careful examination of all the tradeoffs involved should be made before committing to any particular drive configuration.

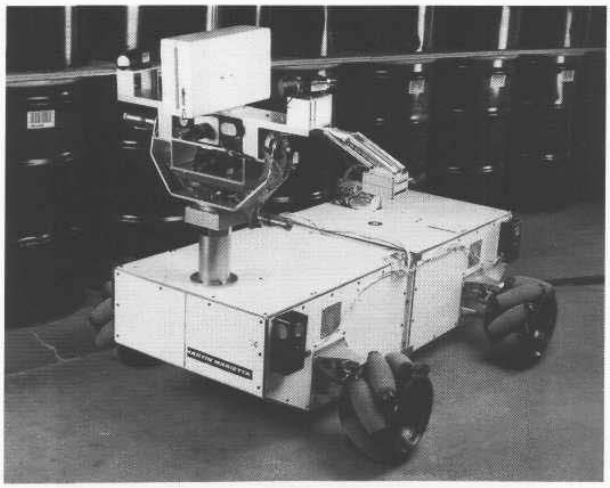

Figure 2-27. An example MDOF drive configuration developed for the Department of Energy nuclear waste inspection program (courtesy Martin Marietta, Denver).

2.4 Internal Position Error Correction

Partly motivated by the degraded navigational capabilities of MDOF vehicles, researchers at the University of Michigan have devised a clever way of significantly reducing dead-reckoning errors by one to two orders of magnitude without any external reference (Borenstein, 1994a). The *internal position error correction* scheme has been demonstrated on the *CLAPPER* (Compliant Linkage Autonomous Platform with Position Error Recovery), a 4-DOF robotic testbed consisting of two TRC *LabMate* vehicles joined together with a compliant linkage (Figure 2-28). The compliant linkage accommodates momentary controller errors without transferring any mutual force reactions between the *LabMates*, thereby eliminating excessive wheel slippage reported for alternative MDOF designs (Reister, 1991; Kilough & Pin, 1992).

More importantly, the linkage is instrumented as illustrated in Figure 2-29 to provide real-time feedback on the relative position and orientation of the two TRC platforms. An absolute encoder at each end measures the rotation of each

LabMate (with respect to the linkage) with a resolution of 0.3 degrees, while a linear encoder is used to measure the separation distance to within ±5 millimeters. A single supervisory computer reads the encoder pulses from all four drive wheels and computes each *LabMate's* dead-reckoned position and heading in conventional fashion. By examining these perceived solutions in conjunction with the known relative orientations of the two platforms, the *CLAPPER* system can detect and significantly reduce heading errors for both mobility bases.

Figure 2-28. The *CLAPPER* is a dual-differential-drive multiple-degree-of-freedom vehicle consisting of two TRC *LabMates* coupled together with a compliant linkage (courtesy University of Michigan).

The principle of operation is centered on the concept of *error growth rate* presented by Borenstein (1994a), who makes a distinction between "fast-growing" and "slow-growing" dead-reckoning errors. For example, when a differentially steered robot traverses a floor discontinuity as discussed in Section 2.3.1, it will immediately experience an appreciable orientation error (i.e., a *fast-growing* error). The associated lateral displacement error, however, is initially very small (i.e., a *slow-growing* error) but grows in an unbounded fashion as a consequence of the orientation error. The internal error correction algorithm performs relative position measurements with sufficient update rate to allow each *LabMate* to detect *fast-growing* errors in orientation, while relying on the fact that the lateral position errors accrued by both platforms during the sampling interval were very small.

The compliant linkage in essence forms a pseudo-stable heading reference in world coordinates, its own orientation being dictated solely by the relative translations of its end points, which in turn are affected only by the lateral displacements of the two *LabMate* bases. Since the lateral displacements are *slow growing*, the linkage rotates only a very small amount between encoder samples. The *fast-growing* azimuthal disturbances of the bases, on the other hand, are not coupled through the rotational joints to the linkage, thus allowing the rotary encoders to detect and quantify the instantaneous orientation errors of the bases, even when both are in motion. Borenstein (1994a) provides a more complete description of this innovative concept and reports experimental results indicating improved dead-reckoning performance up to a factor of 100.

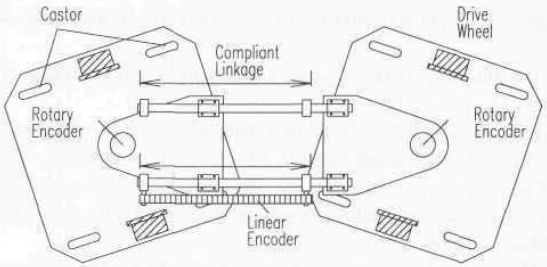

Figure 2-29. The compliant linkage is instrumented with two absolute rotary encoders and a linear encoder to measure the relative orientations and separation distance between the *LabMate* bases (adapted from Borenstein, 1994a, © IEEE).

2.5 References

Agent, A., "The Advantages of Absolute Encoders for Motion Control," *Sensors*, pp. 19-24, April, 1991.

Aviles, W.A., Everett, H.R., Hughes, T.W., Koyamatsu, A.H., Laird, R.T., Martin, S.W., McArthur, S.P., Umeda, A.Y., "Issues in Mobile Robotics: The Unmanned Ground Vehicle Program TeleOperated Vehicle (TOV)," SPIE Vol. 1388, Mobile Robots V, Boston, MA, pp. 587-597, 8-9 November, 1990.

Avolio, G., "Principles of Rotary Optical Encoders," *Sensors*, pp. 10-18, April, 1993.

Barshan, B, Durrant-Whyte, H.F., "An Inertial Navigation System for a Mobile Robot," Proceedings of the 1st IAV, Southampton, England, pp. 54-59, April 18-21, 1993.

Borenstein, J., "The CLAPPER: A Dual-drive Mobile Robot With Internal Correction of Dead Reckoning Errors," IEEE International Conference on Robotics and Automation, San Diego, CA, pp. 3085-3090, May, 1994a.

Borenstein, J., "Internal Correction of Dead-reckoning Errors with the Smart Encoder Trailer," International Conference on Intelligent Robots and Systems, Munchen, Germany, September, 1994b.

Byrne, R.H., Klarer, P.R., Pletta, J.B., "Techniques for Autonomous Navigation," Sandia Report SAND92-0457, Sandia National Laboratories, Albuquerque, NM, March, 1992.

Catling, I., *Advanced Technology for Road Transport: IVHS and ATT*, Artech House, Boston, MA, 1994.

Dahlin, T., Krantz, D., "Low-Cost, Medium Accuracy Land Navigation System," *Sensors*, pp. 26-34, February, 1988.

Deirmengian, C., "Synchros and Resolvers: Part I," *Sensors*, pp. 31-38, April, 1990a.

Deirmengian, C., "Synchros and Resolvers: Part II," *Sensors*, pp. 48-55, May, 1990b.

Dunlap, G.D., Shufeldt, H.H., *Dutton's Navigation and Piloting*, Naval Institute Press, pp. 557-579, 1972.

Everett, H.R., "A Computer Controlled Autonomous Sentry Robot," Masters Thesis, Naval Postgraduate School, Monterey, CA, October, 1982.

Everett, H.R., "Security and Sentry Robots", *International Encyclopedia of Robotics Applications and Automation*, R.C. Dorf, ed., John Wiley, pp. 1462-1476, March, 1988.

Fisher, D., Holland, J.M., Kennedy, K.F., "K3A Marks Third Generation Synchro-Drive," American Nuclear Society Winter Meeting, Proceedings of Robotics and Remote Systems, New Orleans, LA, June, 1994.

Fraden, J., *AIP Handbook of Modern Sensors*, ed., Radebaugh, R., American Institute of Physics, New York, 1993.

Grandner, W., Lanton, S., "Development of LSI Circuits for Position Encoders," *Sensors*, pp. 28, 32, April, 1986.

Harmon, S.Y., "USMC Ground Surveillance Robot (GSR): Lessons Learned," Mobile Robots, SPIE Vol. 727, Cambridge, MA, pp. 336-343, 1986.

Harrington, J.J., Klarer, P.R., "SIR-1: An Autonomous Mobile Sentry Robot," Sandia Report SAND87-1128, Sandia National Laboratories, Albuquerque, NM, May, 1987.

Henkel, S. vL., "Optical Encoders: A Review," *Sensors*, pp. 9-12, September, 1987.

Holland, J.M., *Basic Robotics Concepts*, Howard W. Sams, Macmillan, Inc., Indianapolis, IN, 1983.

Holle, S., "Incremental Encoder Basics," *Sensors*, pp. 22-30, April, 1990.

ILC Data Device Corporation, "Synchro Conversion Handbook", Bohemia, NY, April, 1982.

Jones, J.L., Flynn, A.M., *Mobile Robots: Inspiration to Implementation*, AK Peters, Ltd., Wellesley, MA, p. 141, 144, 1993.

Kadonoff, M.B., "Navigation Techniques for the Denning Sentry," MS86-757, RI/SME 2nd International Conference on Robotics Research, Scottsdale, AZ, August, 1986.

Kilough, S.M., Pin, F.G., "Design of an Omnidirectional Holonomic Wheeled Platform Prototype," IEEE Conference on Robotics and Automation, Nice, France, pp. 84-90, May, 1992.

Klarer, P.R., "Simple 2-D Navigation for Wheeled Vehicles," Sandia Report SAND88-0540, Sandia National Laboratories, Albuquerque, NM, April, 1988.

Klarer, P.R., Harrington, J.J., "Development of a Self-Navigating Mobile Interior Robot Application as a Security Guard/Sentry," Sandia Report SAND86-0653, Sandia National Laboratories, Albuquerque, NM, July, 1985.

La, W.H.T., Koogle, T.A., Jaffe, D.L., Leifer, L.J., "Microcomputer-Controlled Omnidirectional Mechanism for Wheelchairs," Proceedings, IEEE Frontiers of Engineering in Health Care, CH1621-2/81/0000-0326, 1981.

Manolis, S., Resolvers vs. Rotary Encoders For Motor Commutation and Position Feedback, *Sensors*, pp. 29-32, March, 1993.

Metz, C.D., Everett, H.R., Myers, S., "Recent Developments in Tactical Unmanned Ground Vehicles," Association for Unmanned Vehicle Systems, Huntsville, AL, June, 1992.

Milner, R., ""Measuring Speed and Distance with Doppler," *Sensors*, pp. 42-44, October, 1990.

Mononen, J., Nieminen, T., Puputti, J., "Teleoperation and Autonomous Guidance Systems for Off-Road Vehicles," International Off-Highway and Powerplant Congress and Exposition, Milwaukee, WI, Society of Automotive Engineers, ISSN 0148-7191, September, 1994.

Myers, S.D., "Update on the Surrogate Teleoperated Vehicle (STV)," Association for Unmanned Vehicle Systems, Huntsville, AL, 1992.

Nickson, P., "Solid-State Tachometry," *Sensors*, pp. 23-26, April, 1985.

Reister, D.B., "A New Wheel Control System for the Omnidirectional Hermies III Robot," IEEE Conference on Robotics and Automation, Sacramento, CA, pp. 2322-2327, April, 1991.

Sammarco, J.J., "Mining Machine Orientation Control Based on Inertial, Gravitational, and Magnetic Sensors," Report of Investigations 9326, US Bureau of Mines, Pittsburgh, PA, 1990.

Sammarco, J.J., "A Navigational System for Continuous Mining Machines," *Sensors*, pp. 11-17, January, 1994.

Schultz, W., "Traffic and Vehicle Control Using Microwave Sensors," *Sensors*, pp. 34-42, October, 1993.

Schwartz, O.B., Grafstein, P., *Pictorial Handbook of Technical Devices*, Chemical Publishing Co, Inc., New York, NY, pp. 272-275, 1971.

Tiwari, R., "Resolver-Based Encoders," *Sensors*, pp. 29-34, April, 1993.

Turpin, D.R., "Inertial Guidance: Is It a Viable Guidance System for AGVs?" 4th International Conference on AGVs (AGVS4), pp. 301-320, June, 1986.

Vaganay, J., Aldon, M.J., Fournier, A., "Mobile Robot Localization by Fusing Odometric and Inertial Measurements," Fifth Topical Meeting on Robotics and Remote Systems, Knoxville, TN, Vol. 1, pp. 503-510, April, 1993.

3
Tactile and Proximity Sensing

Tactile sensors are typically employed on automated guided vehicles (AGVs) and mobile robots to provide a last-resort indication of collisions with surrounding obstructions. As the name implies, the detection process involves *direct physical contact* between the sensor and the object of interest. *Proximity sensors*, on the other hand, are *non-contact devices* that provide advance warning on the presence of an object in close proximity to the sensing element.

3.1 Tactile Sensors

A number of different technologies are employed in various *tactile sensing* schemes (Harmon, 1983; Hall, 1984; Dario & DeRossi, 1985; Fielding, 1986; McAlpine, 1986; Pennywitt, 1986):

- Contact closure.
- Magnetic.
- Piezoelectric.
- Capacitive.
- Photoelectric.
- Magnetoresistive.
- Piezoresistive.
- Ultrasonic.

Furthermore, there are many different ways the above candidate sensing strategies can be physically configured. From a mobile robotics perspective, however, the actual embodiments can for the most part be broken down into three general areas: 1) *tactile feelers*, or *antennae*, 2) *tactile bumpers*, and 3) *distributed surface arrays*.

3.1.1 Tactile Feelers

My first experience with *tactile feelers* was in conjunction with the CRAWLER I robot introduced in Chapter 1. Tactile sensing was the only practical means available at the time (1966), due to existing limitations in both technology and my

budget, for deriving any sort of collision avoidance feedback. The first implementation consisted of a short length of guitar string extended through the center of a small screw-eye; deflection of the wire due to physical contact caused contact closure with the surrounding screw-eye, completing a simple normally open circuit. Similar implementations are reported by Russell (1984), Schiebel, et al., (1986), and Brooks (1989).

An enhanced version of the CRAWLER sensor (Figure 3-1) involved looping the wire back on itself through a second screw-eye to form a circle, thus widening the protected area. This latter design was interfaced to a punched-card reader (see Chapter 1) to support programmable collision-recovery maneuvers. Small nylon spacers (not shown in the figure) were employed to limit the vertical motion of the wire and thus prevent false activation of the sensor due to vehicle vibration. Instantaneous sensor status was represented by four state variables.

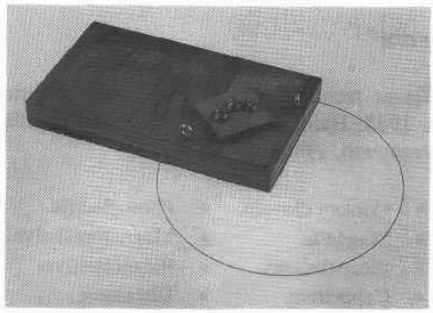

Figure 3-1. Tactile sensors situated at the four corners of the CRAWLER robots (see Chapter 1) were fabricated from guitar strings looped through the center of a pair of small screw-eyes.

Like the CRAWLER robots, ROBART I also relied heavily on tactile sensing for collision detection feedback (see also Chapter 10). The guitar-string feeler probe was mechanically upgraded slightly (Figure 3-2) to make use of an off-the-shelf automobile curb feeler. A cylindrical metal sleeve was fitted around the lower end of the feeler and electrically insulated from it by means of a short length of plastic tubing wedged into the lower half of the metal sleeve as shown in the figure. Any significant deflection of the feeler probe caused it to come into contact with the upper lip of the coaxial sleeve, completing the circuit. Additional tactile sensors used on ROBART I are discussed later in section 3.1.2.

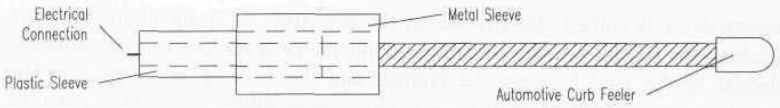

Figure 3-2. Tactile probes employed on *ROBART I* were fabricated from automobile curb feelers.

Patterned after the sensory antennae of certain insects, *active feelers* are an interesting variant of the *tactile feeler* category that incorporate some type of mechanical search strategy for increased utility and expanded coverage. Whereas the passive feelers described above rely on the relative motion between the robotic platform and the sensed object, active feelers are independently swept through a range of motion by their own dedicated actuation schemes. Kaneko (1994) describes such a system that uses a small rotary actuator to manipulate a *flexible feeler* (or *antenna*) in the horizontal plane (Figure 3-3). By careful analysis of the relationship between sensed torque and rotational displacement of the actuator after initial contact is made, the associated moment arm can be calculated. The length of this moment arm corresponds to the actual point of contact along the feeler. A similar *active-antenna* system reported by Ferrel (1994) is used on the six-legged robot *Attila* developed at MIT's Artificial Intelligence Lab in Cambridge, MA.

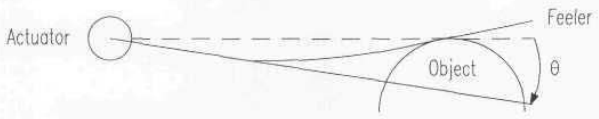

Figure 3-3. In this *active antenna* configuration, the point of actual contact along the flexible feeler can be determined by measuring the amount of rotation θ after initial contact, and the corresponding induced torque (adapted from Kaneko, 1994, © IEEE).

3.1.2 Tactile Bumpers

One of the simplest *tactile bumper* designs, common in AGV applications, consists of a flexible metal plate secured at one end and bowed out to form a protective bumper in front of the vehicle. The other end of the plate is constrained to a single degree of freedom in its motion such that any inward pressure on the plate causes the free edge to shift laterally away from the constrained edge, activating in the process some form of contact closure device (Gat, et al., 1993). This concept is similar in many respects to the previously discussed wire-loop sensors employed on the CRAWLER but with increased vertical coverage (i.e., some bumpers of this type are 18 inches high).

Rowan (1988) describes an alternative instrumentation method wherein a small retroreflective target is placed on the back of the flexible metal plate, directly in the beam of a forward-looking photoelectric sensor mounted on the front of the vehicle. If the bumper is deflected by physical contact with an obstruction, the

retroreflector is shifted laterally out of the detector's footprint of illumination, breaking the beam. Another variation on this theme involves using an inflatable bladder in the void between the bumper and the front of the vehicle. Any subsequent impact causes an increase in air pressure within the bladder, actuating a diaphragm switch assembly that halts forward motion.

The entire front panel of ROBART I was mechanically floated on a spring suspension to form a contact plate for purposes of tactile feedback (Figure 3-4). In addition, all leading structural edges were protected by hinged sections of aluminum angle that would actuate recessed microswitches in the event of obstacle contact. Flexible nylon extensions protruding from either side of the base provided coverage for the rear wheels. Note also the vertically oriented tactile feelers described in the previous section.

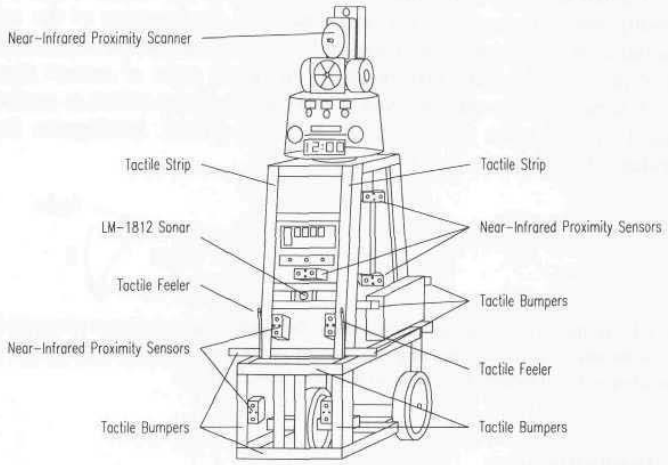

Figure 3-4. Constructed before the introduction of the Polaroid ranging module, *ROBART I* was generously equipped with tactile bumpers and feeler probes for collision detection feedback.

Relying more heavily on *sonar* and *proximity detectors* for collision avoidance protection, ROBART II employs only two tactile sensors in the form of circumferential bumpers situated around the periphery of its mobility base. Each bumper assembly consists of a free-floating plastic strip encased in a fixed housing, spring loaded to be normally in the extended position. A series of microswitches is arranged behind these housings such that individual switch elements are engaged by any displacement of the strip. When a bumper comes in contact with another surface, the floating strip is locally depressed and activates the appropriate microswitch to provide geometric resolution of the point of impact. This haptic *situation awareness* facilitates intelligent recovery by the collision avoidance software, while the housing configuration doubles as a protective bumper for the surface of the robot base.

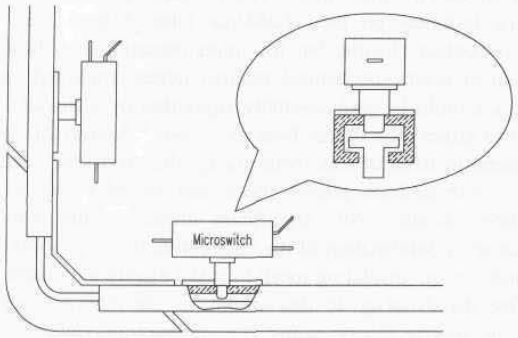

Figure 3-5. Spring-loaded tactile bumpers on ROBART II are designed to activate a series of microswitches when locally depressed, providing geometric resolution of the point of impact.

The most significant component of this continuous-bumper design is the corner piece (Figure 3-5), designed with an angled cut at both ends to mate with the floating strips in the linear encasings. When a corner comes in contact with another surface, it will press against a floating strip and thus activate the microswitch nearest the corner. The angled construction also permits lateral motion of the strips within their encasings when responding to oblique impacts.

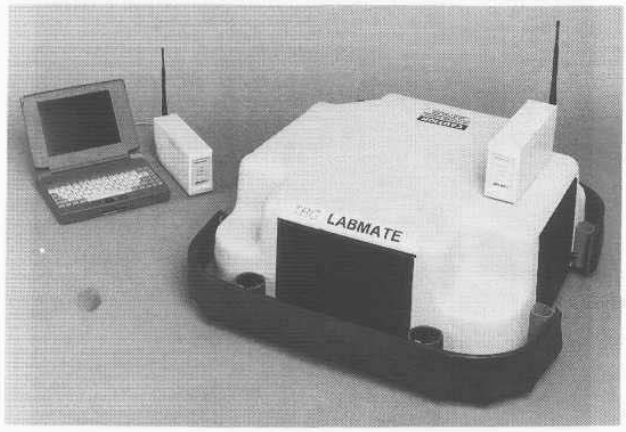

Figure 3-6. The tactile bumper employed on the *LabMate* uses a conductive foam material separated from a flexible metal backplate by an insulating mesh (courtesy Transitions Research Corp.).

Transitions Research Corporation (TRC), Danbury, CN, provides both front and rear tactile bumpers on their *LabMate* base (Figure 3-6). The sensing methodology is contact closure, but the implementation is a little more elegant than the myriad of electromechanical microswitches employed on ROBART II. Each bumper is a multi-layered assembly supported by a flexible metal backing plate attached to either side of the base as shown. A layer of conductive-foam material is placed in front of this metal backplate, electrically and mechanically isolated by an intermediate plastic mesh and covered on the outside by a protective rubber sheath. Any significant impact to the outer skin of this "sandwich" causes a deformation of the conductive foam, pushing it momentarily through the holes in the insulating mesh to make electrical contact with the metal backplate. One disadvantage to this scheme is the inherent lack of positional resolution in the strictly binary nature (i.e., contact/no-contact) of the resulting output.

Rather than instrument the entire bumper surface itself, the Cybermotion *K2A-Navmaster* design shown in Figure 3-7 below simply incorporates adjustable strain gauges in the cantilevered supporting arms to sense any impact. A minor problem with this approach is occasional false activation due to inertial loads created by vertical acceleration of the bumper assembly when traversing small cracks or bumps in the floor. When properly adjusted for actual site conditions, however, the concept works very well with minimal problems. The use of separate left and right sensors allows for some limited degree of geometric resolution of the point of impact.

Figure 3-7. The tactile bumper on the Cybermotion *K2A Navmaster* robot is configured to activate adjustable-threshold strain sensors in the left and right supporting arms (courtesy Cybermotion, Inc.)

3.1.3 Distributed Surface Arrays

There is somewhat of a growing trend (on the research side of the house anyway) to move towards embedded tactile arrays that provide two-dimensional profiling of the contacting object. In addition to geometric resolution of the point of impact, many of these strategies also provide some quantification of the contact force magnitude. Early applications involved fairly small rectangular array structures geared towards component identification and/or orientation sensing for industrial robotic scenarios and are aptly summarized in surveys presented by Harmon (1983), Dario, et al., (1985), Pennywitt (1986), Nicholls and Lee (1989), and Grahn (1992).

More recently there has been emerging interest in the development of a continuous skin-like sensor array that could be incorporated directly into the entire outer covering of a manipulator arm or even a mobile robotic vehicle. Grahn (1992) describes a tactile array produced by Bonneville Scientific, Salt Lake City, UT, that uses rows of ultrasonic transmitters and receivers to measure the thickness of an overlying rubber pad. Each element of the sensor array transmits an ultrasonic pulse that reflects off the outer surface of the rubber and returns to the sensor, thereby providing a means of precisely measuring the round-trip path length. Contact with an external object causes compression of the rubber and subsequently reduces the measured time of flight (See also chapter 5). The current 256-element sensor array (Model 200-16 X 16A) is a rigid planar structure consisting of a ceramic substrate, the PVDF transducer material, and an elastomeric pad covering.

Merritt Systems, Inc., (MSI) Merritt Island, FL, is developing a continuous flexible array of tactile and temperature sensors under a Small Business Innovative Research program managed by the Naval Command Control and Ocean Surveillance Center, San Diego, CA. The goal is to produce a conformal skin-like material containing distributed arrays of temperature and tactile sensors that can be cut into any desired shape for attachment to robotic manipulator arms or to the structural housings of mobile robotic vehicles. The company has already developed a methodology for mounting miniature ultrasonic and near-infrared proximity sensors on a flexible base material incorporating an embedded matrix of power and communications buses (MSI, undated). Up to 1022 *SmartSensor* modules may be configured into a single *SensorSkin* (Wing, 1995). The skin can be custom wrapped around the robot in a single piece (PM, 1995).

3.2 Proximity Sensors

Proximity sensors, used to determine the presence (as opposed to actual range) of nearby objects, were developed to extend the sensing range beyond that afforded by direct-contact tactile or haptic sensors. Recent advances in electronic technology have significantly improved performance and reliability, thereby

increasing the number of possible applications. As a result, many industrial installations that historically have used mechanical limit switches can now choose from a variety of alternative non-contact devices for their close (between a fraction of an inch and a few inches) sensing needs. Such *proximity sensors* are classified into several types in accordance with the specific properties used to initiate a switching action:

- Magnetic.
- Inductive.
- Ultrasonic.
- Microwave.
- Optical.
- Capacitive.

The reliability characteristics displayed by these sensors make them well suited for operation in harsh or otherwise adverse environments, while providing high-speed response and long service lives. Instruments can be designed to withstand significant shock and vibration, with some capable of handling forces over 30,000 Gs and pressures of nearly 20,000 psi (Hall, 1984). Burreson (1989) and Peale (1992) discuss advantages and tradeoffs associated with proximity sensor selection for applications in challenging and severe environments. In addition, proximity devices are valuable when detecting objects moving at high speed, when physical contact may cause damage, or when differentiation between metallic and non-metallic items is required. Ball (1986), Johnson (1987), and Wojcik (1994) provide general overviews of various alternative proximity sensor types with suggested guidelines for selection.

3.2.1 Magnetic Proximity Sensors

Magnetic proximity sensors include *reed switches*, *Hall-effect devices*, and *magnetoresistive sensors*.

Magnetic Reed Switches

The simplest form of magnetic proximity sensor is the *magnetic reed switch*, schematically illustrated in Figure 3-8. A pair of low-reluctance ferromagnetic reeds are cantilevered from opposite ends of a hermetically sealed tube, arranged such that their tips overlap slightly without touching. The extreme ends of the reeds assume opposite magnetic polarities when exposed to an external magnetic flux, and the subsequent attractive force across the gap pulls the flexible reed elements together to make electrical contact (Hamlin, 1988).

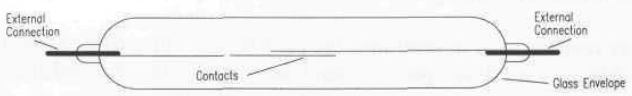

Figure 3-8. The hermetically sealed *magnetic reed switch*, shown here with normally open contacts, is filled with inert gas and impervious to dust and corrosion.

Some problems can be encountered with this type of sensor due to contact bounce, structural vibration, and pitting of the mating surfaces in the case of inductive or capacitive loads (Burreson, 1989).

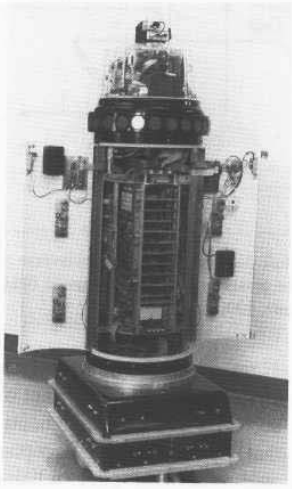

Figure 3-9. Photo of rear-access doors on ROBART II, showing location (top outer corners) of the magnetic door-closure switch (left) and its associated permanent magnet (right).

Available in both *normally open* and *normally closed* configurations, these inexpensive and robust devices are commonly employed as door- and window-closure sensors in security applications. A magnetic reed switch of this type was installed on ROBART II to monitor the status of the rear access doors as shown in Figure 3-9.

Hall Effect Sensors

The *Hall effect*, as it has come to be known, was discovered by E.H. Hall in 1879. Hall noted a very small voltage was generated in the transverse direction across a conductor carrying a current in the presence of an external magnetic field (Figure 3-10), in accordance with the following equation (White, 1988):

$$V_h = \frac{R_h IB}{t}$$

where:

V_h = Hall voltage

R_h = material-dependent Hall coefficient
I = current in amps
B = magnetic flux density (perpendicular to I) in Gauss
t = element thickness in centimeters.

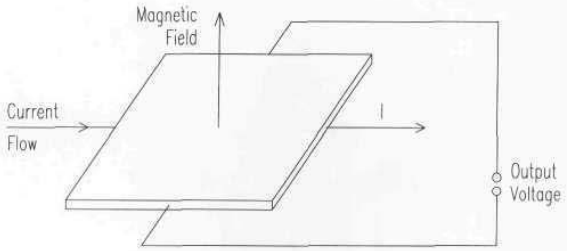

Figure 3-10. In 1879, E.H. Hall discovered a small transverse voltage was generated across a current-carrying conductor in the presence of a static magnetic field, a phenomenon now known as the *Hall effect* (adapted from Lenz, 1990).

It was not until the advent of semiconductor technology (heralded by the invention of the transistor in 1948) that this important observation could be put to any practical use. Even so, early silicon implementations were plagued by a number of shortcomings that slowed popular acceptance, including high cost, temperature instabilities, and otherwise poor reliability (McDermott, 1969). Subsequent advances in integrated circuit technology (i.e., monolithic designs, new materials, and internal temperature compensation) have significantly improved both stability and sensitivity. With a 100-milliamp current flow through *indium arsenide (InAs)*, for example, an output voltage of 60 millivolts can be generated with a flux density (B) of 10 kiloGauss (Hines, 1992). Large-volume applications in the automotive industry (such as distributor timing in electronic ignition systems) helped push the technology into the forefront in the late 1970s (White, 1988). Potential robotic utilization includes position and speed sensing, motor commutation (Manolis, 1993), guidepath following (Chapter 11), and magnetic compasses (Chapter 12).

The linear relationship of output voltage to transverse magnetic field intensity is an important feature contributing to the popularity of the modern *Hall-effect sensor*. To improve stability, *linear Hall-effect sensors* are generally packaged with an integral voltage regulator and output amplifier as depicted in the block diagram of Figure 3-11. The output voltage V_o fluctuates above and below a zero-field equilibrium position (usually half the power supply voltage V_{cc}), with the magnitude and direction of the offset determined by the field strength and polarity, respectively (White, 1988). (Note also that any deviation in *field direction* away from the perpendicular will also affect the magnitude of the voltage swing.) Frequency responses over 100 kiloHertz are easily achieved (Wood, 1986).

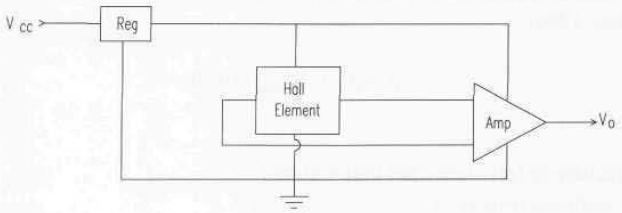

Figure 3-11. The *linear Hall-effect sensor* incorporates an integral voltage regulator and a stable DC output amplifier in conjunction with the *Hall-effect element* shown previously in Figure 3-10 above (adapted from White, 1988).

The addition of a *Schmitt-trigger* threshold detector and an appropriate output driver transforms the linear Hall-effect sensor into a digital *Hall-effect switch.* Most commercially available devices employ transistor drivers that provide an open-circuit output in the absence of a magnetic field (Wood, 1986). The detector trip point is set to some nominal value above the zero-field equilibrium voltage, and when this threshold is exceeded the output driver toggles to the *on* state (*source* or *sink*, depending on whether PNP or NPN transistor drivers are employed). A major significance of this design approach is the resulting insensitivity of the *Hall-effect switch* to reverse magnetic polarity. While the mere approach of the *south pole* of a permanent magnet will activate the device, even direct contact by the *north pole* will have no effect on switching action, as the amplified output voltage actually falls further away from the *Schmitt-trigger* setpoint. Switching response times are very rapid, typically in the 400-nanosecond range (Wood, 1986).

Magnetoresistive Sensors

For *anisotropic* materials, the value of a given property depends on the direction of measurement, in contrast to *isotropic* materials, which exhibit the same values for measured properties in all directions. *Anisotropy* may be related to the shape of a material, its crystalline structure, or internal strains (Graf, 1974). For example, the direction of magnetization in a ferromagnetic crystal will be oriented along a certain crystallographic axis known as the *easy axis*, referring to the "easy" or preferred direction of magnetization (Barrett, et al., 1973).

Changing this direction of magnetization (relative to the direction of current flow) in a conductive material through application of some external magnetic field H_y will result in a change in *resistivity* ρ of the material, a phenomenon known as the *magnetoresistive effect.* By way of illustration, rotating the magnetization state of thin-film anisotropic *permalloy* through 90 degrees causes a maximum change in resistivity of 2 to 3 percent (Dibburn & Petersen, 1986). At low temperatures, certain materials (such as bismuth) may be influenced by a factor as large as 10^6 (Fraden, 1994). The relationship of resistivity to the angle θ between

the direction of magnetization and direction of current flow is given by (Dibburn & Petersen, 1986):

$$\rho = \rho_o + \Delta\rho_{max} \cos^2 \theta$$

where:

ρ = resistivity (resistance per unit volume)
ρ_o = isotropic resistivity
$\Delta\rho_{max}$ = maximum possible change in resistivity (resulting from 90-degree rotation)
θ = angle between magnetization and direction of current flow.

In the presence of a transverse field H_y (Figure 3-12A), a permalloy strip with an original direction of magnetization M_o will exhibit the behavior shown in Figure 3-12B. As the applied field H_y is increased, the change in resistivity increases as shown until a point of saturation is reached when the angle of rotation θ becomes equal to 90 degrees, after which no further increase is possible (Petersen, 1989). The symmetry of the plot (Figure 3-12B) with respect to the vertical axis implies the resistivity value is uninfluenced by the two possible directions of original magnetization (i.e., $+M_o$, $-M_o$) or the sign of the transverse field (i.e., $+H_y$, $-H_y$).

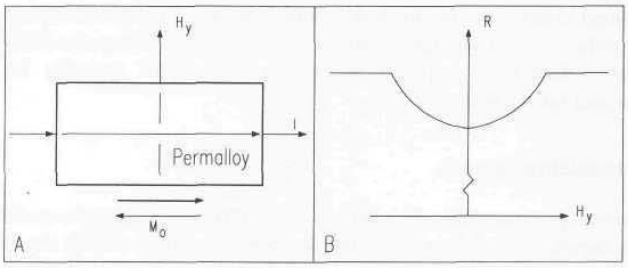

Figure 3-12. The *permalloy* strip with original direction of magnetization *Mo* as shown in (A) will exhibit a response (B) that is independent of the direction of the external transverse field H_y (adapted from Petersen, 1989).

If the demagnetizing and anisotropic fields tending to align the magnetization in the direction of current flow are represented by H_o, then:

$$\sin\theta = \frac{H_y}{H_o}$$

and so for $H_y < H_o$:

$$\rho = \rho_o + \Delta\rho_{max}\left[1 - \frac{H_y^2}{H_o^2}\right]$$

while $\rho = \rho_o$ for saturation conditions where $H_y > H_o$ (Dibburn & Petersen, 1986).

The most immediate problem with this relationship (aside from a non-unique solution) is its nonlinearity. Kwiatkowski and Tumanski (1986) review a variety of ways for biasing the magnetoresistive device to achieve linear operation over a finite range (H_y much smaller than H_o). The most common method of biasing is the "barber-pole" configuration, where gold (Dibburn & Petersen, 1986) or aluminum (Petersen, 1989) stripes are affixed to the top of each permalloy strip at a 45-degree angle. The much higher conductivity of gold (or aluminum) relative to the permalloy results in a rotation of the current-flow direction by 45 degrees as illustrated in Figure 3-13A. The net effect on the transfer function is illustrated in Figure 3-13B, which shows ρ increases linearly with H_y, for small values of H_y relative to H_o (Dibburn & Petersen, 1986). The complementary barber-pole configuration, wherein the stripes are oriented -45 degrees to the strip axis, results in a linear decrease in ρ with an increasing H_y. In either case, measuring the change in resistivity Δρ provides a reliable and accurate means for detecting very small variations in the applied magnetic field along a specific axis.

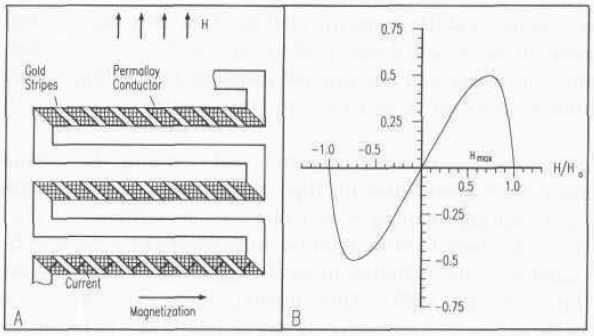

Figure 3-13. A barber-pole biasing scheme rotates the direction of current flow 45 degrees (A) to achieve a linear relationship (B) between resistivity ρ and sensed magnetic field H_y (Dibburn & Petersen, 1986).

A typical *anisotropic magnetoresistive (AMR)* sensor is constructed of four sets of *permalloy* strips, each laid down on a silicon substrate in a raster pattern and connected as shown in Figure 3-14 to form a Wheatstone bridge. Diagonally opposed elements in the bridge are biased such that for one pair ρ increases with *Hy*, while for the other pair ρ decreases. This complementary bridge configuration serves to largely eliminate effects of common-mode isotropic

variations such as temperature, while effectively doubling device sensitivity (Dibburn & Petersen, 1986).

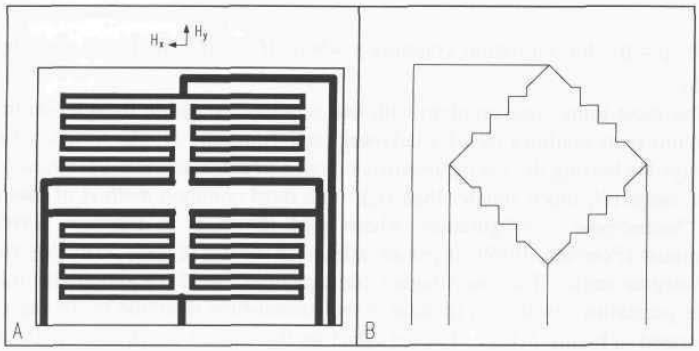

Figure 3-14. Four raster patterns of permalloy strips are connected to form a Wheatstone bridge in a typical *anisotropic magnetoresistive (AMR)* sensor (adapted from Fraden, 1994).

A second problem associated with magnetoresistive sensors is due to the bistable nature of the internal magnetization direction. A preferred magnetization is imparted along the axis of the *permalloy* strips through application of a strong magnetic field during the manufacturing process. The combination of this anisotropic structure and the geometric configuration (strip aspect ratio) means the magnetization direction will always tend to align with the longitudinal axis of the strips, even in the absence of any external magnetic field (Philips, undated). This axial alignment, however, could exist in two possible directions, 180 degrees apart.

Exposure to a strong external magnetic field opposing the internal magnetic field can cause the magnetization to "flip," reversing the internal magnetization of the strips and radically altering sensor characteristics (Figure 3-15). For most applications an auxiliary field H_x must be established along the length of the strip to ensure stability in the preferred internal magnetization direction so the sensor doesn't "flip" (Petersen, 1989). This "flipping" anomaly, however, can be put to good use in the design of a magnetoresistive compass, as will be discussed later in Chapter 12.

One way to provide this auxiliary magnetic field is through use of small permanent magnets or bias coils. The amount of bias is optimized to provide the desired sensitivity and linearity (see again Figure 3-13) but maintained sufficiently below the saturation point on the curve so as to preclude clipping (Lao, 1994). Figure 3-16 shows an example AMR device developed by Space Electronics, Inc., San Diego, CA, that incorporates an integral solenoidal bias coil in a 14-pin ceramic DIP package (SEI, 1994a; 1994b). The magnetoresistive element in the *MicroMag MMS101* is situated in a gap between two *permalloy* thin-film flux concentrators that magnify the sense-axis field component by a factor of 20, while

simultaneously shielding and reducing orthogonal components by an order of magnitude (SEI, 1994b; Lao, 1994). Selected specifications for the device are listed in Table 3-1.

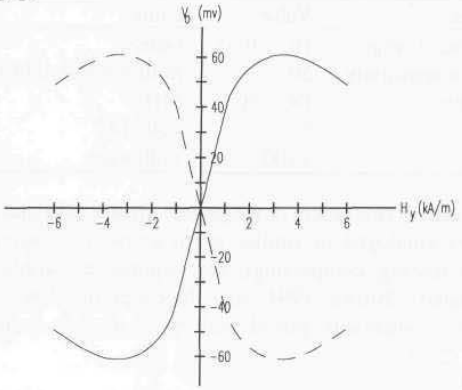

Figure 3-15. The transfer function for a "normal" magnetoresistive sensor (solid line) with magnetization oriented in the +X direction, and for a "flipped" sensor (dashed lines) oriented in the -X direction (adapted from Philips, undated).

In 1988 a French physicist by the name of Dr. Albert Fert at the University of Paris succeeded in efforts to amplify the magnetoresistive effect through fabrication of multiple thin layers of magnetoresistive materials (Baibich, et al., 1992). Such *giant magnetoresistance (GMR)* devices, as they are now called, exhibit a much larger magnetoresistive effect than do conventional *AMR* sensors (Henkel, 1994), resulting in output signals three to 20 times higher (Brown, 1994). More importantly, *GMR* devices are linear over most of their operating range, do not exhibit the characteristic "flipping" behavior of *AMR* sensors, and thus do not require a fixed-field biasing arrangement (Brown, 1994).

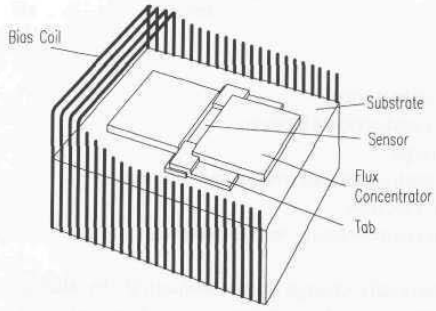

Figure 3-16. The Space Electronics, Inc. *MicroMag MMS101* monolithic AMR sensor employs integrated flux concentrators and bias coil in a 14-pin ceramic dual-inline package (SEI, 1994b).

Table 3-1. Selected specifications for *MicroMag MMS101* AMR sensor.

Parameter	Value	Units
Measurement range	10^{-5} - 0.65	Gauss
Maximum sensitivity	50	milliohms/ohm-Gauss
Bandwidth	DC - 50	MHz
Power	5	volts DC
	<100	milliwatts

The raw signal size is two orders of magnitude greater than that associated with *Hall-effect sensors* employed in similar applications (i.e., proximity, position, speed, orientation sensing, compassing), and requires less applied field for full output (NVE, undated). Brown (1994) cites three significant advantages of *GMR sensors* relative to comparably priced *Hall-effect devices* in position sensing applications:

- Increased standoff (gap) between sensor and magnet or geartooth.
- Improved high-temperature tolerance (> 200 degrees C).
- Superior temperature stability.

GMR sensors are fabricated as multiple thin-film layers of magnetic material sandwiched between alternating layers of non-magnetic conductive interlayers. The principle of operation is based on the fact that conduction electrons can have two opposite spin states, and their spin polarization (spin-state preference) in a magnetic material is determined by the direction in which the material is magnetized (Brown, 1994). The electrical *conductivity* of a material is directly proportional to the mean free path of its conduction electrons, in accordance with the following equation:

$$\sigma = \frac{nq^2 l}{mv}$$

where:

σ = material conductivity
n = number of conduction electrons
q = electron charge
l = mean free path of an electron in the material
m = mass of an electron
v = average electron velocity in the material.

GMR sensors basically change their *conductivity* by altering the mean free path of conducting electrons in the sandwich as a function of the applied magnetic field. To achieve this effect, the alternating magnetic layers in a GMR sandwich are magnetized (during fabrication) in antiparallel alignment, and consequently

their conduction electrons are spin-polarized in opposite directions. (The intermediate non-magnetic interlayers serve to separate and decouple the two magnetic films.) Conduction electrons attempting to cross the boundary between layers with opposite spin polarizations have a high probability of being scattered at the interface, resulting in a relatively short mean free path and hence low conductivity (Brown, 1994). The presence of an external magnetic field tends to rotate the antiparallel magnetization axes of the alternating layers in opposite directions towards a common orthogonal axis. Conduction electrons attempting to traverse the multi-layer junctions under these conditions subsequently encounter fewer instances of scattering, with a corresponding increase in their mean free paths.

A representative example of a commercially available *GMR* device is seen in the *NVS5B50 GMR Bridge Sensor* offered by Nonvolatile Electronics (NVE) of Eden Prairie, MN. The NVE sensor consists of four 4.7K GMR "resistors" arranged in a Wheatstone bridge configuration as shown in Figure 3-17A (Henkel, 1994). Two of these resistors are shielded from the effects of external fields by a thick magnetic material, while the other two are situated in the gap between two flux concentrators as shown in Figure 3-17B. The full-scale resistance change of the two active "sense" resistors yields a bridge output of five percent of supply voltage, compared to less than one percent for similar AMR designs (NVE, undated). The *NVS5B50* provides a linear output over the range of 0 to ±35 Gauss and is available in an 8-pin surface-mount package.

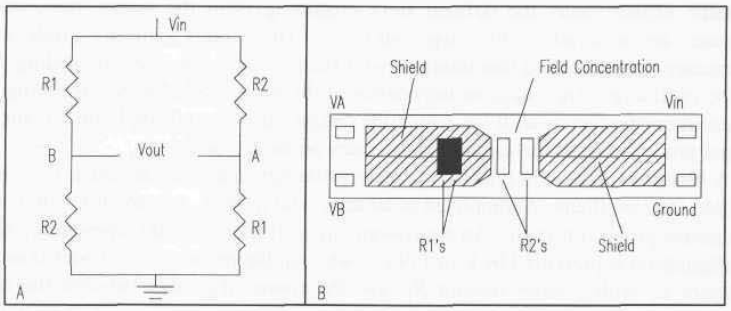

Figure 3-17. Equivalent circuit (A) and schematic drawing (B) for the Nonvolatile Electronics, Inc., *NVS5B50* GMR bridge sensor incorporating integral flux concentrators in an 8-pin surface-mount IC (adapted from Daughton, et al., 1994).

One of the most common robotic applications of AMR and GMR sensors is seen in the dead-reckoning wheel encoder application illustrated in Figure 3-18. Other uses include electronic compassing (Petersen, 1989), angle or position measurement, current sensing, and general magnetic field measurement (Henkel, 1994).

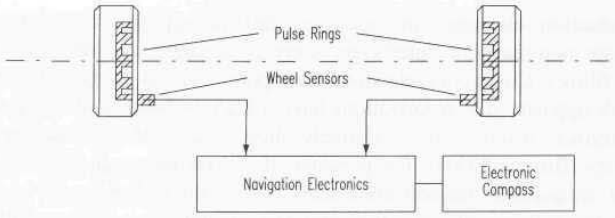

Figure 3-18. A proposed vehicle navigation system employing AMR sensors for electronic compassing (see Chapter 12) and differential wheel odometry (adapted from Petersen, 1989).

3.2.2 Inductive Proximity Sensors

Inductive proximity switches are today the most commonly employed industrial sensors (Moldoveanu, 1993) for detection of ferrous and non-ferrous metal objects (i.e., steel, brass, aluminum, copper) over short distances. Cylindrical configurations as small as 4 millimeters in diameter have been available for over a decade (Smith, 1985). Because of the inherent ability to sense through non-metallic materials, these sensors can be coated, potted, or otherwise sealed, permitting operation in contaminated work areas, or even submerged in fluids. Frequency responses up to 10 KHz can typically be achieved (Carr, 1987).

Inductive proximity sensors generate an oscillatory RF field (i.e., 100 KHz to 1 MHz) around a coil of wire typically wound around a ferrite core. When a metallic object enters the defined field projecting from the sensor face, eddy currents are induced in the target surface. These eddy currents produce a secondary magnetic field that interacts with field of the probe, thereby loading the probe oscillator. The effective impedance of the probe coil changes, resulting in an oscillator frequency shift (or amplitude change) that is converted into an output signal proportional to the sensed gap between probe and target.

A block diagram of a typical inductive proximity sensor is depicted in Figure 3-19A. The oscillator is comprised of an active device (i.e., a transistor or IC) and the sensor probe coil itself. An equivalent circuit (Figure 3-19B) representing this configuration is presented by Carr (1987), wherein the probe coil is modeled as an inductor L_p with a series resistor R_p, and the connecting cable between the coil and the active element shown as a capacitance C. In the case of a typical Collpitts oscillator, the probe-cable combination is part of a resonant frequency tank circuit.

As a conductive target enters the field, the effects of the resistive component R_p dominate, and resistive losses of the tank circuit increase, loading (i.e., damping) the oscillator (Carr, 1987). As the gap becomes smaller, the amplitude of the oscillator output continues to decrease, until a point is reached where oscillation can no longer be sustained. This effect gives rise to the special nomenclature of an *eddy-current-killed oscillator (ECKO)* for this type of configuration. Sensing gaps smaller than this minimum threshold (typically from 0.005 to 0.020 inch) are not quantified in terms of an oscillator amplitude that

correlates with range, and thus constitute a dead-band region for which no analog output is available.

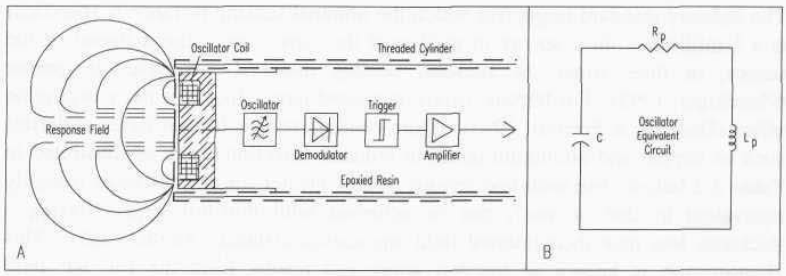

Figure 3-19. (A) Block diagram of a typical *ECKO-type* inductive proximity sensor (adapted from Smith, 1985), and (B) equivalent oscillator circuit (adapted from Carr, 1987).

Monitoring the oscillator output amplitude with an internal threshold detector (Figure 3-19A) creates an *inductive proximity switch* with a digital *on/off* output (Figure 3-20). As the metal target approaches the sensor face, the oscillator output voltage falls off as shown, eventually dropping below a preset *trigger level*, whereupon the threshold comparator toggles from an *off* state to an *on* state. Increasing the gap distance causes the voltage to again rise, and the output switches *off* as the *release level* is exceeded. The intentional small difference between the *trigger level* and the *release level*, termed *hysteresis*, prevents output instabilities near the detection threshold. Typical hysteresis values (in terms of gap distance) range from three to 20 percent of the maximum effective range (Damuck & Perrotti, 1993).

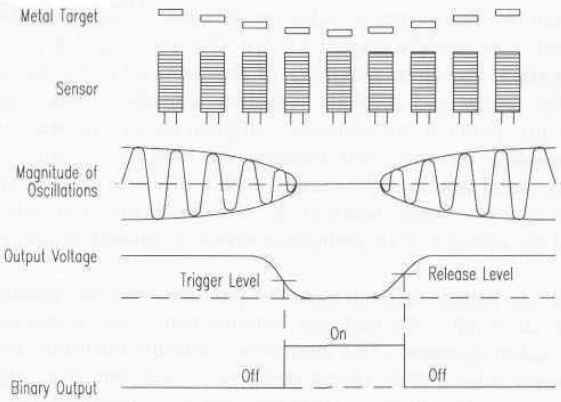

Figure 3-20. A small difference between the trigger and release levels (*hysteresis*) eliminates output instability as the target moves in and out of range (adapted from Moldoveanu, 1993).

Effective sensing range is approximately equal to the diameter of the sensing coil (Koenigsburg, 1982) and is influenced by target material, size, and shape. The industry standard target (for which the nominal sensing distance is specified) is a 1-millimeter-thick square of mild steel the same size as the diameter of the sensor, or three times the nominal sensing distance, whichever is greater (Flueckiger, 1992). For ferrous metals, increased target thickness has a negligible effect (Damuck & Perrotti, 1993). More conductive non-ferrous target materials such as copper and aluminum result in reduced detection range as illustrated in Table 3-2 below. For such non-ferrous metals, greater sensing distances (roughly equivalent to that of steel) can be achieved with thin-foil targets having a thickness less than their internal field attenuation distance (Smith, 1985). This phenomenon is known as the *foil effect* and results from the full RF field penetration setting up additional surface eddy currents on the reverse side of the target (Damuck & Perrotti, 1993).

Table 3-2. Nominal sensing ranges for material other than mild steel must be adjusted using the above attenuation factors (Smith, 1985).

Material	Attenuation Factor
Cast Iron	1.10
Mild Steel	1.00
Stainless Steel	0.70 - 0.90
Brass	0.45
Aluminum	0.40
Copper	0.35

There are two basic types of inductive proximity sensors: 1) *shielded* (Figure 3-21A), and 2) *unshielded* (Figure 3-21B). If an *unshielded* device is mounted in a metal surface, the close proximity of the surrounding metal will effectively saturate the sensor and preclude operation altogether (Swanson, 1985). To overcome this problem, the *shielded* configuration incorporates a coaxial metal ring surrounding the core, thus focusing the field to the front and effectively precluding lateral detection (Flueckiger, 1992). There is an associated penalty in maximum effective range, however, as *shielded* sensors can only detect out to about half the distance of an *unshielded* device of equivalent diameter (Swanson, 1985).

Mutual interference between inductive proximity sensors operating at the same frequency can result if the units are installed with a lateral spacing of less than twice the sensor diameter. This interference typically manifests itself in the form of an unstable pulsing of the output signal, or reduced effective range, and is most likely to occur in the situation where one sensor is undamped and the other is in the hysteresis range (Smith, 1985). Half the recommended $2d$ lateral spacing is generally sufficient for elimination of mutual interaction in the case of shielded

sensors (Gatzios & Ben-Ari, 1986). When mounting in an opposed facing configuration, these minimal separation distances should be doubled.

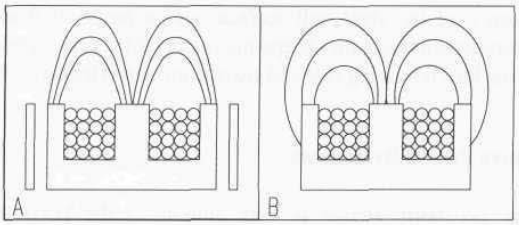

Figure 3-21. *Shielded* inductive sensors (A) can be embedded in metal without affecting performance, while the *unshielded* variety (B) must be mounted on non-metallic surfaces only (Flueckiger, 1992).

While most standard inductive proximity sensors operate on the *ECKO* principle and detect any and all metallic materials, some applications may call for differentiation between various types of metals. The Micro Switch Division of Honeywell Corporation offers an RF inductive *ECKO* sensor series that detects only ferrous (primary component iron) metals, with a 10 to 15 percent decrease in nominal ranges compared to an all-metals sensor (Dixon, 1990). Because of their selective targeting and extremely limited sensing ranges, inductive sensors in general have minimal use in mobile robotic systems for purposes of external object detection, except in application-specific instances.

Figure 3-22. This robotic shot-blasting device employs inductive proximity sensors to keep the closed-cycle end-effector in sealed contact with the ship's hull (courtesy Barnes and Reineke).

One such example involves a large industrial manipulator developed by Barnes and Reineke, Chicago, IL, that cleans the exterior hulls of ships in drydock with steel-shot abrasive (Figure 3-22). Three analog inductive sensors are used to sense the presence of the steel hull surface over a range of 0 to 1.75 inches, controlling a servomechanism that keeps the manipulator under preloaded contact as it traverses the hull removing rust and marine growth (Henkel, 1985).

3.2.3 Capacitive Proximity Sensors

The *capacitive proximity sensor* is very similar to the previously discussed *inductive proximity sensor*, except the capacitive type can reliably detect dielectric materials in addition to metals. Effective for short-range detection out to a few inches, such sensors react to the variation in electrical capacitance between a probe (or plate) and its surrounding environment. As an object draws near, the changing geometry and/or dielectric characteristics within the sensing region cause the capacitance to increase. This change in capacitance can be sensed in a number of different ways: 1) an increase in current flow through the probe (Hall, 1984), 2) initiation of oscillation in an RC circuit (McMahon, 1987), or 3) a decrease in the frequency of an ongoing oscillation (Vranish, et al., 1991). Typical industrial applications include level sensing for various materials (i.e., liquids, pellets, and powders) and product detection, particularly through non-metallic packaging.

An interesting application specifically intended for robotic collision avoidance is seen in the *Capaciflector* developed by the Robotics Branch at NASA Goddard Space Flight Center, Greenbelt, MD. The NASA objective was to produce a conformal proximity-sensing skin for use on robotic manipulator arms in both industrial and space applications, capable of sensing a human presence up to 12 inches away. Normally this type of range requirement would necessitate mounting the capacitive sensor plate with a stand-off displacement of about an inch from the grounded robot arm as illustrated in Figure 3-23A, creating unacceptable bulk and mechanical interference (Vranish, et al., 1991). The NASA design, based on an instrumentation technique for controlling stray capacitance (Webster, 1988), eliminates this offset requirement by introducing an intermediate *reflector* surface between the arm structure and the sensor plate as shown in Figure 3-23B.

In the conventional case (no reflector) illustrated in Figure 3-23A, the smaller the stand-off distance, the greater the capacitive coupling between the sensor plate and the robotic arm, with a corresponding decrease in the strength of the field projected away from the sensor in the direction of the object. The addition of an intermediate active reflector (driven in phase with the sensor plate) causes the sensor field lines to be reflected away from the robot structure, thereby significantly increasing the range of possible interaction with surrounding objects. The equivalent effect (in terms of increased detection range) of a large stand-off is

achieved, but without adding unnecessary bulk to the robot's mechanical structure, since the effective offset is approximately equal to the reflective shield thickness of 0.06 inches (Vranish, et al., 1991). A single-element feasibility prototype attached to a *PUMA* industrial manipulator was demonstrated to routinely detect a human or aluminum structural element at distances out to 12 inches, and even smaller objects such as a graphite pencil lead at ranges of around 5 inches (Vranish, et al., 1991).

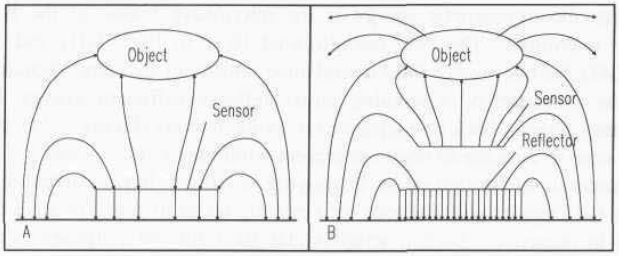

Figure 3-23. Electric field lines without a reflector are shown in (A), while the use of a reflector in (B) allows for greater detection range (adapted from Vranish, et al., 1991).

3.2.4 Ultrasonic Proximity Sensors

All of the preceding proximity sensors relied on target presence to directly change some electrical characteristic or property (i.e., inductance, capacitance) associated with the sense circuitry itself. The ultrasonic proximity sensor is an example of a *reflective* sensor that responds to changes in the amount of emitted energy returned to a detector after interaction with the target of interest. Typical systems consist of two transducers (one to transmit and one to receive the returned energy), although the relatively slow speed of sound makes it possible to operate in the transceiver mode with a common transducer. The transmitter emits a longitudinal wave in the ultrasonic region of the acoustical spectrum (typically 20-200 KHz), above the normal limits of human hearing. The receiver response is a function of the amplitude of the returned energy, as opposed to elapsed time before detection of an echo.

Ultrasonic proximity sensors are useful over distances out to several feet for detecting most objects, liquid and solid. If an object enters the acoustical field, energy is reflected back to the receiver. As is the case with any reflective sensor, maximum detection range is dependent not only on emitted power levels, but also on target cross-sectional area, reflectivity, and directivity. Once the received signal amplitude reaches a preset threshold, the sensor output changes state, indicating detection. Due in part to the advent of low-cost microcontrollers, such devices have for most situations been replaced by more versatile ultrasonic

ranging systems (Chapter 5) that provide a quantitative indicator of distance to the detected object.

3.2.5 Microwave Proximity Sensors

Microwave proximity sensors operate at distances of 5 to 150 feet or more (Williams, 1989) and are very similar to the ultrasonic units discussed above, except that electromagnetic energy in the microwave region of the RF energy spectrum is emitted. The FCC has allocated 10.50 to 10.55 GHz and 24.075 to 24.175 GHz for microwave field-disturbance sensors of this type (Schultz, 1993). When the presence of a suitable target reflects sufficient energy from the transmitting antenna back to a separate receiving antenna (Figure 3-24), the output changes state to indicate an object is present within the field of view.

An alternative configuration employing a single transmit/receive antenna monitors the Doppler shift induced by a moving target to detect relative motion as opposed to presence. Such a setup is classified for our purposes as a motion sensor and treated in Chapter 17.

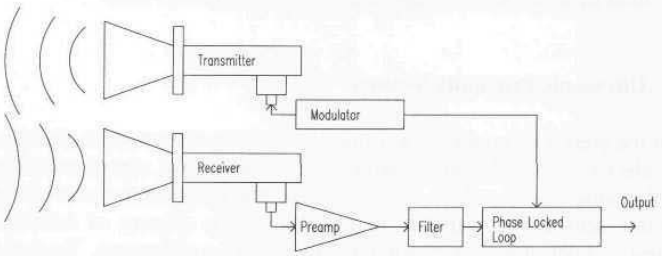

Figure 3-24. The microwave presence sensor, unlike the motion detector, requires a separate transmitter and receiver (adapted from Williams, 1989).

AM Sensors Microwave Proximity Sensors

AM Sensors, Inc., Salem, MA, offers a variety of proximity, direction of motion, displacement, level, and velocity sensors which cover numerous industrial applications. Their products include the *MSM10500* series of FMCW microwave sensors that provide non-contact position detection of metallic and non-metallic moving objects. The *MSM10500* sensor provides continuous distance information, range-gated position indication, and direction of motion. The *MSM10502* is preset to sense objects moving either toward or away from the sensor, and indicates distance as it passes through three range gates that can be adjusted to any fraction of the 50-foot maximum detection range. The microwave portion of the unit uses a *Gunn-diode* transmitter, two microwave *mixer-diode* receivers, and a *varactor diode* to vary the transmitted frequency. The output of

the oscillator is focused by a horn antenna into a beam, and any object moving through this beam is detected.

The signal conditioning circuitry contains the power supply, amplifiers, comparator, and a microcontroller to drive the oscillator and convert the detected outputs into useful control signals. The amount of averaging applied to each reading is adjustable so the user may choose between maximum noise immunity and minimum output response time. The regulated power supply allows the module to operate with a wide range of input voltages, such as in automotive systems, and provide high electrical noise rejection. When the target is inside a given range, the corresponding output will turn on and remain on as long as the target is within this range, specified in normal environments to be accurate within 6 inches. This accuracy can be degraded if there are multiple targets moving in the range or if the target has low reflectivity. The point where a range gate will turn on for a given target is typically repeatable within 1 inch.

Table 3-3. Performance specifications of AM Sensors MSM10500 and MSM10502 microwave proximity sensors.

Parameter	MSM10500	MSM10502	Units
Range	50	50	feet
Resolution	6	6	inches
Size	6.5 by 6.5 by 4.25	4.25 by 4.25 by 3.5	inches
Weight	1	1	pound
Power	10 to 16	10 to 28	volts
	150	50	milliamps
Range gates	Adjustable	Preset at 3, 5, 10	feet
Frequency	10.525	10.525	GHz

3.2.6 Optical Proximity Sensors

Optical (photoelectric) sensors commonly employed in industrial applications can be broken down into three basic groups: (1) *opposed*, (2) *retroreflective*, and (3) *diffuse*. (The first two of these categories are not really "proximity" sensors in the strictest sense of the terminology.) Effective ranges vary from a few inches out to several feet. Common robotic applications include floor sensing, navigational referencing, and collision avoidance. Modulated near-infrared energy is typically employed to reduce the effects of ambient lighting, thus achieving the required signal-to-noise ratio for reliable operation. Visible-red wavelengths are sometimes used to assist in installation alignment and system diagnostics.

Actual performance depends on several factors. Effective range is a function of the physical characteristics (i.e., size, shape, reflectivity, and material) of the object to be detected, its speed and direction of motion, the design of the sensor, and the quality and quantity of energy it radiates or receives. Repeatability in

detection is based on the size of the target object, changes in ambient conditions, variations in reflectivity or other material characteristics of the target, and the stability of the electronic circuitry itself. Unique operational characteristics of each particular type can often be exploited to optimize performance in accordance with the needs of the application.

Opposed Mode

Commonly called the "electric eye" at the time, the first of these categories was introduced into a variety of applications back in the early 1950s, to include parts counters, automatic door openers, annunciators, and security systems. Separate transmitting and receiving elements are physically located on either side of the region of interest; the transmitter emits a beam of light, often supplied in more recent configurations by an LED, that is focused onto a photosensitive receiver (Figure 3-25). Any object passing between the emitter and receiver breaks the beam, disrupting the circuit. Effective ranges of hundreds of feet or more are routinely possible and often employed in security applications.

Figure 3-25. The *opposed-mode sensor* configuration relies on target passage between the emitter and detector to interrupt the beam.

Other than a few specialized cases of internal sensing (such as certain types of optical encoders) *opposed-mode sensors* have little applicability to mobile robotic systems due to their geometric configuration (i.e., opposed-pair transmitter and receiver elements).

Retroreflective Mode

Retroreflective sensors evolved from the *opposed* variety through the use of a mirror to reflect the emitted energy back to a detector located directly alongside the transmitter. *Corner-cube retroreflectors* (Figure 3-26) eventually replaced the mirrors to cut down on critical alignment needs. Corner-cube prisms have three mutually perpendicular reflective surfaces and a hypotenuse face; light entering through the hypotenuse face is reflected by each of the surfaces and returned back through the face to its source (Banner, 1993b).

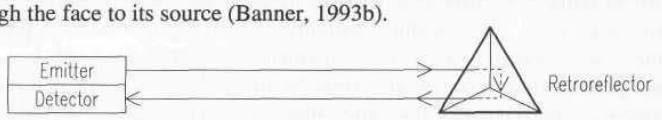

Figure 3-26. *Corner-cube retroreflectors* are employed to increase effective range and simplify alignment (adapted from Banner, 1993b).

In most factory automation scenarios, the object of interest is detected when it breaks the beam, although some applications call for placing the retroreflector on the item itself. A good retroreflective target will return about 3,000 times as much energy to the sensor as would be reflected from a sheet of white typing paper (Banner, 1993b).

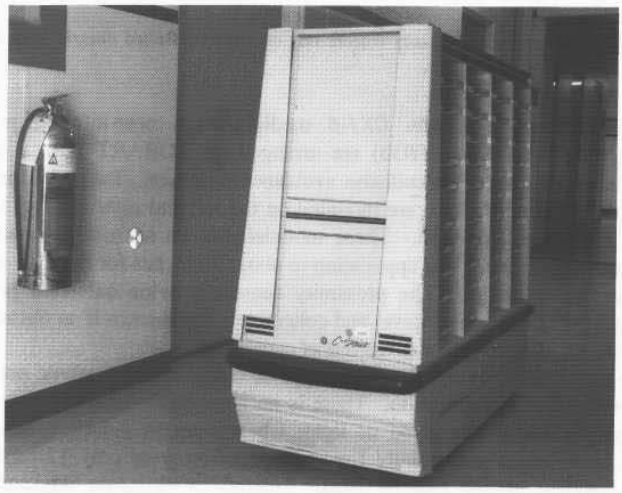

Figure 3-27. Earlier versions of this automated mail delivery cart relied on wall-mounted retroreflectors (left of doorway) to identify desired stops along the route; the current system senses longitudinal markers on the floor adjacent to the guidepath (courtesy Naval Command Control and Ocean Surveillance Center).

Collocation of the emitter and detector simplified installation in industrial assembly-line scenarios and opened up several applications for mobile systems as well. One common example is seen in the employment of fixed-location retroreflective reference markers for automated guided vehicles. Figure 3-27 shows a typical implementation in conjunction with a Bell and Howell mail delivery system in operation at NCCOSC. The circular retroreflective target mounted on the wall adjacent to the office doorway was used to mark a position along the route of travel where the platform is supposed to stop. (The present system actually senses a longitudinal marker on the floor adjacent to the guidepath, as will be discussed in Chapter 11). An onboard annunciator then alerts the secretarial staff to deposit outgoing mail in a collection bin and collect any mail intended for delivery at that particular station.

Diffuse Mode

Optical proximity sensors in the *diffuse* category operate in similar fashion to *retroreflective* types, except that energy is returned from the surface of the object of interest, instead of from a *cooperative reflector* (Figure 3-28). This feature facilitates random object detection in unstructured environments.

Figure 3-28. *Diffuse-mode proximity sensors* rely on energy reflected directly from the target surface.

Three Banner *Multi-Beam CX1-6* medium-range near-infrared proximity detectors (Banner, 1993a; 1993b) are arranged on ROBART II in a forward-looking horizontal array for collision avoidance purposes. Two additional units (*Mini-Beam* model *SM312D*) are mounted on the left and right sides of the front panel of the lower base unit. These modulated-beam sensors have adjustable maximum ranges, set for this application to about 30 inches for the *CX1-6* and 15 inches for the *SM312D*. The proximity sensors provide extended protection capability in the direction of travel and collectively can discern if an obstruction is directly ahead, to the right, or to the left of centerline.

There are several advantages of this type of sensor over ultrasonic ranging for close-proximity object detection. There is no appreciable time lag since optical energy propagates at the speed of light, whereas up to a full second can be required to update a sequentially fired ultrasonic array of only 12 sensors. In addition, optical energy can be easily focused to eliminate adjacent sensor interaction, thereby allowing multiple sensors to be fired simultaneously. Finally, the shorter wavelengths involved greatly reduce problems due to specular reflection, resulting in more effective detection of off-normal surfaces (see chapters 8 and 9). The disadvantage, of course, is that no direct range measurement is provided, and variations in target reflectivity can sometimes create erratic results. One method for addressing this limitation is discussed in the next section.

Convergent Mode

Diffuse proximity sensors can employ a special geometry in the configuration of the transmitter with respect to the receiver to ensure more precise positioning information. The optical axis of the transmitting LED is angled with respect to that of the detector, so the two intersect only over a narrowly defined region as illustrated in Figure 3-29. It is only at this specified distance from the device that a target can be in position to reflect energy back to the detector. Consequently, most targets beyond this range are not detected. This feature decouples the

proximity sensor from dependence on the reflectivity of the target surface, and is useful where targets are not well displaced from background objects.

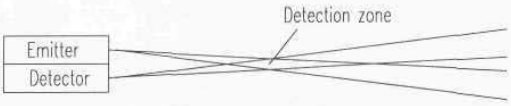

Figure 3-29. *Diffuse proximity sensors* configured in the *convergent mode* can be used to ascertain approximate distance to an object.

Convergent-mode sensors were used on ROBART II to detect discontinuities in the floor, such as a descending stairway, where significant variations in floor surface reflectivities precluded the use of diffuse-mode sensors. A Banner *SM512DB* near-infrared sensor is installed on the front and a model *SE612* on each corner of the base. The sensors are positioned to detect the normal presence of the floor, to preclude attempts to traverse unsuitable discontinuities that could entrap or even damage the unit. Any undesirable conditions detected by these sensors cause the drive motors to be immediately disabled, and the controlling processor is alerted to which corner sensor detected the problem.

In the early 1980s, Honeywell Visitronics, Englewood, CO, developed an interesting non-contact proximity gauge that employed the convergent sensing technique to determine relative distance as well as the presence or absence of an object. The *HVS-300 Three Zone Distance Sensor* (no longer available) would indicate whether a target surface was close to the sensor, at an intermediate distance, far from the sensor, or out of range. Conventional diffuse proximity detectors based on return signal intensity display high repeatability only when target surface reflectivity is maintained constant. The *HVS-300* was capable of higher range accuracy under varying conditions of reflectivity and ambient lighting through use of the triangulation ranging scheme.

The *HVS-300* proximity sensor consisted of a pair of 820-nanometer near-infrared LED sources, a dual-element silicon photodetector, directional optics, and control logic circuitry. The LEDs emitted coded light signals at differing angles through one side of a directional lens as shown in Figure 3-30. If an outgoing beam struck an object, a portion of the reflected energy was returned through the other side of the lens and focused onto the detector assembly.

The detector employed two photodiode elements placed side by side, separated by a narrow gap. Depending on the range to the reflective surface, a returning reflection would either fall on one photodetector (indicating the reflecting surface was close to the sensor), or the other (indicating the surface was far from the sensor), or equally on both (meaning the object was on the boundary between these two regions). With two separate transmissions projected onto the scene at different angles of incidence, two such boundaries were created. The first distinguished between the *near* and *intermediate* regions, while the second distinguished between the *intermediate* and *far* regions. Because both

transmissions used the same detector, the sources were uniquely coded for positive identification by the control electronics.

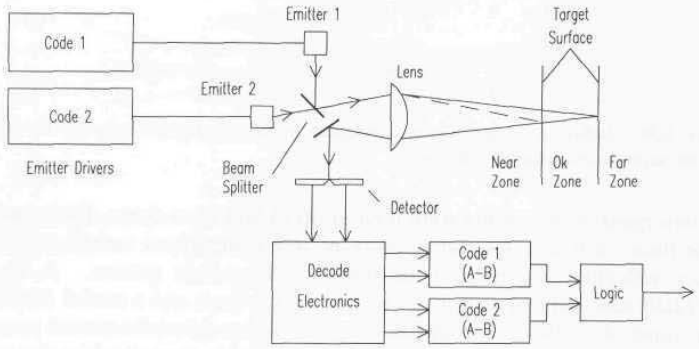

Figure 3-30. The Honeywell *HVS-300* proximity sensor incorporated dual near-infrared emitters to determine if an object was in the adjustable OK zone (courtesy Honeywell Visitronics, Inc.).

Generally insensitive to changes in surface texture or color and unaffected by ambient lighting conditions, the *HVS-300* seemed well suited to the collision avoidance needs of an indoor mobile robot, where the limited speed of advance was in keeping with the sensor's maximum range of 30 inches. In addition, the four discrete range bins would give a relative feel for the distance to a threatening object, allowing for more intelligent evasive maneuvering. Unfortunately, the higher unit cost relative to ultrasonic ranging systems and conventional diffuse-mode proximity detectors was hard to justify, and subsequent advances in position sensitive detectors (PSDs) made competing triangulation ranging systems even more attractive (see Chapter 4).

3.3 References

Baibich, M., Broto, J., Fert, A., Van Dau, F.N., Petroff, F., Eitenne, P., Creuzet, G., Friederich, A., Chazelas, J., "Giant Magnetoresistance of (001) Fe/(001) Cr Magnetic Super Lattices," Physical Review Letters, Vol. 61, No. 21, p. 2472, November, 1992.

Ball, D., "Sensor Selection Guide," *Sensors*, pp. 50-53, April, 1986.

Banner, *Photoelectric Controls*, Product Catalog, Banner Engineering Corp., Minneapolis, MN, 1993a.

Banner, *Handbook of Photoelectric Sensing*, Banner Engineering Corp., Minneapolis, MN, 1993b.

Barrett, C.R., Nix, W.D., Tetelman, A.S., *The Principles of Engineering Materials*, Prentice Hall, Englewood Cliffs, NJ, 1973.

Brooks, R.A., "A Robot that Walks: Emergent Behaviors from a Carefully Evolved Network," *Neural Computation*, Vol. 1, pp. 253-262, 1989.

Brown, J., "GMR Materials: Theory and Applications," *Sensors*, pp. 42-48, September, 1994.

Burreson, B., "Magnetic Proximity Switches in Severe Environments," *Sensors*, pp. 28-36, June, 1989.

Carr, W.W., "Eddy Current Proximity Sensors," *Sensors*, pp. 23- 25, November, 1987.

Damuck, N., Perrotti, J., "Getting the Most out of Your Inductive Proximity Switch," *Sensors*, pp. 25-27, August, 1993.

Dario, P., DeRossi, D., "Tactile Sensors and the Gripping Challenge," *IEEE Spectrum*, pp. 46-52, August, 1985.

Daughton, J., Brown, J., Chen, E., Beech, R., Pohm, A., Kude, W., "Magnetic Field Sensors Using GMR Multilayer," *IEEE Transactions on Magnetics*, Vol. 30, No. 6, pp. 4608-4610, November, 1994.

Dibburn, U., Petersen, A., "The Magnetoresistive Sensor - a Sensitive Device for Detecting Magnetic Field Variations," *Electronic Components and Applications*, Vol. 5, No. 3, June, 1983.

Dixon, D., "Ferrous Metals Only Inductive Proximity Sensors," *Sensors*, pp. 18-20, April, 1990.

Ferrel, C.L., "An Autonomous Mobile Robot, a Planetary Microrover," *Sensors*, pp. 37-47, February, 1994.

Fielding, P.J., "Evaluation of Robotic Tactile Sensing System," *Sensors*, pp. 35-46, April, 1986.

Fraden, J., *AIP Handbook of Modern Sensors*, ed., Radebaugh, R., American Institute of Physics, New York, 1993.

Flueckiger, N., "Inductive Proximity Sensors: Theory and Applications," *Sensors*, pp. 11-13, May, 1992.

Gat, E., Behar, A., Desai, R., Ivlev, R., Loch, J., Miller, D.P., "Behavior Control for Planetary Exploration," IEEE International Conference on Robotics and Automation, Atlanta, GA, Vol. 2, pp. 567-571, May, 1993.

Gatzios, N.E., Ben-Ari, H., "Proximity Control Primer," *Sensors*, pp. 47-49, April, 1986.

Graf, R.F., *Dictionary of Electronics*, Howard W. Sams, Indianapolis, IN, 1974.

Grahn, J.M., "Robotic Applications for Tactile Sensors," Sensors Expo, Chicago, IL, pp. 63-73, September, 1992.

Hall, D.J., "Robotic Sensing Devices," Report No. CMU-RI-TR-84-3, Carnegie-Mellon University, Pittsburgh, PA, March, 1984.

Hamlin, "The Versatile Magnetic Proximity Sensor," *Sensors*, pp. 16-22, May, 1988.

Harmon, L.D., "Tactile Sensing for Robots," Recent Advances in Robotics, Vol. 1, John Wiley and Sons, 1983.

Henkel, S. vL., "Hull Cleaning System for Trident-Class Submarines," *Robotics Age*, p. 11, November, 1985.

Henkel, S. vL., "GMR Materials Advance Magnetic Field Detection," *Sensors*, p. 8, June, 1994.

Hines, R., "Hall Effect Sensors in Paddlewheel Flowmeters," *Sensors*, pp. 32-33, January, 1992.

Johnson, R.F., "A Refresher in Position Sensing," *Sensors*, pp. 18-24, September, 1987.

Kaneko, M., "Active Antenna," IEEE International Conference on Robotics and Automation, San Diego, CA, pp. 2665-2671, May, 1994.

Koenigsburg, W.D., "Noncontact Distance Sensor Technology," GTE Laboratories, Inc., 40 Sylvan Rd., Waltham, MA, 02254, pp. 519-531, March, 1982.

Kwiatkowski, W., Tumanski, S., "The Permalloy Magnetoresistive Sensors - Properties and Applications," *Journal of Physics E: Scientific Instruments*, Vol. 19, pp. 502-515, 1986.

Lao, R., "A New Wrinkle in Magnetoresistive Sensors," *Sensors*, pp. 63-65, October, 1994.

Lenz, J.E., "A Review of Magnetic Sensors," *Proceedings of the IEEE*, Vol. 78, No. 6, June, 1990.

Manolis, S., Resolvers vs. Rotary Encoders For Motor Commutation and Position Feedback, *Sensors*, pp. 29-32, March, 1993.

McAlpine, G.A., "Tactile Sensing," *Sensors*, pp. 7-16, April, 1986.

McDermott, J., "The Hall Effect: Success at 90," *Electronic Design 21*, pp. 38-45, 11 October, 1969.

McMahon, V.C., "Solutions from Capacitive Proximity Switches," *Sensors*, pp. 31-33, May, 1987.

Moldoveanu, A., "Inductive Proximity Sensors: Fundamentals and Standards," *Sensors*, pp. 11-14, June, 1993.

MSI, "Proximity Sensing Products," Product Literature, Merritt Systems, Inc., Merritt Island, FL, undated.

Nicholls, H.R., Lee, M.H., "A Survey of Robotic Tactile Sensing Technology," *The International Journal of Robotics Research*, Vol. 8, No. 3, June, 1989.

NVE, "NVS5B50 GMR Bridge Sensor," Preliminary Product Literature, Nonvolatile Electronics, Inc., Eden Prairie, MN, undated.

Peale, S., "Speed/Motion Sensing in Challenging Environments," *Sensors*, pp. 45-46, January, 1992.

Pennywitt, K.E., "Robotic Tactile Sensing," *Byte*, pp. 177-200, January, 1986.

Petersen, A., "Magnetoresistive Sensors for Navigation," Proceedings, 7th International Conference on Automotive Electronics, London, England, pp. 87-92, October, 1989.

Philips, "The Magnetoresistive Sensor: A Sensitive Device for Detecting Magnetic-Field Variations," Technical Publication 268, Philips Components, undated.

PM, "Robots Get Sensitive," *Popular Mechanics*, p. 20, February, 1995.

Rowan, J., "The Decade of the Sensor in Materials Handling," *Sensors*, pp. 11-13, April, 1988.

Russell, R.A., "Closing the Sensor-Computer-Robot Control Loop," *Robotics Age*, pp. 15-20, April, 1984.

Schiebel, E.N., Busby, H.R., Waldren, K.J., "Design of a Mechanical Proximity Sensor," IEEE International Conference on Robotics and Automation, pp. 1941-1946, 1986.

SEI, "*Micromag* Application Note AN-1," Space Electronics, Inc., San Diego, CA, May, 1994a.

SEI, "High-Sensitivity Magnetoresistive Magnetometer," Product Literature, MMS101, Space Electronics, Inc., San Diego, CA, June, 1994b.

Smith, J.W., "Design and Application of Inductive Proximity Sensors," *Sensors*, pp. 9-14, November, 1985.

Swanson, R., "Proximity Switch Application Guide," *Sensors*, pp. 20-28, November, 1985.

Vranish, J.M., McConnel, R.L., Mahalingam, S., "Capaciflector Collision Avoidance Sensors for Robots," Product Description, NASA Goddard Space Flight Center, Greenbelt, MD, February, 1991.

Vranish, J.M., McConnell, R.L., "Driven Shielding Capacitive Proximity Sensor, *NASA Tech Briefs*, p. 16, March, 1993.

Webster, J.G., *Tactile Sensors for Robotics and Medicine*, John Wiley and Sons, New York, NY, 1988.

White, D., "The Hall Effect Sensor: Basic Principles of Operation and Application," *Sensors*, pp. 5-11, May, 1988.

Williams, H., "Proximity Sensing with Microwave Technology," *Sensors*, pp. 6-15, June, 1989.

Wingo, W., "Freckled 'Skin' Gives Keener Senses to Robots," *Design News*, p. 16, January 9, 1995.

Wojcik, S., "Noncontact Presence Sensors for Industrial Environments," *Sensors*, pp. 48-54, February, 1994.

Wood, T., "The Hall Effect Sensor," *Sensors*, pp. 27-36, March, 1986.

4
Triangulation Ranging

One of the first areas for concern in the evolution of a mobile robot design is the need to provide the system with sufficient situational awareness to support intelligent movement. The first step towards this end consists of the acquisition of appropriate information regarding ranges and bearings to nearby objects, and the subsequent interpretation of that data. Proximity sensors represent a first step in this direction, but by themselves fall short of the mark for a number of reasons previously discussed, not the least of which is the inability to quantify range.

Sensors that measure the actual distance to a target of interest with no direct physical contact can be referred to as non-contact ranging sensors. There are at least seven different types of ranging techniques employed in various implementations of such distance measuring devices (Everett, et al., 1992):

- Triangulation.
- Time of flight (pulsed).
- Phase-shift measurement (CW).
- Frequency modulation (CW).
- Interferometry.
- Swept focus.
- Return signal intensity.

Furthermore, there are a number of different variations on the theme for several of these techniques, as for example in the case of triangulation ranging:

- Stereo disparity.
- Single-point active triangulation.
- Structured light.
- Known target size.
- Optical flow.

Non-contact ranging sensors can be broadly classified as either *active* (radiating some form of energy into the field of regard) or *passive* (relying on energy emitted by the various objects in the scene under surveillance). The commonly used terms *radar* (radio direction and ranging), *sonar* (sound navigation and ranging), and *lidar* (light direction and ranging) refer to *active* methodologies that can be based on any of several of the above ranging techniques. For example, *radar* is usually implemented using time-of-flight,

phase-shift measurement, or frequency modulation. *Sonar* typically is based on time-of-flight ranging, since the speed of sound is slow enough to be easily measured with fairly inexpensive electronics. *Lidar* generally refers to laser-based schemes using time-of-flight or phase-shift measurement.

For any such active (reflective) sensors, effective detection range is dependent not only on emitted power levels, but also the following target characteristics:

- *Cross-sectional area* — Determines how much of the emitted energy strikes the target.
- *Reflectivity* — Determines how much of the incident energy is reflected versus absorbed or passed through.
- *Directivity* — Determines how the reflected energy is redistributed (i.e., scattered versus focused).

Triangulation ranging is based upon an important premise of plane trigonometry that states given the length of a side and two angles of a triangle, it is possible to determine the length of the other sides and the remaining angle. The basic *Law of Sines* can be rearranged as shown below to represent the length of side B as a function of side A and the angles θ and ϕ:

$$B = A\frac{\sin\theta}{\sin\alpha} = A\frac{\sin\theta}{\sin(\theta+\phi)}.$$

In ranging applications, length B would be the desired distance to the object of interest at point P_3 (Figure 4-1) for known sensor separation baseline A.

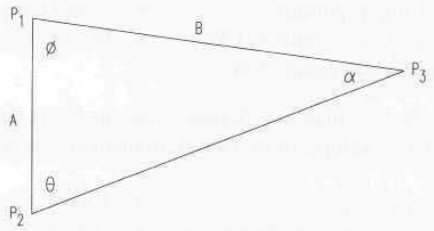

Figure 4-1. Triangulation ranging systems determine range B to target point P_3 by measuring angles ϕ and θ at points P_1 and P_2.

Triangulation ranging systems are classified as either *passive* (use only the ambient light of the scene) or *active* (use an energy source to illuminate the target). Passive stereoscopic ranging systems position directional detectors (video cameras, solid-state imaging arrays, or position sensitive detectors) at positions corresponding to locations P_1 and P_2 (Figure 4-2). Both imaging sensors are arranged to view the same object point, P_3 forming an imaginary triangle. The measurement of angles θ and ϕ in conjunction with the known orientation and

lateral separation of the cameras allows the calculation of range to the object of interest.

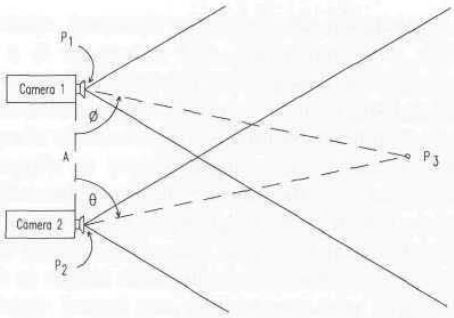

Figure 4-2. Passive stereoscopic ranging system configuration.

Active triangulation systems, on the other hand, position a controlled light source (such as a laser) at either point P_1 or P_2, directed at the observed point P_3. A directional imaging sensor is placed at the remaining triangle vertex and is also aimed at P_3. Illumination from the source will be reflected by the target, with a portion of the returned energy falling on the detector. The lateral position of the spot as seen by the detector provides a quantitative measure of the unknown angle ϕ, permitting range determination by the *Law of Sines*.

The performance characteristics of triangulation systems are to some extent dependent on whether the system is active or passive. Passive triangulation systems using conventional video cameras require special ambient lighting conditions that must be artificially provided if the environment is too dark. Furthermore, these systems suffer from a correspondence problem resulting from the difficulty in matching points viewed by one image sensor with those viewed by the other. On the other hand, active triangulation techniques employing only a single detector do not require special ambient lighting, nor do they suffer from the correspondence problem. Active systems, however, can encounter instances of no recorded strike because of specular reflectance or surface absorption of the light.

Limiting factors common to all triangulation sensors include reduced accuracy with increasing range, angular measurement errors, and a *missing parts* (also known as *shadowing*) problem. *Missing parts* refers to the scenario where particular portions of a scene can be observed by only one viewing location (P_1 or P_2). This situation arises because of the offset distance between P_1 and P_2, causing partial occlusion of the target (i.e., a point of interest is seen in one view but otherwise occluded or not present in the other). The design of triangulation systems must include a tradeoff analysis of the offset: as this baseline measurement increases, the range accuracy increases, but problems due to directional occlusion worsen.

4.1 Stereo Disparity

The first of the triangulation schemes to be discussed, *stereo disparity*, (also called *stereo vision*, *binocular vision*, and *stereopsis*) is a passive ranging technique modeled after the biological counterpart. When a three-dimensional object is viewed from two locations on a plane normal to the direction of vision, the image as observed from one position is shifted laterally when viewed from the other. This displacement of the image, known as *disparity*, is inversely proportional to the distance to the object. Humans subconsciously *verge* their eyes to bring objects of interest into rough registration (Burt, et al., 1992). Hold up a finger a few inches away from your face while focusing on a distant object and you can simultaneously observe two displaced images in the near field. In refocusing on the finger, your eyes actually turn inward slightly to where their respective optical axes converge at the finger instead of infinity.

Most robotic implementations use a pair of identical video cameras (or a single camera with the ability to move laterally) to generate the two disparity images required for stereoscopic ranging. The cameras are typically aimed straight ahead viewing approximately the same scene, but (in simplistic cases anyway) do not possess the capability to *verge* their center of vision on an observed point as can human eyes. This limitation makes placement of the cameras somewhat critical because stereo ranging can take place only in the region where the fields of view overlap. In practice, analysis is performed over a selected range of disparities along the *Z* axis on either side of a perpendicular plane of zero disparity called the *horopter* (Figure 4-3). The selected image region in conjunction with this disparity range defines a three-dimensional volume in front of the vehicle known as the *stereo observation window* (Burt, et al., 1993).

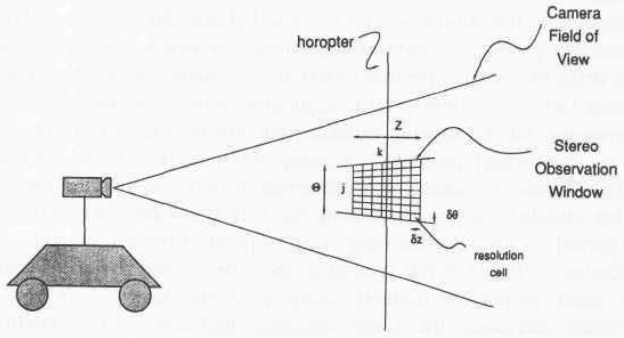

Figure 4-3. The *stereo observation window* is that volume of interest on either side of the plane of zero disparity known as the *horopter* (courtesy David Sarnoff Research Center).

More recently there has evolved a strong interest within the research community for dynamically reconfigurable camera orientation (Figure 4-4), often termed *active vision* in the literature (Aloimonos, et al., 1987; Swain & Stricker, 1991; Wavering, et al., 1993). The widespread acceptance of this terminology is perhaps somewhat unfortunate in view of potential confusion with stereoscopic systems employing an active illumination source (see Section 4.1.3). *Verging stereo*, another term in use, is perhaps a more appropriate choice. *Mechanical verging* is defined as the process of rotating one or both cameras about the vertical axis in order to achieve zero disparity at some selected point in the scene (Burt, et al., 1992).

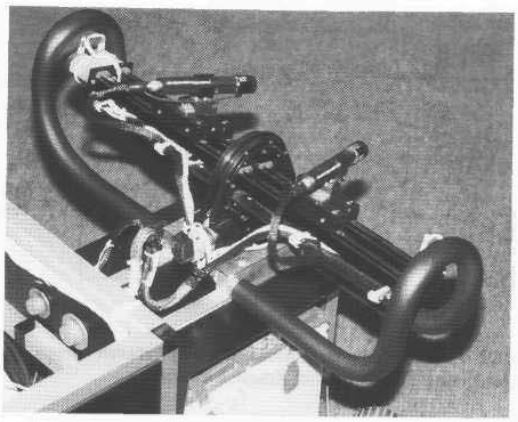

Figure 4-4. This stereoscopic camera mount uses a pair of lead-screw actuators to provide reconfigurable baseline separation and vergence as required (courtesy Robotic Systems Technology, Inc.).

There are four basic steps involved in the stereo ranging process (Poggio, 1984):

- A point in the image of one camera must be identified (Figure 4-5, left).
- The same point must be located in the image of the other camera (Figure 4-5, right).
- The lateral positions of both points must be measured with respect to a common reference.
- Range Z is then calculated from the disparity in the lateral measurements.

On the surface this procedure appears rather straightforward, but difficulties arise in practice when attempting to locate the specified point in the second image

(Figure 4-5). The usual approach is to match "interest points" characterized by large intensity discontinuities (Conrad & Sampson, 1990). Matching is complicated in regions where the intensity and/or color are uniform (Jarvis, 1983b). Additional factors include the presence of shadows in only one image (due to occlusion) and the variation in image characteristics that can arise from viewing environmental lighting effects from different angles. The effort to match the two images of the point is called *correspondence*, and methods for minimizing this computationally expensive procedure are widely discussed in the literature (Nitzan, 1981; Jarvis, 1983a; Poggio, 1984; Loewenstein, 1984; Vuylsteke, et al., 1990; Wildes, 1991).

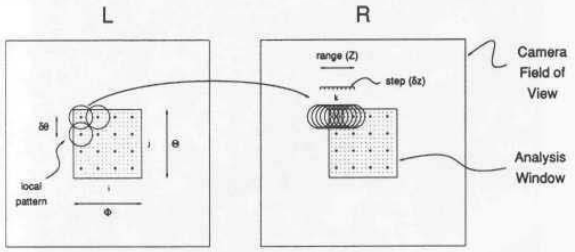

Figure 4-5. Range Z is derived from the measured disparity between interest points in the left and right camera images (courtesy David Sarnoff Research Center).

Probably the most basic simplification employed in addressing the otherwise overwhelming *correspondence* problem is seen in the *epipolar restriction* that reduces the two-dimensional search domain to a single dimension (Vuylsteke, et al., 1990). The *epipolar surface* is a plane defined by the point of interest P and the positions of the left and right camera lenses at L and R as shown in Figure 4-6. The intersection of this plane with the left image plane defines the *left epipolar line* as shown. As can be seen from the diagram, since the point of interest P lies in the *epipolar plane*, its imaged point P_l must lie somewhere along the *left epipolar line*. The same logic dictates the imaged point P_r must lie along a similar *right epipolar line* within the right image plane. By carefully aligning the camera image planes such that the *epipolar lines* coincide with identical scan lines in their respective video images, the correspondence search in the second image is constrained to the same horizontal scan line containing the point of interest in the first image. This effect can also be achieved with non-aligned cameras by careful calibration and rectification (resampling), as is done in real time by JPL's stereo vision system (see below) using a Datacube *Miniwarper* module.

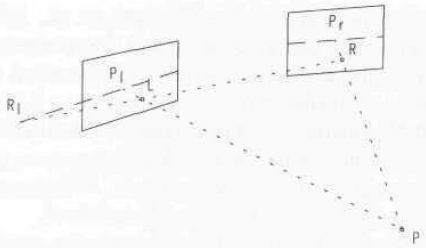

Figure 4-6. The *epipolar surface* is a plane defined by the lens centerpoints *L* and R and the object of interest at *P* (adapted from Vuylsteke, et al., 1990).

To reduce the image processing burden, most correspondence schemes monitor the overall scene at relatively low resolution and examine only selected areas in greater detail. A *foveal representation* analogous to the acuity distribution in human vision is generally employed as illustrated in Figure 4-1, allowing an extended field-of-view without loss of resolution or increased computational costs (Burt, et al., 1993). The high-resolution *fovea* must be shifted from frame to frame in order to examine different regions of interest individually. Depth acuity is greatest for small disparities near the horopter and falls off rapidly with increasing disparities (Burt, et al., 1992).

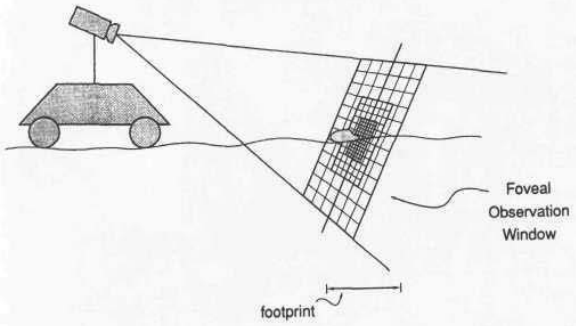

Figure 4-7. The *foveal* stereo representation provides high acuity near the center of the *observation window*, with decreasing resolution towards the periphery (courtesy David Sarnoff Research Center).

4.1.1 JPL Stereo Vision

The Jet Propulsion Laboratory (JPL), Pasadena, CA, is developing a passive stereo vision system for use on board the NASA Planetary Rover and for US

Army robotic land vehicle applications (Bedard, et al., 1991a, 1991b; Slack, 1989). In 1990, JPL developed a vision system that computed Laplacian image pyramids using Datacube hardware, followed by a method of stereo matching which applies a sum-of-squared-differences operator to 8-bit greyscale images. Originally, the sum-of-squared-differences operation was performed at the 64- by 60-pixel image level of the pyramid using a *68020* processor, producing range and confidence images in approximately two seconds. Subsequent implementations perform the correlation at much higher speeds (see below).

An alternate version of the algorithm augments the cross-correlation with a one-dimensional smooth-surface model, allowing interpolation over textureless image areas. Disparity estimates are performed independent of each scan line, requiring approximately six seconds per 64- by 60-pixel image-pair. This system has been implemented on the *Planetary Rover Navigation Testbed* vehicle (Figure 4-8) and performed reliably in off-road navigation tests. Both algorithms assume that the cameras are well aligned, confining the matching search to corresponding scan lines of the two images.

Figure 4-8. NASA Planetary Rover navigation testbed (courtesy Jet Propulsion Laboratory).

The US Army Tank Automotive Command is applying this technology for obstacle detection and reflexive obstacle avoidance within the context of computer-aided remote driving of a HMMWV. Disparity field estimation at 7.5 frames per second has been achieved from the 64- by 60-pixel level of Laplacian image pyramids, using a *Datacube MaxVideo-20* board and a 68040 host processor. Obstacle detection is performed at the rate of three frames per second

with postprocessing, triangulation, and a very simple detection algorithm (Matthies, 1992a, 1992b).

This system was demonstrated at the US Army *Demo I* at Aberdeen, MD, in April/May of 1992. The vehicle successfully detected obstacles of about 50 centimeters on a side while driving at several kilometers per hour on gravel roads. Continued development of the system is taking place under the *Unmanned Ground Vehicle (UGV) Demo II* program sponsored by the Advanced Research Projects Agency (ARPA). Under this program, the need for precise camera alignment has been eliminated by performing real-time image resampling before computing image pyramids, greatly simplifying implementation. The system was used to detect obstacles on relatively smooth off-road terrain during the UGV *Demo B* in June, 1994 (Figure 4-9), using the 128- by 120-level of the Laplacian pyramid. Higher speeds, higher resolution, and rougher terrain are anticipated for *Demo C* in June 1995 and *Demo II* in June 1996.

Figure 4-9. The JPL stereo vision system was used to detect obstacles for the HMMWV-based *Surrogate Semiautonomous Vehicle (SSV)* at *Demo B* in June 1994 (courtesy Martin Marietta Denver Aerospace).

4.1.2 David Sarnoff Stereo Vision

Conventional application of stereoscopic ranging to mobile robot collision avoidance generally involves creating a dense range map over an appropriate field of view dictated in size by the vehicle dynamics (Chapter 1). Sufficient resolution must be provided to detect small hazards at distances typically 10 to 20 meters

ahead of the vehicle. From a practical standpoint, this combination of high-resolution processing over a large field of regard is computationally intensive, resulting in low throughput rates and expensive hardware (Burt, et al., 1993).

The Advanced Image Processing Research Group at David Sarnoff Research Center, Princeton, NJ, is developing a specialized image processing device called the *vision front end (VFE).* This dedicated hardware performs image preprocessing functions faster and more efficiently than a general purpose computer, and thus opens the door for more practical solutions in keeping with the needs of a mobile robotic system. The *VFE* concept is characterized by four innovative features:

- Laplacian pyramid processing (Burt & Adelson, 1983; Anderson, et al., 1985).
- Electronic vergence (Burt, et al., 1992; 1993).
- Controlled horopter (Burt, et al., 1992; 1993).
- Image stabilization (Burt & Anandan, 1994; Hansen, et al., 1994).

The Sarnoff *VFE* approach emulates the *vergence* and *foveal organization* attributes of human vision through electronic warping and local disparity estimation within a pyramid data structure, thus providing appropriate resolution where required, but at lower cost. This approach is algorithmically accomplished as follows (Burt, et al., 1992):

- The right image is warped to bring it into alignment with the left image within a designated region of analysis (Figure 4-10).
- Residual stereo disparity between the partially aligned images is then estimated.
- Global displacement is used to refine the alignment.
- The global displacement and local disparity field are passed to the main vision computer.

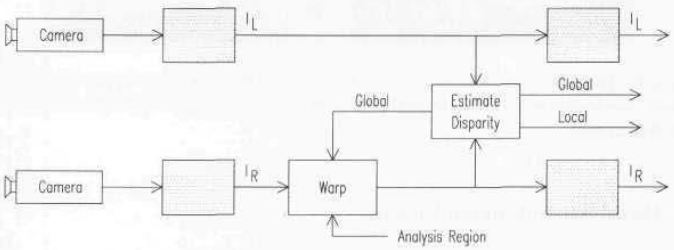

Figure 4-10. After warping the right image into alignment with the left, global alignment (electronic vergence) and local disparity estimations are passed to the main vision processor (adapted from Burt, et al., 1992).

Mechanical vergence of the stereo camera pair results in a horopter oriented perpendicular to the system optical axis as shown earlier in Figure 4-3. *Electronic vergence* is used by the *VFE* to dynamically warp images such that the horopter is tilted to provide optimal stereo acuity for a particular vision task (Burt, et al., 1992). This *controlled horopter* approach thus goes a step beyond the flexibility of interactive mechanical vergence, in that the orientation of the horopter can be varied in addition to its stand-off distance. For example, Figure 4-11 shows a situation where the horopter is made coincident with the ground plane. When *foveal stereo* is employed in conjunction with the tilted horopter technique, maximum sensitivity to small topographical features can be achieved due to the increased clustering of high-resolution stereo cells along the ground surface (Burt, et al., 1993). The ability to detect low-lying obstacles or potholes in the path of the vehicle is subsequently greatly enhanced.

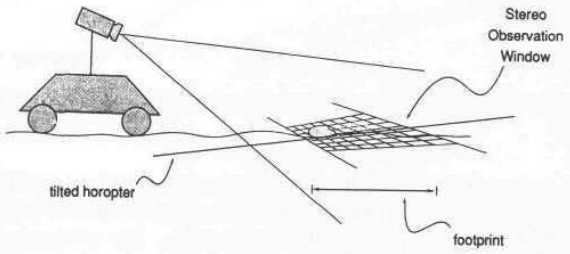

Figure 4-11. Through electronic warping of both images, the plane of zero disparity (horopter) can be made coincident with the ground surface for enhanced acuity in the region of most interest (courtesy David Sarnoff Research Center).

A fundamental challenge to employing any image-based system in a collision avoidance role is the inherent jitter introduced by vehicle pitch and roll. Effective image stabilization has proven to be a critical factor in successful implementation of vehicle-based stereo ranging capabilities (Burt & Anandan, 1994). Mechanically stabilized optics have been used with good results in aerial photography and for filming sporting events, but are very expensive and rather bulky, which limits their utility from a robotics perspective. Low-end electronic-stabilization techniques have recently been introduced into some consumer camcorders (Uomori, et al., 1990) but are generally limited to a small amount of translational compensation only. Using pyramid-based motion estimation and electronic warping, the Sarnoff *VFE* provides real-time removal of first-order deformations between sequential images, and can assemble aligned components over time to produce a *scene mosaic* (Hansen, et al., 1994).

4.2 Active Triangulation

Rangefinding by *active triangulation* is a variation on the *stereo disparity* method of distance measurement. In place of one camera is a laser (or LED) light source aimed at the surface of the object of interest. The remaining camera is offset from this source by a known distance *A* and configured to hold the illuminated spot within its field of view (Figure 4-12).

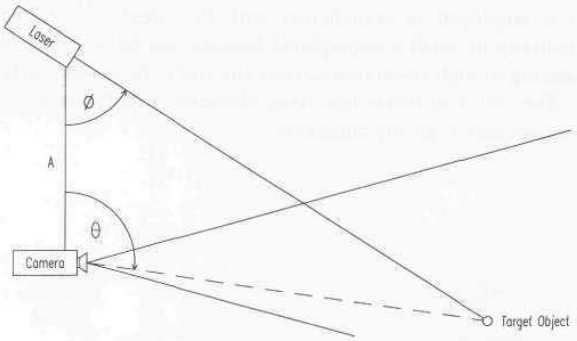

Figure 4-12. An *active triangulation-ranging configuration* employing a conventional CCD array as the detector.

For one- or two-dimensional array detectors such as vidicon or CCD cameras, the range can be determined from the known baseline distance *A* and the relative position of the laser-spot image on the image plane. For mechanically scanned single-element detectors such as photodiodes or phototransistors, the rotational angles of the detector and/or source are measured at the exact instant the detector observes the illuminated spot. The trigonometric relationships between these angles and the baseline separation are used (in theory) to compute the distance. To obtain three-dimensional information for a volumetric region of interest, laser triangulators can be scanned in both azimuth and elevation. In systems where the source and detector are self-contained components, the entire configuration can be moved mechanically as illustrated in Figure 4-13. In systems with movable optics, the mirrors and lenses are generally scanned in synchronization while the laser and detector remain stationary.

In practice, the actual baseline separation distance *A* as well as the angles θ and ϕ are difficult to measure with any precision, and therefore most designers simply calibrate the ranging system with test targets placed at known distances along the *Z* axis. Nguyen and Blackburn (*1995*) present a typical procedure illustrated in Figure 4-14 below. The line *uP* passing through the lens focal point *O* can be represented by:

$$y = \frac{u}{f} z$$

where:

y = height above Z axis
u = vertical projection of point P on the image plane
f = focal length of the lens,

while the laser path is similarly of the form: $y = mz + c$. Combining these equations and simplifying eventually yields the desired expression for range z along the camera optical axis (Nguyen & Blackburn, 1995):

$$z = \frac{N}{ud - k}$$

where N, d, and k are obtained from the calibration setup as follows:

$$N = (u_1 - u_2)z_1 z_2$$
$$d = z_2 - z_1$$
$$k = u_2 z_2 - u_1 z_1$$

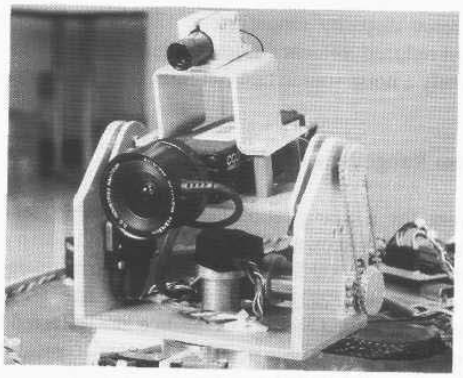

Figure 4-13. A 5-milliwatt laser source used in conjunction with a CCD camera is mounted on a 2-DOF pan and tilt mechanism on the ModBot research prototype (courtesy Naval Command Control and Ocean Surveillance Center).

In other words, calibration targets are placed at distances z_1 and z_2 from the camera, and their associated offsets u_1 and u_2 (i.e., where the laser spot is

observed striking the targets in the image plane) used to calculate d, k, and N, yielding a general expression for range z as a function of pixel offset u. Note this calibration approach does not require any information regarding the baseline separation distance A or lens focal length f.

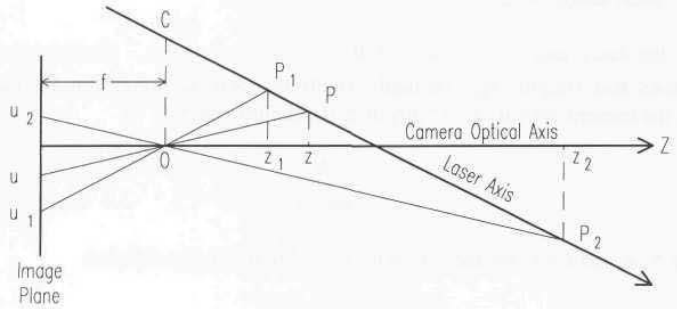

Figure 4-14. Calibration targets are placed at known distances z_1 and z_2 to derive a general expression for range z as a function of image displacement u (adapted from Nguyen & Blackburn, 1995).

Drawbacks to active triangulation include the *missing parts* situation, where points illuminated by the light source cannot be seen by the camera and vice versa (Jarvis, 1983b), as well as surface absorption or specular reflection of the irradiating energy (see Chapter 9). On the positive side, however, point-source illumination of the image effectively eliminates the correspondence problem encountered in stereo disparity rangefinders. There is also no dependence on scene contrast, and reduced influence from ambient lighting effects. (Background lighting is effectively a noise source that can limit range resolution.)

4.2.1 Hamamatsu Rangefinder Chip Set

The block diagram for a triangulation rangefinding chip set manufactured by Hamamatsu Corporation is shown in Figure 4-15. This 16-step rangefinder offers a maximum sample rate of 700 Hz and consists of three related components: a *position sensitive detector (PSD)*, a *rangefinder IC*, and an *LED light source*. Near-infrared energy is emitted by the LED source and reflected by the target back to the PSD, a continuous light-spot position detector (basically a light-sensitive diode combined with a distributed resistance). A small injected current flows from the center to both ends of the detector element with a distribution determined by the footprint of illumination; the ratio of the respective current flows can be used to determine the location of the spot centroid (Vuylsteke, et al., 1990). The sensitive receiver circuitry is capable of detecting pulsed light returns generating as little as 1 nanoamp of output current in the PSD.

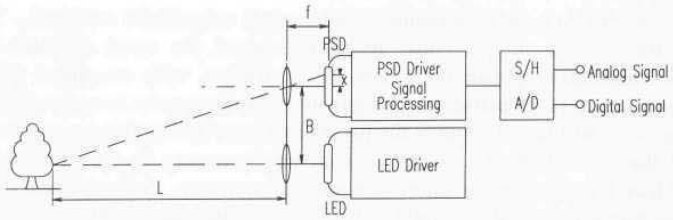

Figure 4-15. Block diagram of the Hamamatsu triangulation rangefinding chip set (courtesy Hamamatsu Corp.).

The Hamamatsu rangefinder chip operates from a 3-volt DC supply and provides both analog and digital signal outputs. The 0.24-to-0.46-volt analog output is produced by a sample-and-hold circuit, while the digital output is determined by an integral A/D converter with 4-bit resolution corresponding to 16 discrete range zones (Hamamatsu, 1990).

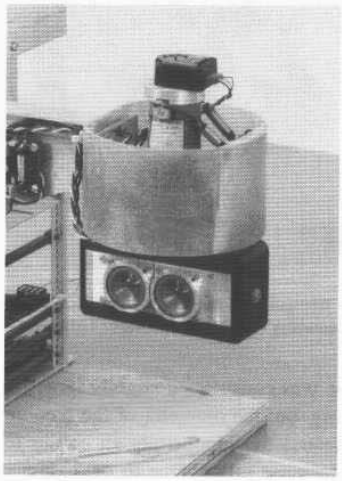

Figure 4-16. The active triangulation ranging system employed on ROBART III is based on the Hamamatsu chip set (courtesy Naval Command Control and Ocean Surveillance Center).

4.2.2 Draper Laboratory Rangefinder

A team of MIT students at the Charles Stark Draper Laboratory has recently designed and built a small (5 kilogram) autonomous microrover for exploration of the Martian surface (Malafeew & Kaliardos, 1994). In the process, the need for a

compact, short-range, and inexpensive non-contact rangefinder emerged. The limited energy and computational resources aboard the rover dictated that potential candidates operate on a low power budget, with an output signal supporting simple range extraction. Simplicity in the electronics was also desired, since the rover will have to endure the harsh environments found in space. It was decided that an 180-degree azimuthal scan was necessary in the direction of forward travel, but that an elevation scan was not necessary. A five-percent range error was deemed acceptable in light of the inherent navigational errors associated with dead reckoning. From these requirements, an active triangulation rangefinder was developed using a near-infrared laser source and a one-dimensional *position-sensitive detector* (Figure 4-17).

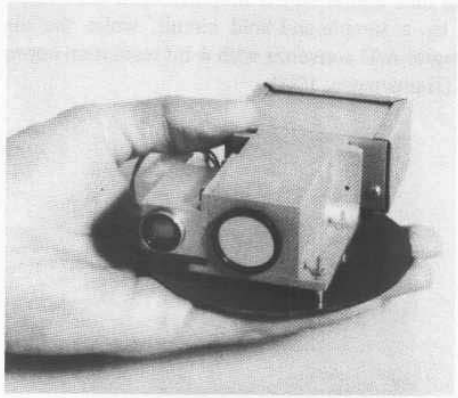

Figure 4-17. This active triangulation ranging system uses a 500-milliwatt near-infrared laser diode as the active source (courtesy Charles Stark Draper Laboratory).

The initial prototype was constructed slightly larger than necessary to simplify mounting and machining, but the diameter of the receiving lens was intentionally kept small (15 millimeters) to demonstrate an ability to collect returned energy with sufficient signal-to-noise ratio. Due to developmental time constraints, the electronics employed on the prototype are typical of those routinely suggested for DC operation of a standard *position-sensitive detector* circuit, hence this rangefinder is very similar in concept to the previously described Hamamatsu system. Signal currents from the detector are read immediately before and during the firing of the active source, a common method for subtracting off ambient background noise. Due to the slow vehicle speed, there is no need for an extremely fast ranging system, and a 25-Hz sampling rate should suffice.

The large amount of electronic noise associated with the rest of the rover systems combined with the small-diameter receiving lens made detection of weak signals difficult, requiring a relatively high-power (>250 milliwatts) illumination

source. The source also needed to be well collimated, since triangulation systems work best when the footprint of illumination is small. To meet these needs, a 920-nanometer laser diode with a beam divergence of under 15 milliradians was selected. The laser provides an optical power output of about 500 milliwatts for 1-millisecond intervals. This power level is not eye-safe, of course, but that is of little concern on Mars.

With a matched interference filter, the rangefinder is able to operate under direct sunlight conditions. Initial test results show a ranging accuracy that is about five percent at the maximum range of 3 meters. As with any triangulation system, this normalized accuracy improves as the range is decreased. Azimuthal scanning on the rover is currently accomplished by servoing the entire rangefinder unit through 180-degree sweeps.

4.2.3 Quantic Ranging System

A novel LED-based triangulation ranging system was developed for the Navy by Quantic Industries, Inc. under the Small Business Innovative Research (SBIR) Program (Moser & Everett, 1989). The prototype unit shown in Figure 4-18 was specifically designed for use on a mobile robotic platform, under the following general guidelines:

- Coverage of 100-degrees azimuth and 30-degrees elevation.
- No moving parts.
- 10-Hz update rate.
- Real-time range measurements out to 20 feet.
- Minimal power consumption.
- Small size and weight.

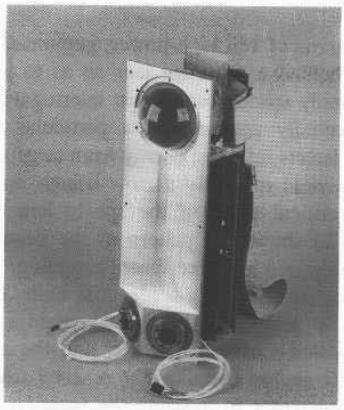

Figure 4-18. Prototype triangulation ranging sensor built by Quantic Industries, Inc. (courtesy Naval Command Control and Ocean Surveillance Center).

Active triangulation ranging is employed with about 5-degree spatial resolution over a nominal field of regard of 100 degrees in azimuth and 30 degrees in elevation. Under typical indoor conditions, fairly accurate target detection and range measurements are obtained to about 24 feet in the dark and about 15 feet under daylight conditions. No mechanical scanning is employed, and the protected envelope can be covered in 0.1 to 1 second, depending upon the required accuracy.

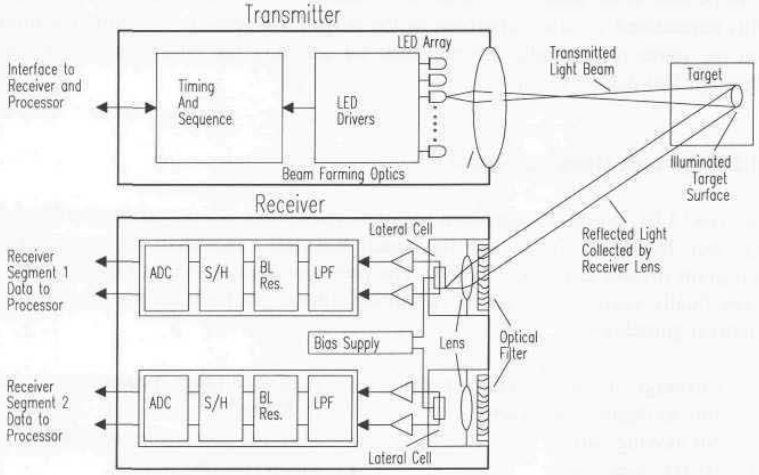

Figure 4-19. Block diagram of Quantic sequential-array triangulation ranging system.

The transmitter consists of 164 high-power, gallium-aluminum-arsenide LEDs mounted in an array behind a spherical lens so as to produce a corresponding number of narrow, evenly spaced beams that interrogate the volume of interest. The LEDs are sequentially activated at a particular repetition rate while a synchronous receiver detects reflected energy from targets within its field of view. The self-lensed LEDs yield relatively narrow beams, so most of their power is projected within the critical angle of the sphere lens for high power-transfer efficiency. Figure 4-20 shows the pattern of the beams and their positioning behind the lens for the desired 5-degree spatial sampling.

The optical receiver consists of two identical units, each covering a field of view of about 50 by 50 degrees. Both units contain a Fresnel lens, an optical bandpass filter, a position-sensitive detector, and the associated electronics to process and digitize the analog signals. The receiver uses a silicon lateral-effect position-sensing photodetector to measure the location (in the image plane) of transmitted light reflected (scattered) from a target surface. The transmitter and receiver are vertically separated by a 10-inch baseline.

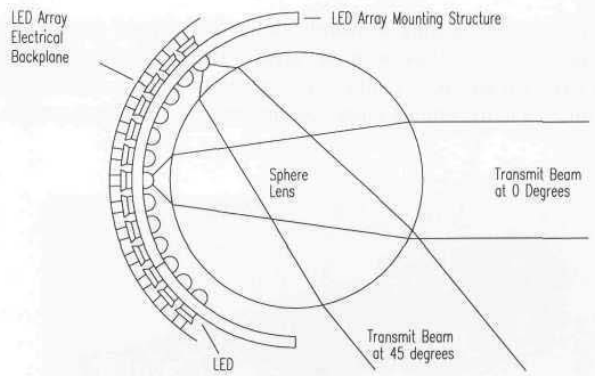

Figure 4-20. Arrangement of near-infrared LED array behind spherical lens in the Quantic ranging system.

The location of the centroid of reflected energy focused on the position-sensing detector is a function of the particular beam that is active and the range to the target being illuminated by that beam. The position signals from the detector (resulting from the sequential activation of LEDs in the transmitter) are collectively processed by a dedicated microcomputer to determine the ranges to targets throughout the sensor's detection envelope. Target azimuth and elevation are a function of the position of the LED (in the transmitter array) active at the time of detection. A look-up table derived from calibration data is used to perform the position-to-range conversions and to compensate for receiver non-uniformities.

4.3 Active Stereoscopic

Due to the computationally intensive complexities and associated resources required for establishing correspondence, passive stereoscopic methods were initially limited in practical embodiments to very simple scenes (Blais, et al., 1988). One way around these problems is to employ an active source in conjunction with a pair of stereo cameras. This active illumination greatly improves system performance when viewing scenes with limited contrast. Identification of the light spot becomes a trivial matter; a video frame representing a scene illuminated by the source is subtracted from a subsequent frame of the same image with the light source deactivated. Simple thresholding of the resultant difference image quickly isolates the region of active illumination. This process is performed in rapid sequence for both cameras, and the lateral displacement of the centroid of the spot is then determined.

Such an active stereoscopic vision system was initially employed on ROBART II for ranging purposes (Figure 4-21). A 6-volt incandescent source was pulsed at

about a 10-Hz rate, projecting a sharply defined V-shaped pattern across the intersection of the camera plane with the target surface. The incandescent source was chosen over a laser-diode emitter because of simplicity, significantly lower cost (at the time), and the limited range requirements for an indoor system.

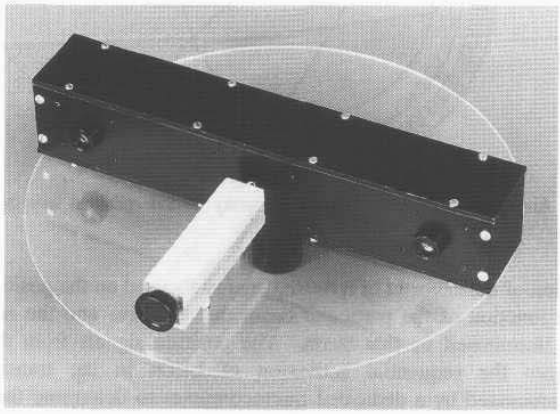

Figure 4-21. The active stereoscopic ranging system employed on ROBART II used a pair of linear CCD arrays in conjunction with an incandescent structured-light source (center).

The configuration did not represent a true three-dimensional capability in that each of the cameras consisted of a horizontal linear (as opposed to two-dimensional) CCD array. (Linear arrays were employed in order to keep the image processing requirements realistic with respect to the available 8-bit computational hardware on board.) The twin cameras provided no vertical resolution, but furnished range and bearing information on interest points detected in the horizontal plane coincident with their respective optical axes. This limitation was consistent with the two-dimensional simplified world model employed by the robot; objects were represented by their projection on the X-Y plane, and height information was not taken into account. The linear cameras were removed in 1987 and replaced with a single two-dimensional high-resolution CCD camera coupled to a line-oriented video digitizer.

4.3.1 HERMIES

Alignment between the source and cameras is not critical in active stereoscopic ranging systems; in fact, the source does not even have to be located on board the robot. For example, Kilough and Hamel (1989) describe two innovative

configurations using external sources for use with the robot HERMIES IIB, built at Oak Ridge National Laboratory. A pair of wide-angle black-and-white CCD cameras are mounted on a pan-and-tilt mechanism atop the robot's head as shown in Figure 4-22. Analog video outputs from the cameras are digitized by a frame grabber into a pair of 512- by 384-pixel arrays, with offboard image processing performed by a *Hypercube* at a scaled-down resolution of 256 by 256. The initial application of the vision system was to provide control of a pair of robotic arms (from the Heathkit *HERO-1* robot) employed on HERMIES.

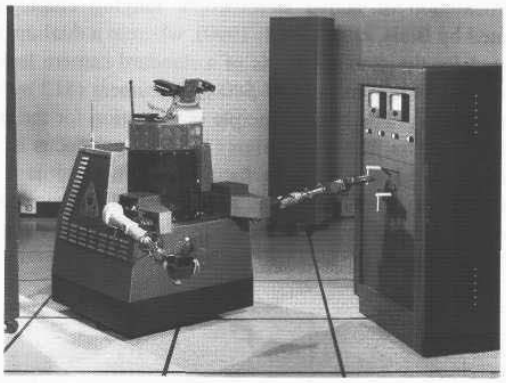

Figure 4-22. HERMIES IIB employed an active stereo ranging system with an external laser source that could be used to designate objects of interest in the video image (courtesy Oak Ridge National Laboratory).

To accomplish this task, a near-infrared LED is attached to the end of the HERO-1 arm near the manipulator and oriented so as to be visible within the field of view of the stereo camera pair. A sequence of images is then taken by each camera, with the LED first *on* and then *off*. The *off* representations are subtracted from the *on* representations, leaving a pair of difference images, each comprised of a single bright dot representing the location of the LED. The centroids of the dots are calculated to precisely determine their respective coordinates in the difference-image arrays. A range vector to the LED can then be easily calculated, based on the lateral separation of the dots as perceived by the two cameras. This technique establishes the actual location of the manipulator in the reference frame of the robot. Experimental results indicated a 2-inch accuracy with a 0.2-inch repeatability at a distance of approximately 2 feet (Kilough and Hamel, 1989).

A near-infrared solid-state laser mounted on a remote tripod was then used by the operator to designate a target of interest within the video image of one of the cameras. The same technique described above was repeated, only this time the imaging system toggled the laser power *on* and *off*. A subsequent differencing

operation enabled calculation of a range vector to the target, also in the robot's reference frame. The difference in location of the gripper and the target object could then be used to effect both platform and arm motion. The imaging processes would alternate in near-real-time for the gripper and the target, enabling the HERMIES robot to drive over and grasp a randomly designated object under continuous closed-loop control.

4.3.2 Dual-Aperture 3-D Range Sensor

A novel implementation of active stereoscopic ranging employing only one camera is presented by Blais, et al. (1988; 1990), wherein a dual-aperture pin-hole mask is substituted for the diaphragm iris of a standard camera lens as shown in Figure 4-23 below. A Pulnix model *TM-540* CCD camera (512 by 492 pixels) is employed as the detector. The basic principle of operation for the *BIRIS* (i.e., bi-iris) system is described by Rioux and Blais (1986). Lens focus is adjusted such that a point located at position *A* is in focus at *A'* in the image plane of the detector; ignoring the mask for a moment, any ray traveling from point *A* through the lens will arrive at the image point *A'*. Under these conditions, a second point *B* at a further distance *z* from the lens will be imaged at *B'*.

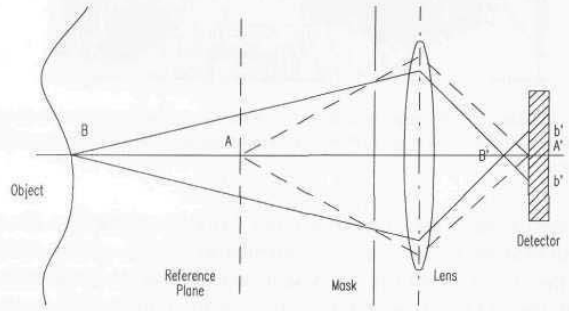

Figure 4-23. The dual-aperture pin-hole mask allows an active stereoscopic ranging capability to be implemented with a single CCD camera (adapted from Blais, et al., 1988).

With the mask inserted in front of the lens, two separate rays originating at point B will pass through the two apertures and be redirected by the lens to point *B'* in front of the detector. These two rays will continue on to strike the CCD array at points b_1 and b_2 as indicated in the figure. The lateral separation between points b_1 and b_2 is directly proportional to the range *Z* from the lens to point *B*. The *X* and *Y* displacement of the spots on the CCD array with respect to its center can be used to calculate the vector direction to the target with respect to the optical axis of the lens. The magnitude of this vector is of course the measured range *Z*.

Projecting a pattern of stripes (instead of a single spot of light) perpendicular to an imaginary line drawn between the two apertures in the mask enables acquisition of multiple range profiles from a single video frame (Rioux & Blais, 1986). Each projected stripe will be appear as a pair of lines on the detector. Similarly, the lateral separation between line pairs can be used to derive the range value *Z*. A 256- by 240-point range image can be acquired in under 4.3 seconds when a single stripe is projected; the same image will be acquired in approximately one second if four profiles are projected simultaneously (Blais, et al., 1988). Discontinuities in the imaged lines will be generated by objects illuminated by the structured pattern of light. This *structured-light* illumination technique will be described in more detail in the next section.

4.4 Structured Light

Ranging systems that employ *structured light* are a further refined case of active triangulation. A pattern of light (either a line, a series of spots, or a grid pattern) is projected onto the object surface while the camera observes the pattern from its offset vantage point. Range information manifests itself in the distortions visible in the projected pattern due to variations in the depth of the scene. The use of these special lighting effects tends to reduce the computational complexity and improve the reliability of three-dimensional object analysis (Jarvis, 1983b; Vuylsteke, et al., 1990). The technique is commonly used for rapid extraction of limited quantities of visual information of moving objects (Kent, 1985), and thus lends itself well to collision avoidance applications. Besl (1988) provides a good overview of *structured-light* illumination techniques, while Vuylsteke, et al. (1990) classify the various reported implementations according to the following characteristics:

- The number and type of sensors.
- The type of optics (i.e., spherical or cylindrical lens, mirrors, multiple apertures).
- The dimensionality of the illumination (i.e., point or line).
- Degrees of freedom associated with scanning mechanism (i.e., zero, one, or two).
- Whether or not the scan position is specified (i.e., the instantaneous scanning parameters are not needed if a redundant sensor arrangement is incorporated).

The most common *structured-light* configuration entails projecting a line of light onto a scene, originally introduced by P. Will and K. Pennington of IBM Research Division Headquarters, Yorktown Heights, NY (Schwartz, undated). Their system created a plane of light by passing a collimated incandescent source through a slit, thus projecting a line across the scene of interest. (More recent

systems create the same effect by passing a laser beam through a cylindrical lens or by rapidly scanning the beam in one dimension.) Where the line intersects an object, the camera view will show displacements in the light stripe that are proportional to the depth of the scene. In the example depicted in Figure 4-24, the lower the reflected illumination appears in the video image, the closer the target object is to the laser source. The exact relationship between stripe displacement and range is dependent on the length of the baseline between the source and the detector. Like any triangulation system, when the baseline separation increases, the accuracy of the sensor increases, but the *missing parts* problem worsens.

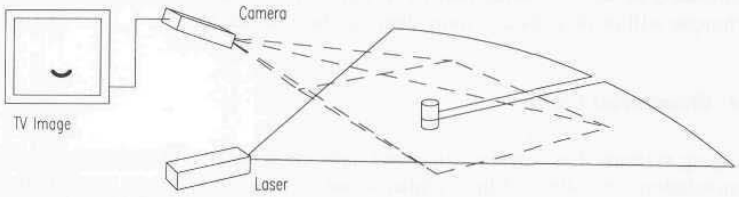

Figure 4-24. A common structured-light configuration used on robotic vehicles projects a horizontal line of illumination onto the scene of interest and detects any target reflections in the image of a downward-looking CCD array.

Three-dimensional range information for an entire scene can be obtained in relatively simple fashion through striped lighting techniques. By assembling a series of closely spaced two-dimensional contours, a three-dimensional description of a region within the camera's field of view can be constructed. The third dimension is typically provided by scanning the laser plane across the scene. Compared to single-point triangulation, striped lighting generally requires less time to digitize a surface, with fewer moving parts because of the need to mechanically scan only in one direction. The drawback to this concept is that range extraction is time consuming and difficult due to the necessity of storing and analyzing many frames.

An alternative structured-light approach for three-dimensional applications involves projecting a rectangular grid of high-contrast light points or lines onto a surface. Variations in depth cause the grid pattern to distort, providing a means for range extraction. The extent of the distortion is ascertained by comparing the displaced grid with the original projected patterns as follows (LeMoigue & Waxman, 1984):

- Identify the intersection points of the distorted grid image.
- Label these intersections according to the coordinate system established for the projected pattern.
- Compute the disparities between the intersection points and/or lines of the two grids.
- Convert the displacements to range information.

The comparison process requires correspondence between points on the image and the original pattern, which can be troublesome. By correlating the image grid points to the projected grid points, this problem can be somewhat alleviated. A critical design parameter is the thickness of the lines that make up the grid and the spacing between these lines. Excessively thin lines will break up in busy scenes, causing discontinuities that adversely affect the intersection points labeling process. Thicker lines will produce less observed grid distortion resulting in reduced range accuracy (LeMoigue & Waxman, 1984). The sensor's intended domain of operation will determine the density of points required for adequate scene interpretation and resolution.

4.4.1 TRC Strobed-Light Triangulation System

Transitions Research Corporation (TRC), Danbury, CN, has incorporated a structured light system to detect and measure the position of objects lying within or adjacent to the forward path of their *HelpMate* mobile platform (Evans, et al., 1990; King, 1990). The TRC system (Figure 4-25) is comprised of a CCD camera and two 700-nanometer near-infrared strobes. The strobes alternately fire with a low (3 Hz) duty cycle, resulting in a 300-millisecond update rate. A bandpass filter is employed at the camera end to enhance the received signal-to-noise ratio, thereby minimizing noise contributions from outside the near-infrared spectrum. By performing a pixel-by-pixel subtraction of a non-flashed image from a flashed image, that portion of the scene resulting from reflected energy is emphasized.

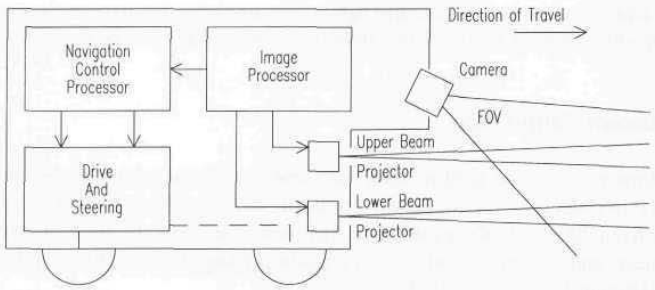

Figure 4-25. Block diagram of the TRC *Strobed Light Triangulation System* installed on the company's *HelpMate* mobile platform (courtesy Transitions Research Corp.).

The reflected light planes are viewed across the horizontal pixel lines of the camera. An object approaching the mobile platform first appears at the top of the field-of-view and then moves down the image plane as the distance closes. In this way, each pixel in the image plane corresponds to a predetermined range and bearing derived through simple triangulation. To ensure real-time computation,

TRC has implemented a thresholding algorithm that uses every sixth pixel in an image of 512 by 480 pixels. Effective range of the system is out to 6 feet with a resolution of 1 to 3 inches, and an angular resolution of 2 degrees. Power consumption (including the frame grabber, camera, AT computer, and strobes) is around 40 watts.

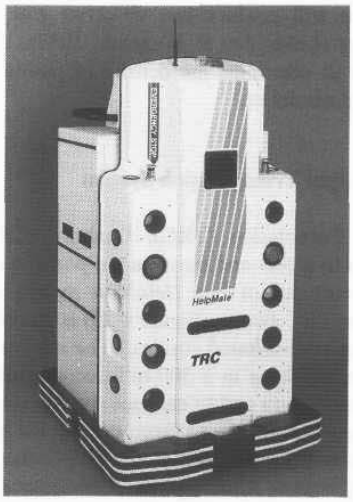

Figure 4-26. Slots for the two structured-light strobes are visible directly above and below the company's logo on the front panel of TRC *HelpMate* (courtesy Transitions Research Corp.).

4.5 Known Target Size

A stadimeter is a hand-held nautical instrument used for optically measuring the distance to objects of known heights, typically between 50 and 200 feet, covering ranges from 200 to 10,000 yards. The stadimeter measures the angle subtended by the object, and converts it into a range reading taken directly from a micrometer drum (Dunlap & Shufeldt, 1972).

The final variation on the triangulation ranging method to be discussed makes use of this same technique. Range is calculated through simple trigonometry; the known baseline, instead of being between two cameras (or a detector and a light source) on the robot, is now the target itself. The concept is illustrated in Figure 4-27. The only limiting constraint (besides knowing the size of the target) is the target must be normal to the optical axis of the sensor, which in the case of a passive system can be an ordinary CCD camera. The standard lens equation applies:

$$\frac{1}{r}+\frac{1}{s}=\frac{1}{f}$$

where:

r = distance from lens to object viewed
s = distance from lens to image plane
f = focal length of the lens.

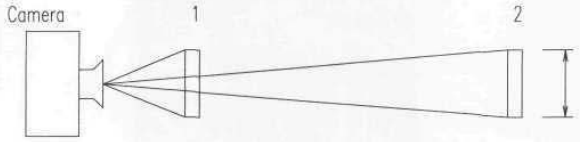

Figure 4-27. The angle subtended by an object of known size is observed to increase as the distance decreases in moving from position 2 to position 1, and can be used to derive the unknown range.

Now suppose the camera views an open doorway of known width A. If A is relatively small compared to the unknown distance r, then the range can be approximated by the formula (Nitzan, et al., 1986):

$$r=\frac{Af}{w}$$

where:

A = known width
w = perceived width in image plane.

If the view angle for the object of interest is wide (*i.e.*, A is not small with respect to r), then local geometric features should be examined (Nitzan, et al., 1986).

4.5.1 NAMCO *Lasernet® Scanning Laser Sensor*

One implementation of this ranging concept employs a scanning laser source mechanically coupled to a photodiode detector. NAMCO Controls, Mentor, OH, developed the *Lasernet® Scanning Laser Sensor* (Figure 4-28) for automated guided vehicle (AGV) applications in industrial environments (see also Chapter 15). A retroreflective target of known width is placed in a strategically located position to serve as a navigational aid (Laskowski, 1988). As the rotating laser scans across the retroreflector, energy is returned to the collocated detector. The length of the arc of rotation during which the detector senses reflected energy is directly related to the distance to the target: the closer the target, the longer the

perceived arc. Multiple targets can be processed simultaneously, and it is also possible to specifically identify objects through the use of uniquely identifiable codes.

Figure 4-28. The *Lasernet*® system detects retroreflective targets with a scanning near-infrared laser to provide bearing and range information used in the navigation of automated guided vehicles (courtesy NAMCO Controls).

A solid-state diode laser source, photodetector, mechanical scanner, beam-forming optics, and control electronics are housed in an enclosure measuring 5 by 6.5 by 3.4 inches for the standard range unit, and 5 by 9 by 3.4 inches for the long-range unit. The photodiode detector has an operational bandwidth of 1.0 MHz, tailored to receive inputs only from the 670-nanometer region of the spectrum. A servo-controlled rotating mirror horizontally pans the laser beam through a 90-degree field of view (45 degrees off either side of centerline) at a rate of 20 scans per second. A directional mirror routes the beam from the laser diode to the scanning mirror; a collecting lens focuses the return signal onto the photodetector.

The standard retroreflective test target used by the developer is a 4- by 4-inch square surface of corner-cube prisms with an overall 90-percent reflection coefficient. When the laser beam sweeps across a retroreflective target, a return signal of finite duration is sensed by the detector. Since the targets are all the same size, the return generated by a close target will be of longer duration than that from a distant one (Figure 4-29). In effect, the closer target appears larger.

The standard model of *Lasernet*® can process up to eight retroreflective targets simultaneously for range and/or angle information. Range is calculated from the equation (NAMCO, 1989):

$$d = \frac{W}{2\tan(\frac{vT_a}{2})}$$

where:

d = range to target
W = target width
v = scan velocity (7200 degrees/second)
T_a = duration of the returned pulse.

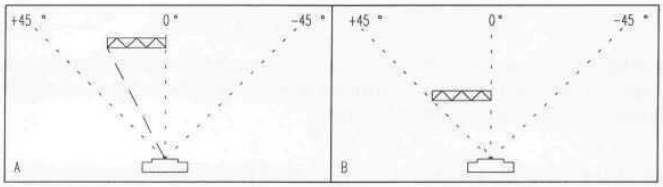

Figure 4-29. The NAMCO *Lasernet*® system determines both range (A) and bearing (B) for standard-size retroreflective targets (adapted from NAMCO, 1989).

Because the target width and angular scan velocity are known, the equation reduces to an inverse function of the pulse duration T_a. With 4-inch targets, the effective range of the sensor is from 1 to 20 feet (2 to 50 feet for the long-range model), and range resolution for either model is 9.6 inches (1.57 inches using digital output) at 20 feet down to 0.1 inch (0.017 inch using digital output) at 1 foot. *Lasernet*® produces an analog output ranging from 0 to 10 volts over the range 0 to 20 feet, and an inverse range function (representing T_a rather than d) digital output on an RS-232 serial port.

The above calculation assumes the target is positioned perpendicular to the angle of incidence of the laser source. If a planar target happens to be rotated or otherwise skewed away from the perpendicular, the resulting decrease in apparent cross-section will induce a range measurement error. Cylindrical targets are sometimes used to overcome this problem.

4.6 Optical Flow

The observed two-dimensional displacement of the brightness pattern in a video image known as optical flow represents a promising new method of obstacle avoidance. The perceived "flow" results from the relative motion between the moving camera and the viewed objects in the surrounding environment, as seen over a sequence of images. Each pixel has an associated instantaneous velocity vector representing the image motion at that point. For example, Figure 4-30 shows an optical flow field resulting from the translational motion of a camera

mounted on a vehicle traveling on a planar surface. The optical-flow vectors from closer objects will have greater magnitudes than the vectors from distant objects.

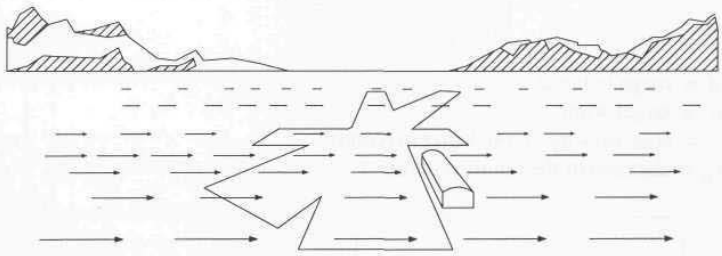

Figure 4-30. The optical flow field due to translation in a direction perpendicular to the camera optical axis will show decreased flow magnitudes with increasing range (reprinted with permission from Gibson, 1950, © Houghton Mifflin Company).

One of the main advantages of using optical flow is that the ratio of distance to speed (e.g., time-to-collision) can be easily obtained and used to generate avoidance maneuvers (Young et al., 1992; Heeger & Jepson, 1990a, 1990b). Disadvantages are seen in the required computational hardware: to achieve real-time results requires processing power on the order of a 50-MHz 80486-based system, which eats up energy at a pretty significant rate.

The optical flow often cannot be found by local computations on the image pixels due to a phenomenon known as the *aperture problem*. However, the component of the optical flow in the direction of the *local brightness gradient* (also known as the *normal flow*, since it is perpendicular to the brightness edge) can always be computed locally without a great deal of difficulty. The magnitude of the *normal flow vector* is:

$$M_n = \frac{E_t}{\sqrt{E_x^2 + E_y^2}}$$

where:

M_n = normal flow vector magnitude
E_t = time derivative of pixel brightness
E_x = spatial derivative along x axis
E_y = spatial derivative along y axis.

When the motion of the camera is known, distances to points in the scene can be computed directly from the normal flow, with most accurate results at points where both the brightness gradient and the normal flow are greatest (Nguyen, 1993).

When camera motion is not known, the camera motion and distances to points in the scene can be recovered from the optical flow, but only up to a scaling

factor. That is, it is possible to find the ratios between the distances to different points in the image, but not their absolute distances. If the distance to one point can be pin-pointed by another method (such as active sonar), however, then the distances to all points will be known. The computations are easiest if the camera motion is purely translational or purely rotational (Horn, 1986). Iterative and approximation schemes for estimating camera motion and distances from visual motion are still being actively investigated (Fermuller, 1991; Duric, 1991).

4.6.1 NIST Passive Ranging and Collision Avoidance

The method of flow extraction employed by the National Institute for Standards and Technology (NIST) reduces the computational burden by assuming that the camera is moving in a known fashion in a stationary world (Herman & Hong, 1991). These assumptions lead to two conclusions:

- The optical-flow field in the image (i.e., the flow direction at every point) can be predicted.
- Once the optical flow has been extracted, the flow vectors can be easily converted to range values.

These conclusions are generally true for arbitrary camera motion, including pure translation, pure rotation, and a combination of translation and rotation. The assumption that the flow field can be predicted enables precalculation of the true flow-vector directions; to extract optical flow, only the magnitudes of the flow vectors need to be computed. Knowledge of the flow field also enables the use of local image operators (for extracting information) that can run in parallel at all points in the image, further minimizing computation time. Additional details on the algorithms are presented by Lau, et al., (1992) and Liu, et al. (1993).

4.6.2 David Sarnoff Passive Vision

Researchers at David Sarnoff Research Center have developed algorithms for recovering scene geometry (range, 3-D orientation, and shape) from passively acquired binocular and motion imagery. Distance measurements are derived from intensity derivatives of two or more images of the same scene. The approach combines a local-brightness-constancy constraint with a global-camera-motion constraint to relate local range values with a global camera model and local image intensity derivatives.

Beginning with initial estimates of the camera motion and local range, the range is refined using the camera motion model as a constraint, whereupon the model is refined using local range estimates as constraints. This estimation procedure is iterated several times until convergence. The entire procedure is

performed within a (spatially) coarse-to-fine algorithmic framework. Demonstration of this technology has made use of a commercial CCD camera and frame grabber for image capture coupled with a workstation to perform the actual range recovery in non-real-time. By way of illustration, Figure 4-31 (left) shows one image from a stereo pair; the brighter regions in the recovered range map depicted in Figure 4-31 (right) represent those regions closer to the cameras. The range values are plausible almost everywhere except at the image border and in the vicinity of the focus of expansion (near the image center).

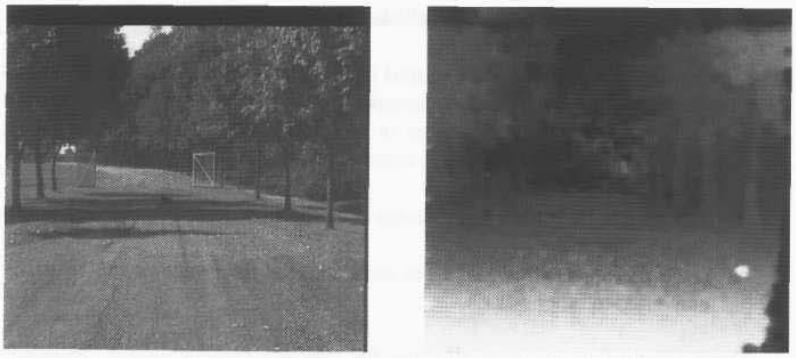

Figure 4-31. One image of a pair is shown at left; pixel intensity in the resulting 3-D range map (right) is inversely related to range (courtesy David Sarnoff Research Center).

Limitations of this approach are two-fold. First, the basic formulation assumes that camera motion is small between captured images and that the image intensity of the same point between images is constant (brightness constancy); violation of either of these constraints can lead to erroneous results. Second, current estimates for a real-time implementation in commercially available hardware suggest that power requirements will be approximately 60 watts. Additional technical details on this technology are presented by Hanna (1991) and Wildes (1990a, 1190b, & 1991).

4.7 References

Aloimonos, J., Weiss, I., Bandyopadhyay, A., "Active Vision," First International Conference on Computer Vision, pp. 35-54, 1987.

Anderson, C.H., Burt, P.J., van der Wal, G. S., "Change Detection and Tracking Using Pyramid Transform Techniques," SPIE Vol. 579, Intelligent Robots and Computer Vision, pp. 72-78, 1985.

Bedard, R.J., et al., "Navigation of Military and Space Unmanned Ground Vehicles in Unstructured Terrains," 3rd Military Robotic Vehicle Conference, Medicine Hat, Canada, September 9-12, 1991a.

Bedard, R.J., et al., "The 1991 NASA Planetary Rover Program," 42nd International Astronautical Federation, Montreal, Canada, October 6-9, 1991b.

Besl, P.J., "Range Imaging Sensors," GMR-6090, General Motors Research Laboratory, 1988.

Blais, F., Rioux, M., Domey, J., Beraldin, J.A., "A Very Compact Real Time 3-D Range Sensor for Mobile Robot Applications," SPIE Vol. 1007, Mobile Robots III, Cambridge, MA, November, 1988.

Blais, F., Rioux, M., Domey, J., Beralsin, J.A., "On the Implementation of the BIRIS Range Sensor for Applications in Robotic Control and Autonomous Navigation," Canadian Conference on Electrical and Computer Engineering, Attawa, Ontario, Canada, pp. 37.1.1-37.1.4, September, 1990.

Burt, P.J., Adelson, E.H., "The Laplacian Pyramid as a Compact Image Code," *IEEE Transactions on Communications*, Vol. COM-31, No. 4, pp. 532-540, April, 1983

Burt, P.J., Anadan, P., Hanna, K., van der Wal, G., "A Front End Vision Processor for Unmanned Vehicles," Advanced Image Processing Group, David Sarnoff Research Center, Princeton, NJ, April, 1992.

Burt, P.J., Anadan, P., Hanna, K., van der Wal, G., Bassman, R., "A Front End Vision Processor for Vehicle Navigation," International Conference on Intelligent Systems, pp. 653-662, February, 1993.

Burt, P.J., Anadan, P., "Image Stabilization by Registration to a Reference Mosaic," 1994 Image Understanding Workshop, Monterey, CA, pp. 425-434, November, 1994.

Conrad, D.J., Sampson, R.E., "3D Range Imaging Sensors," in *Traditional and Non-Traditional Robotic Sensors*, T.C. Henderson, ed., NATO ASI Series, Vol. F63, Springer-Verlag, pp. 35-47, 1990.

Dunlap, G.D., Shufeldt, H.H., *Dutton's Navigation and Piloting*, Naval Institute Press, p. 1013, 1972.

Duric, Z., Aloimonos Y., "Passive Navigation: An Active and Purposive Solution," Technical Report CAR-TR-560, Center for Automation Research, University of Maryland, College Park, MD, 1991.

Evans, J.M., King, S.J., Weiman, C.F.R., "Visual Navigation and Obstacle Avoidance Structured Light Systems," U.S. Patent No. 4,954,962, 4 September, 1990.

Everett, H.R., DeMuth, D.E., Stitz, E.H., "Survey of Collision Avoidance and Ranging Sensors for Mobile Robots," Technical Report 1194, Naval Command Control and Ocean Surveillance Center, San Diego, CA, December, 1992.

Fermuller, C., Aloimonos, Y., "Estimating 3-D Motion from Image Gradients," Technical Report CAR-TR-564, Center for Automation Research, University of Maryland, College Park, MD, 1991.

Gibson, J., *The Perception of the Visual World*, Houghton Mifflin, Boston, MA, 1950.

Hanna, K.J., "Direct Multi-Resolution Estimation of Ego-Motion and Structure from Motion," Proceedings of IEEE Workshop on Visual Motion, pp. 156-162, 1991.

Hansen, M., Anandan, P., Dana, K., van der Wal, G, Burt, P., Real-Time Scene Stabilization and Mosaic Construction," 1994 Image Understanding Workshop, Monterey, CA, pp. 457-465, November, 1994.

Hamamatsu, "16 Step Range-Finder IC H2476- 01," Product Literature , Hamamatsu Corporation, January, 1990.

Heeger, D.J., Jepson, A., "Method and Apparatus for Image Processing to Obtain Three Dimensional Motion and Depth," U.S. Patent 4,980,762, MIT, Cambridge, MA, 25 December, 1990a

Heeger, D.J., Jepson, A., "Subspace Methods for Recovering Rigid Motion I: Algorithm and Implementation," Technical Report RBCV-TR- 90-35, University of Toronto, Ontario, Canada, November, 1990b.

Herman, M., Hong, T., "Visual Navigation using Optical Flow," Proceedings NATO Defense Research Group Seminar on Robotics in the Battlefield, Paris, France, March, 1991.

Horn, B. K. P., *Robot Vision*, The MIT Press, Cambridge, MA, 1986.

Jarvis, R.A., "A Perspective on Range Finding Techniques for Computer Vision," IEEE Transactions on Pattern Analysis and Machine Intelligence, Vol. PAMI-1, No. 2, pp. 122-139, March, 1983a.

Jarvis, R.A., "A Laser Time-of-Flight Range Scanner for Robotic Vision," IEEE Transactions on Pattern Analysis and Machine Intelligence, Vol. PAMI-5, No. 5, pp. 505-512, September, 1983b.

Kent, E.W., et al., Real-time Cooperative Interaction Between Structured Light and Reflectance Ranging for Robot Guidance," Robotica, Vol. 3, pp. 7-11, January-March, 1985.

Kilough, S.M., Hamel, W.R., "Sensor Capabilities for the HERMIES Experimental Robot," American Nuclear Society, Third Topical Meeting on Robotics and Remote Systems, Charleston, SC, CONF-890304, Section 4-1, pp. 1-7, March, 1989.

King, S.J., Weiman, C.F.R., "HelpMate Autonomous Mobile Robot Navigation System," SPIE Vol. 1388, Mobile Robots V, Boston, MA, pp. 190-198, November, 1990.

Laskowski, E.L., "Range Finder Wherein Distance Between Target and Source is Determined by Measuring Scan Time Across a Retroreflective Target," U.S. Patent No. 4,788,441, 29 November, 1988.

Lau, H., Hong, T., Herman, M., "Optimal Estimation of Optical Flow, Time-to-Contact and Depth," NISTIR 4919, National Institute of Standards and Technology, Gaithersburg, MD, September, 1992.

LeMoigue, J., Waxman, A.M., "Projected Light Grids for Short Range Navigation of Autonomous Robots," Proceedings, 7th IEEE Conference on Pattern Recognition, Montreal, Canada, pp. 203-206, 30 July - 2 August, 1984.

Liu, H., Hong, T., Herman, M., Chellappa, R., "A Reliable Optical Flow Algorithm Using 3-D Hermite Polynomials," NISTIR 5333, National Institute of Standards and Technology, Gaithersburg, MD, December, 1993.

Loewenstein, D., "Computer Vision and Ranging Systems for a Ping Pong Playing Robot," *Robotics Age*, pp. 21-25, August, 1984.

Malafeew, E., Kaliardos, W., "The MITy Micro-Rover: Sensing, Control, and Operation," AIAA/NASA Conference on Intelligent Robots in Field, Factory, Service, and Space, Houston, TX, pp. 696-704, March, 1994.

Matthies, L.H., "Stereo Vision for Planetary Rovers: Stochastic Modeling to Near-Real-time Implementation," International Journal of Computer Vision, Vol. 8, No. 1, July, 1992a.

Matthies, L.H., "Passive Stereo Range Imaging for Semi-Autonomous Land Navigation," Journal of Robotic Systems, Vol. 9, No. 6, September, 1992b.

Moser, J., Everett, H.R., "Wide-Angle Active Optical Triangulation Ranging System," SPIE Vol. 1195, Mobile Robots IV, Philadelphia, PA, November, 1989.

NAMCO, "LNFL03-A 5M/4-90," *Lasernet* Product Bulletin, NAMCO Controls, Mentor, OH, November, 1989.

Nitzan, D., "Assessment of Robotic Sensors," Proceedings of 1st International Conference on Robotic Vision and Sensory Controls, pp. 1-11, 1-3 April, 1981.

Nitzan, D. et al., "3-D Vision for Robot Applications." NATO Workshop: Knowledge Engineering for Robotic Applications, Maratea, Italy, 12-16 May, 1986.

Nguyen, H. G., "Summary of Auto-Landing Problem Analysis and Proposal," NRaD Memorandum 943/11-93, Naval Command Control and Ocean Surveillance Center, February, 1993.

Nguyen, H.G., Blackburn, M.R., "A Simple Method for Range Finding via Laser Triangulation," NCCOSC Technical Document, TD-2734, Naval Command Control and Ocean Surveillance Center, San Diego, CA, January, 1995.

Poggio, T., "Vision by Man and Machine," *Scientific America*, Vol. 250, No. 4, pp. 106-116, April, 1984.

Rioux, M., Blais, F., "Compact Three-Dimensional Camera for Robotic Applications," Journal of Optical Society of America, Vol. 3, pp. 1518-1521, September, 1986.

Schwartz, J.T., "Structured Light Sensors for 3-D Robot Vision," Technical Report No. 65, Courant Institute of Mathematical Sciences, New York University, undated.

Slack, M., "Generating Symbolic Maps from Grid Based Height Maps," JPL-D-6948, December 7, 1989.

Swain, M.J., Stricker, M., eds., *Promising Directions in Active Vision*, Report from the National Science Foundation Active Vision Workshop, University of Chicago, IL, 1991.

Uomori, K., Morimura, A., Ishii, A., Sakaguchi, H., Kitamura, Y., "Automatic Image Stabilizing System by Full Digital Signal Processing," *IEEE Transactions on Consumer Electronics*, Vol. 36, No. 3, pp. 510-519, 1990.

Vuylsteke, P., Price, C.B., Oosterlinck, A., "Image Sensors for Real-Time 3D Acquisition, Part 1," *Traditional and Non-Traditional Robotic Sensors*, T.C. Henderson, ed., NATO ASI Series, Vol. F63, Springer-Verlag, pp. 187-210, 1990.

Wavering, A.J., Fiala, J.C., Roberts, K.J., Lumia, R., "TRICLOPS: A High-Powered Trinocular Active Vision System," IEEE International Conference on Robotics and Automation, pp. 410-417, 1993.

Wildes, R.P., "Qualitative 3D Shape from Stereo," SPIE Intelligent Robots and Computer Vision Conference, pp. 453-463, 1990a.

Wildes, R.P., "Three-Dimensional Surface Curvature from Binocular Stereo Disparity," *Optical Society of America Technical Digest*, Vol. 25, p. 58, 1990b.

Wildes, R.P., "Direct Recovery of Three-Dimensional Scene Geometry from Binocular Stereo Disparity," *IEEE Transactions on Pattern Analysis and Machine Intelligence*, Vol. 13, No. 8, pp. 761-774, August, 1991.

Young, G.S., Hong, T.H., Herman, M., Yang, J.C.S., "Obstacle Avoidance for a Vehicle Using Optical Flow," Technology Description, NIST, Gaithersburg, MD, July, 1992.

5
Time of Flight

Time-of-flight (TOF) ranging systems measure the round-trip time required for a pulse of emitted energy to travel to a reflecting object, then echo back to a receiver. Ultrasonic, RF, or optical energy sources are typically employed; the relevant parameters involved in range calculation, therefore, are the speed of sound in air (roughly 1 foot per millisecond), and the speed of light (1 foot per nanosecond). Using elementary physics, distance is determined by multiplying the velocity of the energy wave by the time required to travel the round-trip distance:

$$d = v\,t$$

where:

d = round-trip distance
v = speed of propagation
t = elapsed time.

The measured time is representative of traveling twice the separation distance (i.e., out and back) and must therefore be reduced by half to result in actual range to the target.

The advantages of *TOF* systems arise from the direct nature of their straight-line active sensing. The returned signal follows essentially the same path back to a receiver located coaxially with or in close proximity to the transmitter. In fact, it is possible in some cases for the transmitting and receiving transducers to be the same device. The absolute range to an observed point is directly available as output with no complicated analysis required, and the technique is not based on any assumptions concerning the planer properties or orientation of the target surface. The *missing parts* problem seen in triangulation does not arise because minimal or no offset distance between transducers is needed. Furthermore, *TOF* sensors maintain range accuracy in a linear fashion as long as reliable echo detection is sustained, while triangulation schemes suffer diminishing accuracy as distance to the target increases.

Potential error sources for *TOF* systems include the following:

- Variations in the speed of propagation, particularly in the case of acoustical systems.
- Uncertainties in determining the exact time of arrival of the reflected pulse (Figueroa & Lamancusa, 1992).
- Inaccuracies in the timing circuitry used to measure the round-trip time of flight.
- Interaction of the incident wave with the target surface.

Each of these areas will be briefly addressed below, and discussed later in more detail along with other factors influencing performance in Chapters 8 and 9.

Propagation Speed — For mobile robotic applications, changes in the propagation speed of electromagnetic energy are for the most part inconsequential and can basically be ignored, with the exception of satellite-based position-location systems as presented in Chapter 14. This is not the case, however, for acoustically based systems, where the speed of sound is markedly influenced by temperature changes, and to a lesser extent by humidity. (The speed of sound is actually proportional to the square root of temperature in degrees Rankine; an ambient temperature shift of just 30 degrees can cause a 1-foot error at a measured distance of 35 feet.)

Detection Uncertainties — So called *time-walk errors* are caused by the wide dynamic range in returned signal strength as a result of: 1) varying reflectivities of target surfaces, and, 2) signal attenuation to the fourth power of distance due to spherical divergence. These differences in returned signal intensity influence the rise time of the detected pulse, and in the case of fixed-threshold detection will cause the less reflective targets to appear further away (Lang, et al., 1989). For this reason, *constant fraction timing discriminators* are typically employed to establish the detector threshold at some specified fraction of the peak value of the received pulse (Vuylsteke, et al., 1990). See also Chapter 8.

Timing Considerations — The relatively slow speed of sound in air makes TOF ranging a strong contender for low-cost acoustically-based systems. Conversely, the propagation speed of electromagnetic energy can place severe requirements on associated control and measurement circuitry in optical or RF implementations. As a result, TOF sensors based on the speed of light require subnanosecond timing circuitry to measure distances with a resolution of about a foot (Koenigsburg, 1982). More specifically, a desired resolution of 1 millimeter requires a timing accuracy of 3 picoseconds (Vuylsteke, et al., 1990). This capability is somewhat expensive to realize and may not be cost effective for certain applications, particularly at close range where high accuracies are required.

Surface Interaction — When light, sound, or radio waves strike an object, any detected echo represents only a small portion of the original signal. The remaining energy reflects in scattered directions and can be absorbed by or pass

through the target, depending on surface characteristics and the angle of incidence of the beam. Instances where no return signal is received at all can occur because of specular reflection at the object surface, especially in the ultrasonic region of the energy spectrum. If the transmission source approach angle meets or exceeds a certain critical value, the reflected energy will be deflected outside of the sensing envelope of the receiver. Scattered signals can reflect from secondary objects as well, returning to the detector at various times to generate false signals that can yield questionable or otherwise noisy data. To compensate, repetitive measurements are usually averaged to bring the signal-to-noise ratio within acceptable levels, but at the expense of additional time required to determine a single range value.

5.1 Ultrasonic TOF Systems

Ultrasonic TOF ranging is today the most common technique employed on indoor mobile robotic systems, primarily due to the ready availability of low-cost systems and their ease of interface. Over the past decade, much research has been conducted investigating applicability in such areas as world modeling and collision avoidance (Chapter 10), position estimation (Chapter 15), and motion detection (Chapter 17). Several researchers have more recently begun to assess the effectiveness of ultrasonic sensors in exterior settings (Pletta, et al., 1992; Langer & Thorpe, 1992; Pin & Watanabe, 1993; Hammond, 1994). In the automotive industry, BMW now incorporates four piezoceramic transducers (sealed in a membrane for environmental protection) on both front and rear bumpers in its Park Distance Control system (Siuru, 1994).

Four of the most popular commercially available ultrasonic ranging systems will be reviewed in the following sections.

5.1.1 National Semiconductor's *LM1812 Ultrasonic Transceiver*

The *LM1812,* discontinued in 1990, was a general purpose ultrasonic transceiver IC originally designed to support fish- and depth-finding products in the recreational electronics industry (Frederiksen & Howard, 1974). The 18-pin chip contained a pulse-modulated class-C transmitter, a high-gain receiver, a pulse modulation detector, and noise rejection circuitry as shown in Figure 5-1 (National, 1991). Maximum range was 100 feet in water and 20 feet in air, at typical operating frequencies of 20 to 350 KHz.

The chip's specifications (National, 1989) listed the following features:

- *Monostatic* (single transducer) or *bistatic* (dual transducer) operation.
- Transducers interchangeable without realignment.
- No external transistors required.

- Impulse noise rejection.
- No heat sinking required.
- 12 watts peak transmit power.
- Power consumption of 50 milliamps at 18 volts DC.

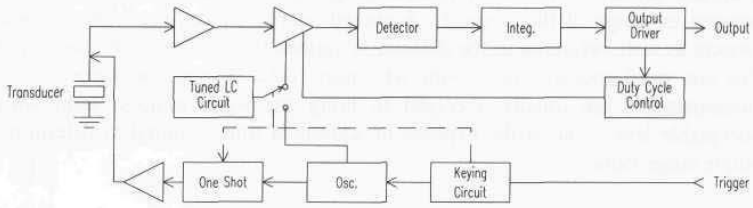

Figure 5-1. Block diagram of *LM1812* monolithic sonar transceiver (courtesy National Semiconductor Corporation).

Two different types of ultrasonic transducers, *electrostatic* and *piezoceramic* (also known as *piezoelectric*), were commonly used with the *LM1812* (Everett, 1982; Pletta, et al., 1992). *Electrostatic* transducers transmit an outgoing signal and act as an electrostatic microphone in order to receive the reflected waveform (National, 1991). *Piezoceramic* transducers are electrically similar to quartz crystals and resonant at only two frequencies: the *resonant* and *antiresonant* frequencies (Pletta, et al., 1992). Transmission is most efficient at the resonant frequency while optimum receiving sensitivity occurs at the antiresonant frequency (National, 1989). In bistatic systems, the resonant frequency of the transmitting transducer is matched to the antiresonant frequency of the receiver for optimal performance.

The majority of practical applications, however, use a monostatic configuration for which the maximum echo sensitivity occurs at a frequency close to resonance. The ultrasonic ranging system on ROBART I, for example, was based on the *LM1812* in conjunction with a single 40-KHz piezoceramic transducer (see Chapter 10). Pletta, et al. (1992) elected to use three Massa piezoceramic transducers operating at 26 KHz in an *LM1812*-based collision-avoidance sonar for Sandia's *Telemanaged Mobile Security System.* Effective range to favorable targets (rough surfaced or normal to the beam) was approximately 12 meters.

The receiver gain could be varied over time by attenuating the signal between pin 3 (first-stage amplifier output) and pin 2 (second-stage amplifier input) using external circuitry as shown in Figure 5-2. The 12-volt trigger pulse that keyed the transmitter simultaneously charged C_1 to a preset voltage determined by R_8, thereby turning off the FET to block the transducer ring-down signal (National, 1989). C_1 then slowly discharged through R_1, decreasing the gate voltage and allowing the FET to conduct. The resulting attenuation of the received signal thus decreased as the voltage on C_1 fell, effectively increasing overall receiver gain as a function of elapsed time. This feature served to both block the unwanted ring-

down effect as well as keep the amplifier gain proportionally matched to the decay in returned-echo intensity resulting from the inverse square law.

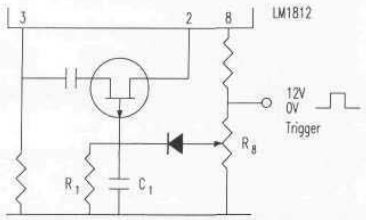

Figure 5-2. An optional time-variable FET attenuator could be connected between pins 2 and 3 of the *LM1812* to implement a ramped-gain response (adapted from National, 1989).

5.1.2 Massa Products *Ultrasonic Ranging Module Subsystems*

Massa Products Corporation, Hingham, MA, offers a full line of ultrasonic ranging subsystems with maximum detection ranges from 2 to 30 feet (Massa, undated). The *E-201B series* sonar operates in the bistatic mode with separate transmit and receive transducers, either side by side for echo ranging or as an opposed pair for unambiguous distance measurement between two uniquely defined points. This latter configuration is sometimes used in ultrasonic position location systems (see Chapter 15) and provides twice the effective operating range with respect to that advertised for conventional echo ranging. The *E-220B series* (Figure 5-3) is designed for monostatic (single-transducer) operation but is otherwise functionally identical to the *E-201B*. Either version can be externally triggered on command, or internally triggered by a free-running oscillator at a repetition rate determined by an external resistor.

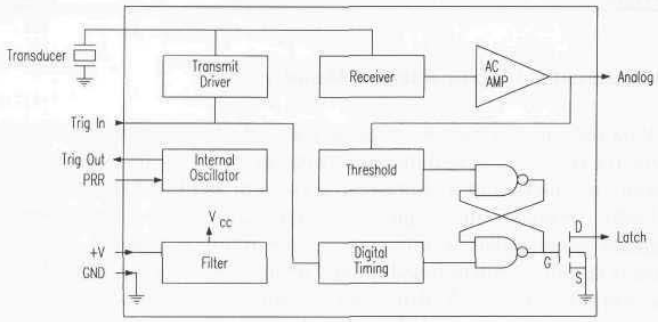

Figure 5-3. The single-transducer Massa *E-220B-series* ultrasonic ranging module can be internally or externally triggered and offers both analog and digital outputs (courtesy Massa Products Corp.).

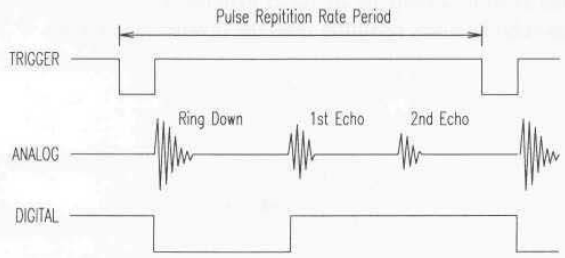

Figure 5-4. Timing diagram for the *E-220B series* ranging module showing analog and digital output signals in relationship to the trigger input (courtesy Massa Products Corp.).

Selected specifications for the four operating frequencies available in the *E-220B series* are listed in Table 5-1 below. A removable focusing horn is provided for the 26- and 40-KHz models that decreases the effective beamwidth (when installed) from 35 to 15 degrees. The horn must be in place to achieve the maximum listed range.

Table 5-1. Selected specifications for the monostatic *E-220B Ultrasonic Ranging Module Subsystems*. The *E-201 series* is a bistatic configuration with very similar specifications.

Parameter	220B/215	220B/150	220B/40	220B/26	Units
Range	4 - 24	8 - 60	24 - 240	24 - 360	inches
Beam width	10	10	35 (15)	35 (15)	degrees
Frequency	215	150	40	26	KHz
Max rep rate	150	100	25	20	Hz
Resolution	0.03	0.04	0.3	0.4	inches
Power	8 - 15	8 - 15	8 - 15	8 - 15	volts DC
Weight	4 - 8	4 - 8	4 - 8	4 - 8	ounces

5.1.3 Polaroid *Ultrasonic Ranging Modules*

The Polaroid ranging module is an active TOF device developed for automatic camera focusing and determines the range to target by measuring elapsed time between transmission of an ultrasonic waveform and the detected echo (Biber, et al., 1980). Probably the single most significant sensor development from the standpoint of its catalytic influence on the robotics research community, this system is the most widely found in the literature (Koenigsburg, 1982; Moravec & Elfes, 1985; Everett, 1985; Kim, 1986; Arkin, 1989; Borenstein & Koren, 1990). Representative of the general characteristics of a number of such ranging devices, the Polaroid unit soared in popularity as a direct consequence of its extremely low cost (Polaroid offers both the transducer and ranging module circuit board for less

than $50), made possible by high-volume usage in its original application as a camera autofocus sensor.

The most basic configuration consists of two fundamental components: 1) the ultrasonic transducer and 2) the ranging module electronics. A choice of transducer types is now available. In the original instrument-grade electrostatic version (Figure 5-5), a very thin metalized diaphragm mounted on a machined backplate forms a capacitive transducer (Polaroid, 1981). A smaller diameter electrostatic transducer (*7000-Series*) has also been made available, developed for the Polaroid *Spectra* camera (Polaroid, 1987). A ruggedized piezoelectric (*9000-Series*) *environmental transducer* introduced for applications that may be exposed to rain, heat, cold, salt spray, and vibration is able to meet or exceed guidelines set forth in SAE J1455 January 1988 specification for heavy-duty trucks.

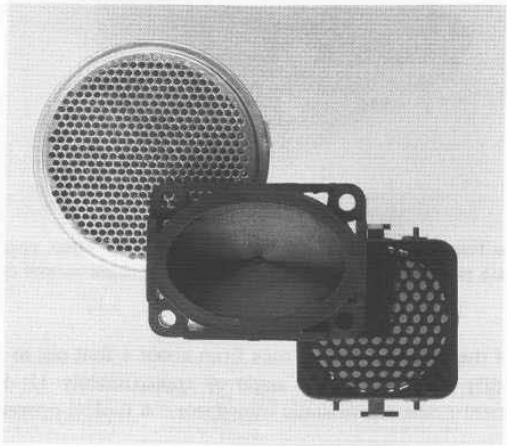

Figure 5-5. From left to right: 1) the original instrument grade electrostatic transducer, 2) *9000-Series* environmental transducer, and 3) *7000 Series* electrostatic transducer (courtesy Polaroid Corp.).

The original Polaroid ranging module (607089) functioned by transmitting a *chirp* of four discrete frequencies in the neighborhood of 50 KHz (see also Chapter 8). The *SN28827* module was later developed with a reduced parts count, lower power consumption, and simplified computer interface requirements. This second-generation board transmits only a single frequency at 49.1 KHz. A third-generation board (*6500 series*) introduced in 1990 provided yet a further reduction in interface circuitry, with the ability to detect and report multiple echoes (Polaroid, 1990). An *Ultrasonic Ranging Developer's Kit* based on the Intel *80C196* microprocessor is now available (Figure 5-6) that allows software control of transmit frequency, pulse width, blanking time, amplifier gain, and achieved range measurements from 1 inch to 50 feet (Polaroid, 1993).

Figure 5-6. The Polaroid *Ultrasonic Ranging Developer's Kit* offers programmable pulse, frequency, and gain parameters, with the ability to detect multiple echoes (courtesy Polaroid Corp.).

The range of the Polaroid system runs from about 1 foot out to 35 feet, with a half-power (-3dB) beam dispersion angle of approximately 12 degrees for the original instrument-grade electrostatic transducer. A typical operating cycle is as follows.

- The control circuitry fires the transducer and waits for an indication that transmission has begun.
- The receiver is blanked for a short period of time to prevent false detection due to residual transmit signal ringing in the transducer.
- The received signals are amplified with increased gain over time to compensate for the decrease in sound intensity with distance.
- Returning echoes that exceed a fixed-threshold value are recorded and the associated distances calculated from elapsed time.

In the *single-echo* mode of operation for the *6500-series* module, the *blank* (BLNK) and *blank-inhibit* (BINH) lines are held low as the *initiate* (INIT) line goes high to trigger the outgoing pulse train. The *internal blanking* (BLANKING) signal automatically goes high for 2.38 milliseconds to prevent transducer ringing from being misinterpreted as a returned echo. Once a valid return is received, the

echo (ECHO) output will latch high until reset by a high-to-low transition on INIT. For *multiple-echo* processing, the *blank* (BLNK) input must be toggled high for at least 0.44 milliseconds after detection of the first return signal to reset the *echo* output for the next return as shown in Figure 5-7 (Polaroid, 1990).

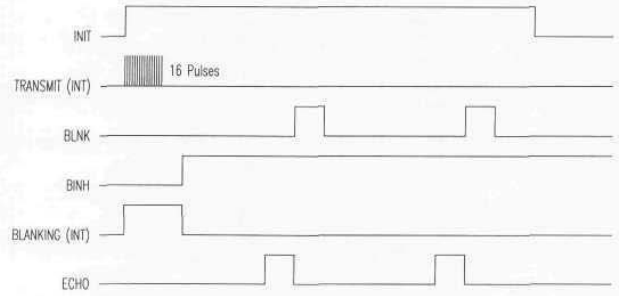

Figure 5-7. Timing diagrams for the 6500-*Series Sonar Ranging Module* executing a multiple-echo-mode cycle with blanking input (courtesy Polaroid Corp.).

The ultrasonic ranging capability of ROBART II is based entirely on the Polaroid system (three *SN28827* ranging modules each multiplexed to 12 electrostatic transducers). For obstacle avoidance purposes, a fixed array of 11 transducers is installed on the front of the body trunk to provide distance information to objects in the path of the robot as shown in Figure 5-8. A ring of 24 additional ranging sensors (15 degrees apart) is mounted just below the robot's head and used to gather range information for position estimation. A final ranging unit is located on the rotating head assembly, allowing for distance measurements to be made in various directions. Reliability of the Polaroid components has been exceptional, with no failures or degraded performance of any type in over eight years of extended operation.

Table 5-2. Selected specifications for the various Polaroid ultrasonic ranging modules.

Parameter	607089	SN28827	6500	Units
Maximum range	35	35	35	feet
Minimum range	10.5	6	6	inches
Number of pulses	56	16	16	
Blanking time	1.6	2.38	2.38	milliseconds
Resolution	1	2	1	percent
Gain steps	16	12	12	
Multiple echo	no	yes	yes	
Programmable frequency	no	no	yes	
Power	4.7 - 6.8	4.7 - 6.8	4.7 - 6.8	volts
	200	100	100	milliamps

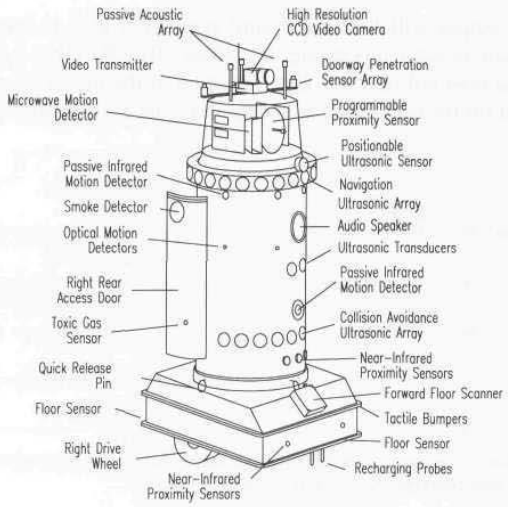

Figure 5-8. ROBART II, an autonomous security robot, employs a total of 132 external sensors for navigation and intruder detection, including 36 Polaroid electrostatic transducers.

5.1.4 Cybermotion *CA-2 Collision Avoidance System*

The *CA-2 Collision Avoidance System* is a dual-channel ultrasonic ranging module developed by Cybermotion, Inc., Salem, VA, for use on indoor vehicles operating at speeds up to 10 miles per hour. The *CA-2* achieves a maximum detection range of 8 feet at a 10-Hz update rate, with programmable resolution (0.084 inch standard) over the span of interest (Cybermotion, 1991). Two broad-beam (70-degree) ceramic transducers are employed for maximum protection in the direction of vehicle travel. Four operating modes are provided:

- OFF — The system is powered up but no transducers are fired.
- LEFT — The left transducer only is fired.
- RIGHT — The right transducer only is fired.
- BOTH — The left and right transducers are alternately fired.

Hammond (1993) reports that most man-made noise sources have energy peaks below 50 KHz, and much of this industrial noise spectrum is avoided by choosing an operating frequency of 75 KHz. In addition, the *CA-2* employs a number of specialized techniques for improving the generally poor signal-to-noise ratio experienced by wide-beam transducers in order to achieve higher immunity to sources of ultrasonic interference (i.e., rotating machinery, leaking or rushing air, fluorescent lighting, other ultrasonic equipment). Referring now to Figure 5-9,

the received echo signal generated by the ultrasonic transducer is passed through a narrow-band gain-controlled amplifier before presentation to an envelope detector and two additional stages of baseband filtering. The output signal is then digitized and stored in memory, whereupon five different filtering algorithms are invoked to eliminate transducer ring-down, white noise, impulse noise, residual echoes from previous ranging operations, and interference from other robots (Hammond, 1993).

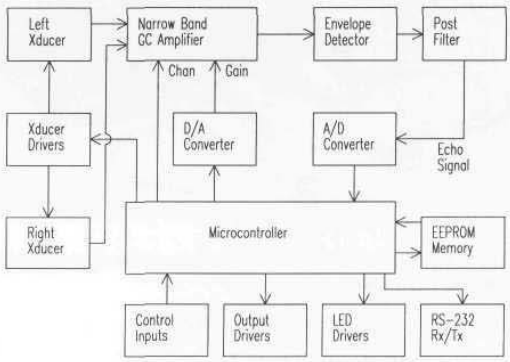

Figure 5-9. Block diagram of the Cybermotion *CA-2* Collision Avoidance System (adapted from Hammond, 1993).

The resulting digital signature is then compared to a complex threshold generated from a programmable baseline and several dynamically calculated components, with distance computed for the first point in time where signal amplitude exceeds the threshold value. This *range to first echo* is compared to three preset variables downloaded from system EEPROM on initialization (or subsequently reset by an external command):

- SLOW — Range threshold for causing the vehicle to decrease speed.
- STOP — Range threshold below which the vehicle should stop.
- HORN — Range threshold for enabling a warning enunciator.

If the measured range is less than any of the threshold values listed above for any two of five consecutive readings, the appropriate output signal is generated. The measured range must then exceed the prespecified threshold for five consecutive pings to cancel the indicated condition. Red LED status lights are associated with both the SLOW and STOP outputs for convenience.

The *CA-2* (Figure 5-10) is offered by Cybermotion as a stand-alone unit measuring 7.25 wide, 5.75 inches deep, and 1 inch high, with both parallel and serial interfaces. System sensitivity is programmable, down to as small as a 1-

inch-square surface at a distance of 5 feet. Power consumption is 150 milliamps at 12 volts DC.

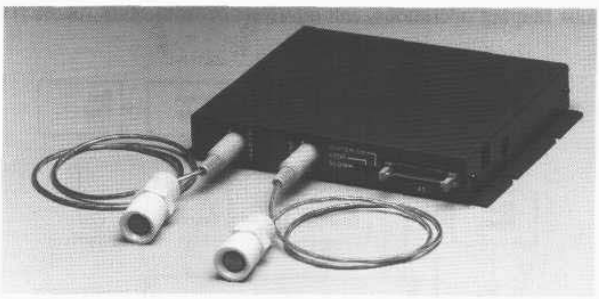

Figure 5-10. The *CA-2 Collision Avoidance System* is available as a stand-alone non-contact ranging subsystem (courtesy Cybermotion, Inc.).

5.2 Laser-Based TOF Systems

Laser-based TOF ranging systems, also known as *laser radar* or *lidar*, first appeared in work performed at the Jet Propulsion Laboratory, Pasadena, CA, in the 1970s (Lewis & Johnson, 1977). Laser energy is emitted in a rapid sequence of short bursts aimed directly at the object being ranged. The time required for a given pulse to reflect off the object and return is measured and used to calculate distance to the target based on the speed of light. Accuracies for early sensors of this type could approach a few centimeters over the range of 1 to 5 meters (NASA, 1977; Depkovich & Wolfe, 1984).

5.2.1 Schwartz Electro-Optics Laser Rangefinders

Schwartz Electro-Optics, Inc. (SEO), Orlando, FL, produces a number of laser TOF rangefinding systems employing an innovative *time-to-amplitude-conversion* scheme to overcome the subnanosecond timing requirements necessitated by the speed of light. As the laser fires, a precision film capacitor begins discharging from a known setpoint at a constant rate, with the amount of discharge being proportional to the round-trip time-of-flight (Gustavson & Davis, 1992). An analog-to-digital conversion is performed on the sampled capacitor voltage at the precise instant a return signal is detected, whereupon the resulting digital representation is converted to range and time-walk corrected using a look-up table.

SEO *LRF-X* Series Rangefinders

The *LRF-X* series rangefinder shown in Figure 5-11 features a compact size, high-speed processing, and an ability to acquire range information from most surfaces (i.e., minimum 10-percent Lambertian reflectivity) out to a maximum of 100 meters. The basic system uses a pulsed InGaAs laser diode in conjunction with an avalanche photodiode detector and is available with both analog and digital (RS-232) outputs. The following general specifications detail the sensor's performance (SEO, 1991a).

Figure 5-11. The *LRF-200* series rangefinder (courtesy Schwartz Electro Optics, Inc.).

Table 5-3. Selected specifications for the *LRF-200* laser rangefinder.

Parameter	Value	Units
Maximum range	100	meters
Minimum range	1	meter
Accuracy	±0.3	meter
Range jitter	±12	centimeters
Wavelength	902	nanometers
Diameter	8.9	centimeters
Length	17.75	centimeters
Weight	1	kilogram
Power	8 to 24	volts DC
	5	watts

The *High Accuracy Altitude Measurement System (HAAMS)* is an enhanced variation of the basic *LRF* concept intended as a *lidar altimeter* for aircraft. The *HAAMS* system operates at a 3-KHz update rate with a maximum range of 200 meters and is available in the same 8.9-centimeter-diameter cylindrical package as the *LRF-200*. An inclinometer was added to automatically compensate for aircraft angle of bank. In addition, peak-detection feedback was incorporated to reduce *time-walk errors* for an increased accuracy of 3 to 4 inches.

SEO Hover Obstacle Proximity Sensor System

The *Hover Obstacle Proximity Sensor System (HOPSS)* was developed for the US Army (SEO, 1991c) as an onboard pilot alert to the presence of surrounding obstructions. Located on the bottom of the fuselage directly below the main-rotor driveshaft (Figure 5-12), the *HOPSS* system provides continuous distance and azimuth measurements in the horizontal plane of a helicopter.

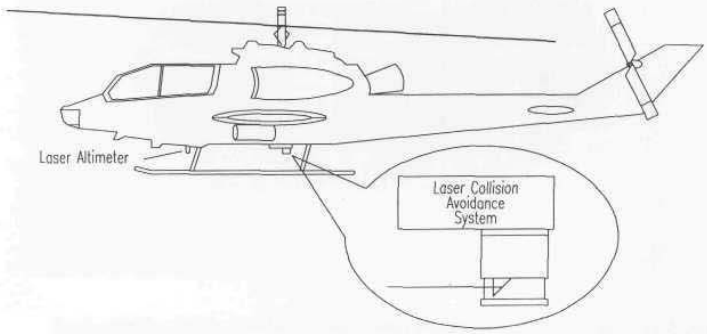

Figure 5-12. Placement of the *Hover Optical Proximity Sensor System* on a US Army helicopter (courtesy Schwartz Electro-Optics, Inc.).

A high-pulse-repetition-rate GaAs laser-diode emitter shares a common aperture with a sensitive avalanche photodiode detector. The transmit and return beams are reflected from a motor-driven prism rotating at 300 rpm as depicted in Figure 5-13. Range measurements are taken at 1.5-milliradian intervals and correlated with the azimuth angle using an optical encoder. The detection range for a 3/8-inch cable is greater than 75 feet, while larger targets can be reliably sensed out to 250 feet or more. Detected obstacles are displayed in a format similar to a radar plan-position indicator, and visual and audible warnings are provided in the event the measured range within prespecified warning zones falls below an established threshold. To achieve broader three-dimensional sensor coverage, a concept employing two counter-rotating wedge-prisms is under investigation (SEO, 1991d).

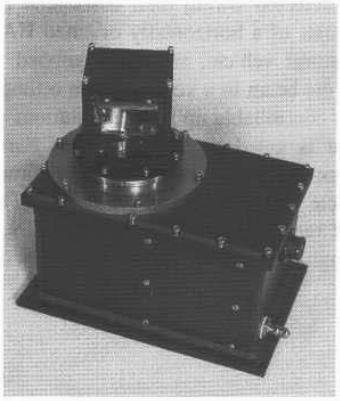

Figure 5-13. Distance measurements are correlated with the azimuth angle of a rotating prism to yield range and bearing information for detected obstacles (courtesy Schwartz Electro-Optics, Inc.).

Table 5-4. Selected specifications for the *Hover Obstacle Avoidance Proximity Sensor System.*

Parameter	Value	Units
Wavelength	904	nanometers
Output energy	50	nanojoules
Pulse width	7	nanoseconds
Minimum range	5	feet
Maximum range	250	feet
Accuracy	±0.5	feet
Scan angle	360	degrees
Scan rate	5	Hz
Samples per scan	2048	
Diameter	7	inches
Length	11.75	inches
Weight (sensor)	< 10	pounds
(display)	< 10	pounds
Power	18 to 36	volts DC
	< 2	amps

SEO *TreeSense*

TreeSense was developed by SEO for automating the selective application of pesticides to orange trees, where the goal was to enable individual spray nozzles only when a tree was detected within their associated field of coverage. The sensing subsystem consists of a horizontally oriented HAAMS unit mounted on the back of an agricultural vehicle, suitably equipped with a rotating mirror arrangement that scans the beam in a vertical plane orthogonal to the direction of travel. The scan rate is controllable up to 40 revolutions per second (35 typical). The ranging subsystem is gated on and off twice during each revolution to illuminate two 90-degree fan-shaped sectors to a maximum range of 25 feet on either side of the vehicle as shown in Figure 5-14. (The existing hardware is theoretically capable of ranging to 100 feet using a PIN photodiode and can be extended further through an upgrade option that incorporates an avalanche photodiode detector.)

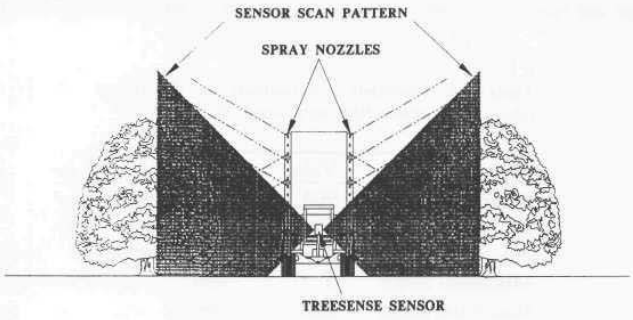

Figure 5-14. The *TreeSense* system illuminates two fan-shaped sectors (±45 degrees with respect to horizontal) on either side of the path to determine the location of trees for precision application of pesticides (courtesy Schwartz Electro-Optics, Inc.).

The *TreeSense* system is hard-wired to a valve manifold to enable/disable a vertical array of nozzles for the spraying of insecticides, but analog as well as digital (RS-232) output can easily be made available for other applications. (A *TreeSense* unit was purchased by Robotic Systems Technology, Inc. for evaluation as a possible collision avoidance sensor on the MDARS Exterior robot.) The system is housed in a rugged fiberglass enclosure (Figure 5-15) with a total weight of only 5 pounds. Power requirements are 12 watts at 12 volts DC.

Table 5-5. Selected specifications for the SEO *TreeSense* system.

Parameter	Value	Units
Maximum range	100	feet
Accuracy	3-4	inches
Wavelength	902	nanometers
Pulse repetition rate	18	KHz
Length	9	inches
Width	9	inches
Height	4.5	inches
Weight	5	pounds
Power	12	volts DC

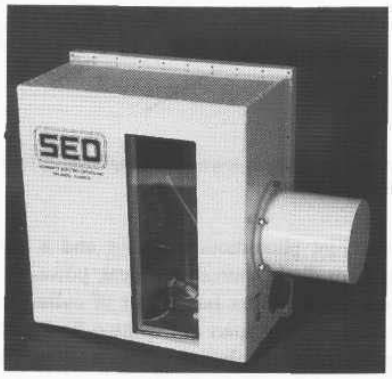

Figure 5-15. The *TreeSense* system is enclosed in a fiberglass housing with two rectangular windows on either side for the left and right fan-shaped beams (courtesy Schwartz Electro-Optics, Inc.).

SEO *AutoSense*

The *AutoSense I* system was developed by SEO under a Department of Transportation Small Business Innovative Research (SBIR) effort as a replacement for buried inductive loops for traffic signal control. (Inductive loops don't always sense motorcyclists and some of the smaller cars with fiberglass or plastic body panels, and replacement or maintenance can be expensive as well as disruptive to traffic flow.) The system is configured to look down at about a 30-degree angle on moving vehicles in a traffic lane as illustrated in Figure 5-16. The

ability to accurately measure vehicle height profiles as well as velocities opens up new possibilities for classifying vehicles as part of the *intelligent vehicle highway systems (IVHS)* concept (Olson, et al., 1994).

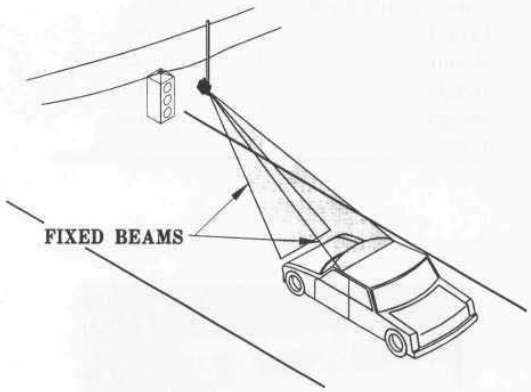

Figure 5-16. Two fan-shaped beams look down on moving vehicles for improved target detection (courtesy Schwartz Electro-Optics, Inc.).

AutoSense I uses a PIN photodiode detector and a pulsed (8 nanosecond) InGaAs near-infrared laser-diode source with peak power of 50 watts. The laser output is directed by a beam splitter into a pair of cylindrical lenses to generate two fan-shaped beams 10 degrees apart in elevation for improved target detection. (The original prototype projected only a single spot of light but ran into problems due to target absorption and specular reflection.) As an added benefit, the use of two separate beams makes it possible to calculate the speed of moving vehicles to an accuracy of 1 mile per hour. In addition, a two-dimensional image (i.e., length and width) is formed of each vehicle as it passes through the sensor's field of view, providing accurate data for numerous vehicle classification applications.

An improved second-generation unit (*AutoSense II*) uses an avalanche photodiode detector instead of the PIN photodiode for greater sensitivity, and a multifaceted rotating mirror with alternating pitches on adjacent facets to create the two beams. Each beam is scanned across the traffic lane 720 times per second, with 15 range measurements made per scan. This azimuthal scanning action allows for generation of a precise three-dimensional profile to better facilitate vehicle classification in automated toll booth applications. An abbreviated system block diagram is depicted in Figure 5-17.

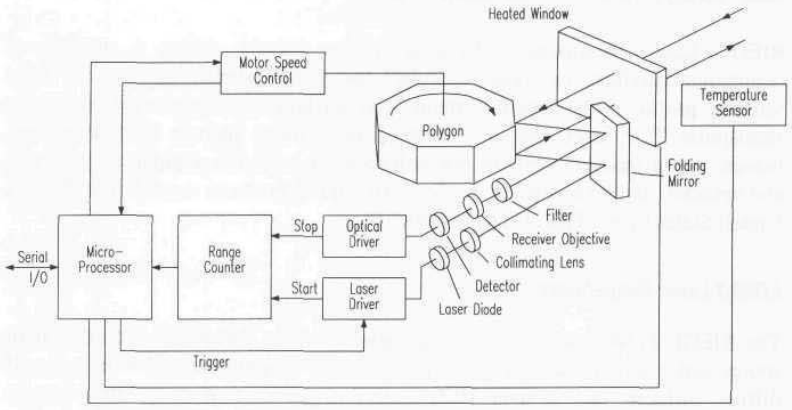

Figure 5-17. Simplified block diagram of the *AutoSense II* time-of-flight 3-D ranging system (courtesy Schwartz Electro-Optics, Inc.).

Intensity information from the reflected signal is used to correct the *time-walk* error in threshold detection resulting from varying target reflectivities, for an improved range accuracy of ±3 inches over a 5- to 30-foot field of regard. The scan resolution is 1 degree, and vehicle velocity can be calculated with an accuracy of 2 mph at speeds up to 60 mph. High-speed RS-232 and RS-422 outputs are provided. A third-generation *AutoSense III* is now under development for an application in Canada that requires three-dimensional vehicle profile generation at speeds up to 100 miles per hour.

Table 5-6. Selected specifications for the SEO *AutoSense II* system.

Parameter	Value	Units
Maximum range	30	feet
Accuracy	±3	inches
Wavelength	904	nanometers
Pulse repetition rate	15	KHz
Scan rate	29.29	rps
Length	9	inches
Width	4.5	inches
Height	9	inches
Weight	5	pounds
Power	12	volts DC
	1	amp

5.2.2 RIEGL Laser Measurement Systems

RIEGL Laser Measurement Systems, Horn, Austria, offers a number of commercial products (i.e., laser binoculars, surveying systems, "speed guns," level sensors, profile measurement systems, and tracking laser scanners) employing short-pulse TOF laser ranging. Typical applications include lidar altimeters, vehicle speed measurement for law enforcement, collision avoidance for cranes and vehicles, and level sensing in silos. All RIEGL products are distributed in the United States by RIEGEL USA, Orlando, FL.

LD90-3 Laser Rangefinder

The RIEGL *LD90-3 series* laser rangefinder employs a near-infrared laser diode source and a photodiode detector to perform TOF ranging out to 500 meters with diffuse surfaces, and to over 1000 meters in the case of cooperative targets. Round-trip propagation time is precisely measured by a quartz-stabilized clock and converted to measured distance by an internal microprocessor using one of two available algorithms. The *clutter suppression* algorithm incorporates a combination of range measurement averaging and noise rejection techniques to filter out backscatter from airborne particulates, and is therefore useful when operating under conditions of poor visibility (Riegel, 1994). The *standard measurement* algorithm, on the other hand, provides rapid range measurements without regard for noise suppression, and can subsequently deliver a higher update rate under more favorable environmental conditions. Worst case range measurement accuracy is ±5 centimeters, with typical values of around ±2 centimeters. The pulsed near-infrared laser is Class-1 eye-safe under all operating conditions.

Figure 5-18. The Class 1 (eye-safe) *LD90-3 series* TOF laser rangefinder is a self-contained unit available in several versions with maximum ranges of 150 to 500 meters under average atmospheric conditions (courtesy RIEGL USA).

A nominal beam divergence of 2 milliradians for the LD90-3100 unit (see Table 5-7 below) produces a 20-centimeter footprint of illumination at 100 meters (Riegl, 1994). The complete system is housed in a small light-weight metal enclosure weighing only 1.5 kilograms and draws 10 watts at 11 to 18 volts DC. The standard output format is serial RS-232 at programmable data rates up to 19.2 kilobits per second, but RS-422 as well as analog options (0 to 10 volts DC and 4 to 20 milliamps current-loop) are available upon request.

Table 5-7. Typical specifications for two popular models of the *LD90-3 series* rangefinders.

Parameter		LD90-3100	LD90-3300	Units
Maximum range	(diffuse)	150	400	meters
	(cooperative)	>1000	>1000	meters
Minimum range		1	3-5	meters
Accuracy	(distance)	±2	±5	centimeters
	(velocity)	±0.3	±0.5	meters/sec
Beam divergence		2	2.8	milliradians
Power		11-18	11-18	volts DC
		10	10	watts
Size		22 x 13 x 7.6	22 x 13 x 7.6	centimeters
Weight		1.5	1.5	kilograms

Scanning Laser Rangefinders

The *LRS90-3 Laser Radar Scanner* is an adaptation of the basic LD90-3 electronics, fiber-optically coupled to a remote *scanner unit* as shown in Figure 5-19. The scanner package contains no internal electronics and is thus very robust under demanding operating conditions typical of industrial or robotic scenarios. The motorized scanning head pans the beam back and forth in the horizontal plane at a 10-Hz rate, resulting in 20 data-gathering sweeps per second. Beam divergence is 5 milliradians, with the option of expanding in the vertical direction if desired up to 2 degrees.

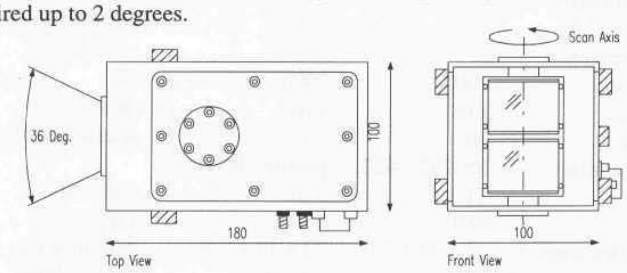

Figure 5-19. The *LRS90-3 Laser Radar Scanner* consists of an *electronics unit* (not shown) connected via a duplex fiber-optic cable to the remote *scanner unit* depicted above (courtesy RIEGL USA).

Figure 5-20 shows a representative plot of actual range data output taken along a curved section of roadway with the scanner fixed in a stationary position.

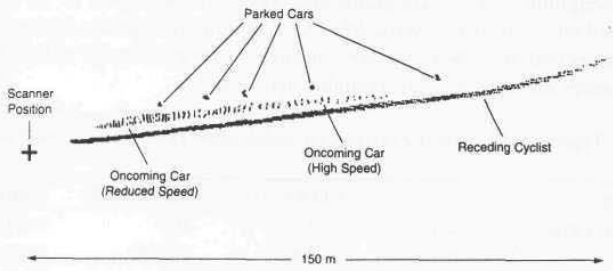

Figure 5-20. Plot of measured range values for a fixed sensor position at X, showing the path of an oncoming vehicle and a receding bicyclist along a curved roadway section (courtesy RIEGL USA).

The *LSS390 Laser Scanning System* is very similar to the *LRS90-3* but scans a more narrow field of view (±10 degrees) with a faster update rate (2000 Hz) and a more tightly focused beam. Range accuracy is typically ±10 centimeters, ±20 centimeters worst case. The *LSS390* unit is available with an RS-422 digital output (19.2 kilobits standard, 150 kilobits optional) or a 20-bit parallel TTL interface. Selected specifications for the *LRS90-3* and *LSS390* scanners are presented in Table 5-8.

Table 5-8. Typical specifications for the *LRS90-3 Laser Radar Scanner* and the *LSS390 Laser Scanner System* (courtesy RIEGL USA).

Parameter	LRS90-3	LSS390	Units
Maximum range	80	60	meters
Minimum range	2	1	meters
Accuracy	±3	±10	centimeters
Beam divergence	5	3.5	milliradians
Sample rate	1000	2000	Hz
Scan range	±18	±10	degrees
Scan rate	10	10	scans/second
Output (digital)	RS-232, -422	parallel, RS-422	
Power	11-15	9-16	volts DC
	880	880	milliamps
Size (electronics)	22 x 13 x 7.6	22 x 13 x 7.6	centimeters
(scanner)	18 x 10 x 10	6 x 9 x 12	centimeters
Weight (electronics)	1.5	1.3	kilograms
(scanner)	1.6	0.9	kilograms

5.2.3 Odetics *Fast Frame Rate 3-D Laser Imaging System*

Odetics, Inc., Anaheim, CA, has designed and partially fabricated a fast-frame-rate, pulsed TOF laser imager for use in high-speed autonomous land vehicle navigation and other machine vision applications. Three-dimensional range images out to 300 feet are captured by a pulsed laser rangefinder capable of acquiring one million range pixels per second. A GaAlAs diode laser produces a peak power output of approximately 50 watts, but the extremely narrow pulse width (12 nanoseconds) permits eye-safe operation within the maximum permissible exposure limits pursuant to the ANSI standard for the safe use of lasers.

A 60-degree azimuth and 30-degree elevation field of view is provided by a high-speed polygonal scanner mechanism as illustrated in the block diagram of Figure 5-21. Line scanning is programmable in elevation for random line access and faster scan functions, with a minimum capability of 12 frames/second of 256 pixels by 128 lines.

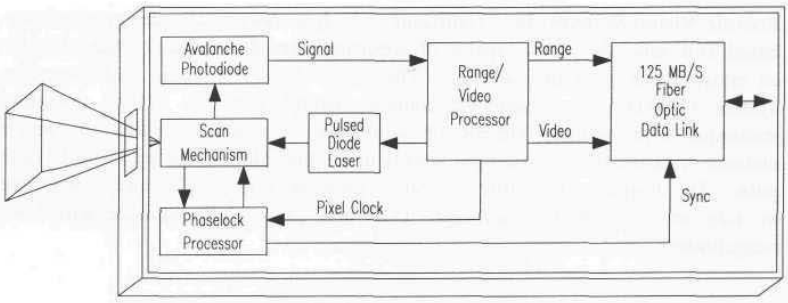

Figure 5-21. The *Fast Frame Rate 3-D Laser Imaging System* provides 3-D range data out to 300 feet for a 256-pixel by 128-line format at a 12-Hz frame rate (courtesy Odetics, Inc.).

Simultaneous range and reflectance images are processed and stored in a *VME Bus* frame buffer for direct pixel access by user image processors. Range data is processed by a pipelined picosecond *emitter coupled logic (ECL)* time interpolator. Range resolution is 0.5 inches (78 picoseconds) with a single-pulse *noise-equivalent range* of less than 1 foot at the *minimum-discernible-signal* range of 306 feet. Multiple-pulse averaging can reduce this noise scatter as required. The self-contained imaging system will be packaged in a compact (less than 1 cubic foot) enclosure suitable for vehicle mounting, with a full-duplex high-speed user interface provided by a 125 megabit/second fiber-optic data link. Selected specifications are listed in Table 5-9.

Note: Odetics also offers a previously developed phase-shift-measurement laser ranging system discussed in the next chapter.

Table 5-9. Selected specifications for the Fast Frame Rate 3-D Laser Imaging System (courtesy Odetics, Inc.).

Parameter	Value	Units
Maximum range	306	feet
Minimum range	2	feet
Range resolution	0.5	inches
Noise equivalent range	<1	foot
Frame rate	12	Hz
Format	256 pixels x 128 lines	
Field of view (azimuth)	60	degrees
(elevation)	30	degrees
Wavelength	820	nanometers
Output power	<50	watts
Pulsewidth	12 (nominal)	nanoseconds

5.2.4 RVSI *Long Optical Ranging and Detection System*

Robotic Vision Systems, Inc., Haupauge, NY, has conceptually designed a laser-based TOF ranging system capable of acquiring three-dimensional image data for an entire scene without scanning. The *Long Optical Ranging and Detection System (LORDS)* is a patented concept incorporating an optical encoding technique with ordinary vidicon or solid-state camera(s), resulting in precise distance measurement to multiple targets in a scene illuminated by a single laser pulse. The design configuration is relatively simple (Figure 5-22) and comparable in size and weight to traditional TOF and phase-shift measurement laser rangefinders.

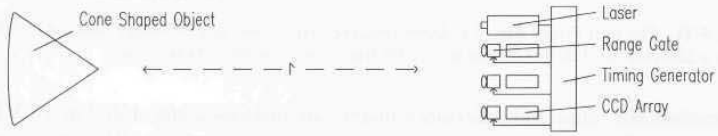

Figure 5-22. Simplified block diagram of a three-camera configuration of the *LORDS* 3-D laser TOF rangefinding system (courtesy Robotic Vision Systems, Inc.).

Major components include a single laser-energy source, one or more imaging cameras, each with an electronically implemented shuttering mechanism, and the associated control and processing electronics. In a typical configuration, the laser will emit a 25-millijoule pulse lasting 1 nanosecond, for an effective transmission of 25 megawatts. The anticipated operational wavelength will lie between 532 and 830 nanometers, due to the ready availability within this range of the required laser source and imaging arrays.

The cameras will be two-dimensional CCD arrays spaced closely together, side by side, with parallel optical axes resulting in nearly identical, multiple views of the illuminated surface. Lenses for these cameras will be of the standard photographic varieties between 12 and 135 millimeters. The shuttering function will be performed by microchannel plate image intensifiers (MCPs), 18 or 25 millimeters in size, which will be gated in a binary encoding sequence, effectively turning the CCDs on and off during the detection phase. Control of the system will be handled by a single-board processor based on the Motorola *MC-68040*.

LORDS obtains three-dimensional image information in real time by employing a novel time-of-flight technique requiring only a single laser pulse to collect all the information for an entire scene. The emitted pulse journeys a finite distance over time; hence, light traveling for 2 milliseconds will illuminate a scene a greater distance away than light traveling only 1 millisecond.

The entire sensing range is divided into discrete distance increments, each representing a distinct range plane. This is accomplished by simultaneously gating the MCPs of the observation cameras according to their own unique on-off encoding pattern over the duration of the detection phase. This binary gating alternately blocks and passes any returning reflection of the laser emission off objects within the field-of-view. When the gating cycles of each camera are aligned and compared, there exists a uniquely coded correspondence which can be used to calculate the range to any pixel in the scene.

For instance, in a system configured with only one camera, the gating MCP would be cycled on for half the detection duration, then off the remainder of the time. Figure 5-23 shows that any object detected by this camera must be positioned within the first half of the sensor's overall range (half the distance the laser light could travel in the allotted detection time). However, significant distance ambiguity exists because the exact time of reflected-energy detection could have occurred at any point within this relatively long interval.

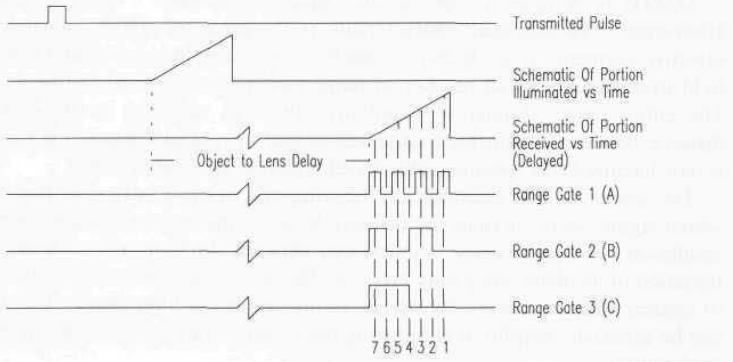

Figure 5-23. *Range ambiguity is reduced by increasing the number of binary range gates* (courtesy Robotic Vision Systems, Inc.).

This ambiguity can be reduced by a factor of two through the use of a second camera with its associated gating cycled at twice the rate of the first. This scheme would create two complete *on-off* sequences, one taking place while the first camera is on and the other while the first camera is off. Simple binary logic can be used to combine the camera outputs and further resolve the range (Figure 5-24). If the first camera did not detect an object but the second did, then by examining the instance when the first camera is off and the second is on, the range to the object can be associated with a relatively specific time frame. Incorporating a third camera at again twice the gating frequency (i.e., two cycles for every one of camera 2, and four cycles for every one of camera 1) provides even more resolution. For each additional CCD array incorporated into the system, the number of distance divisions is effectively doubled.

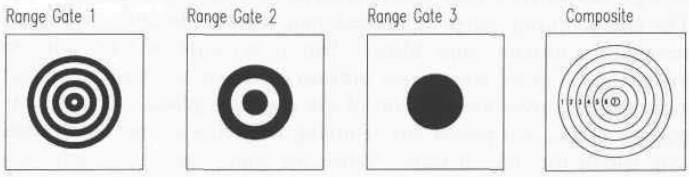

Figure 5-24. Binary coded images from range gates 1-3 are combined to generate the composite range map on the far right (courtesy Robotic Vision Systems, Inc.).

Alternatively, the same encoding effect can be achieved using a single camera when little or no relative motion exists between the sensor and the target area. In this scenario, the laser is pulsed multiple times, and the gating frequency for the single camera is sequentially changed at each new transmission. This creates the same detection intervals as before but with an increase in the time required for data acquisition.

LORDS is designed to operate over distances between 1 meter and several kilometers. An important characteristic is the projected ability to range over selective segments of an observed scene to improve resolution, in that the depth of field over which a given number of range increments is spread can be variable. The entire range of interest is initially observed, resulting in the maximum distance between increments (coarse resolution). An object detected at this stage is thus localized to a specific, abbreviated region of the total distance.

The sensor is then electronically reconfigured to cycle only over this region, which significantly shortens the distance between increments, thereby increasing resolution. A known delay is introduced between the time of transmission and initiation of the detection/gating process. The laser light thus travels to the region of interest without concern for objects positioned in the foreground. This feature can be especially helpful in eliminating backscatter from fog or smoke in outdoor applications.

5.3 References

Arkin, R.C., "Motor-Schema-Based Mobile Robot Navigation," *International Journal of Robotics Research*, Vol. 8., No. 4, pp. 92-112, August, 1989.

Biber, C., Ellin, S., Shenk, E., "The Polaroid Ultrasonic Ranging System," Audio Engineering Society, 67th Convention, New York, NY, October-November, 1980.

Borenstein, J., Koren, Y., "Real-Time Obstacle Avoidance for Fast Mobile Robots in Cluttered Environments," IEEE International Conference on Robotics and Automation, Vol. CH2876-1, Cincinnati, OH, pp. 572-577, May, 1990.

Cybermotion, "Ultrasonic Collision Avoidance System," Cybermotion Product Literature, Salem, VA, 1991.

Depkovich, T., W. Wolfe, "Definition of Requirements and Components for a Robotic Locating System," Final Report MCR-83-669, Martin Marietta Denver Aerospace, Denver, CO, February, 1984.

Everett, H.R., "A Microprocessor Controlled Autonomous Sentry Robot," Masters Thesis, Naval Postgraduate School, Monterey, CA, October, 1982.

Everett, H.R., "A Multi-Element Ultrasonic Ranging Array," *Robotics Age*, pp. 13-20, July, 1985.

Figueroa, J.F., Lamancusa, J.S., "A Method for Accurate Detection of Time of Arrival: Analysis and Design of an Ultrasonic Ranging System," Journal of the Acoustical Society of America, Vol. 91, No. 1, pp. 486-494, January, 1992.

Frederiksen, T.M., Howard, W.M., "A Single-Chip Monolithic Sonar System," *IEEE Journal of Solid State Circuits*, Vol. SC-9, No. 6, December, 1974.

Gustavson, R.L., Davis, T.E., "Diode-Laser Radar for Low-Cost Weapon Guidance," SPIE Vol. 1633, Laser Radar VII, Los Angeles, CA, pp. 21-32, January, 1992.

Hammond, W., "Smart Collision Avoidance Sonar Surpasses Conventional Systems," *Industrial Vehicle Technology '93: Annual Review of Industrial Vehicle Design and Engineering*, UK and International Press, pp. 64-66, 1993.

Hammond, W., "Vehicular Use of Ultrasonic Systems," Technical Report, Cybermotion, Inc., Salem, VA, May, 1994.

Kim, E.J., "Design of a Phased Sonar Array for a Mobile Robot," Bachelor's Thesis, MIT, Cambridge, MA, May, 1986.

Koenigsburg, W.D., "Noncontact Distance Sensor Technology," GTE Laboratories, Inc., 40 Sylvan Rd., Waltham, MA, pp. 519-531, March, 1982.

Lang, S., Korba, L., Wong, A., "Characterizing and Modeling a Sonar Ring," SPIE Mobile Robots IV, Philadelphia, PA, pp. 291-304, 1989.

Langer, D., Thorpe, C., "Sonar Based Outdoor Vehicle Navigation and Collision Avoidance," International Conference on Intelligent Robots and Systems, IROS '92, Raleigh, NC, July , 1992.